Automatic detection of rock glaciers from very-high resolution satellite imagery using convolutional neural networks and object-based image analysis

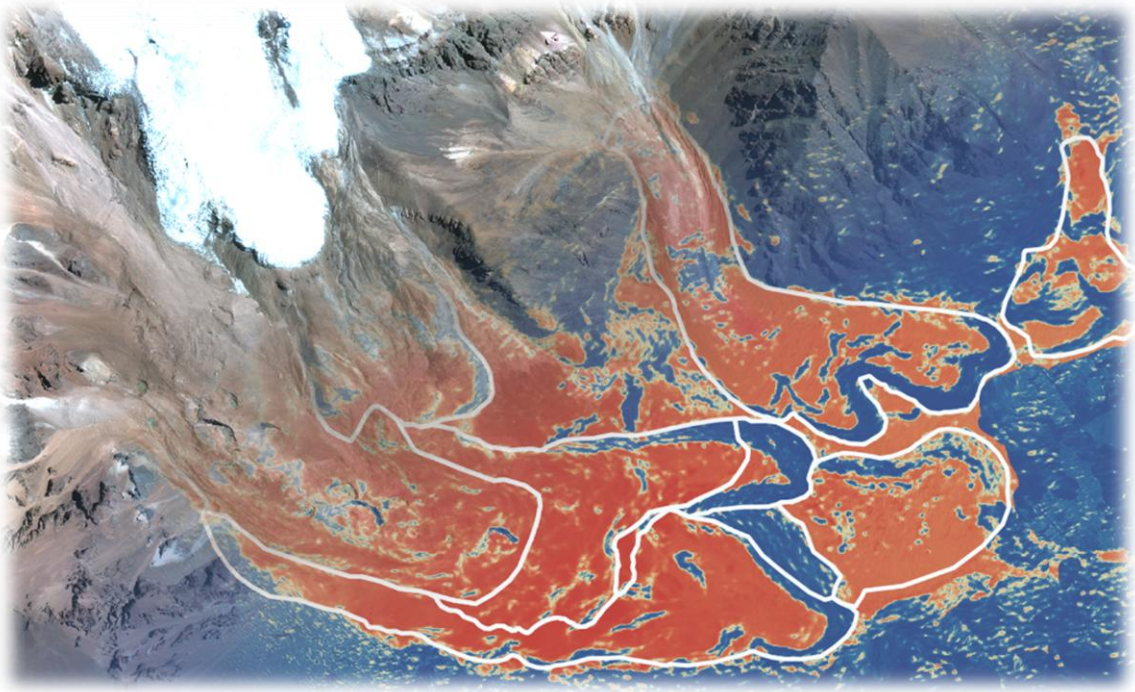

Master's thesis in Physical Geography

Mark Aguera

Department of Geography

University of Bergen

2021

Table of contents

Abstract

A visible expression of permafrost, rock glaciers are lobate-shaped landforms with a mixture of rock, sediment and ice. Due to their ice-content and high resistivity to global warming, they can act as important freshwater providers to local regions. In many world regions, suchas the Semi-Arid Andes, rock glaciers likely play a crucial role in water supplement of the streamflow during dry periods. Nevertheless, these landforms have received significantly less attention from the scientific community than clean-ice or debris-covered glaciers. Because of their spectral similarity of the surrounding bedrock, rock glaciers are extremely difficult to detect automatically and most inventories are still created by manual delineation. However, this method is extremely time-consuming and subjective as it is made by a human user. Based on previous research on automatic rock glacier mapping, this thesis is presenting a new method which uses very-high resolution remote sensing data, convolutional neural networks (CNN) and object-based image analysis (OBIA) to automatically detect and map rock glaciers. CNNs are artificial neural networks which form a sub-field of deep-learning and are based on the automatic identification of reoccurring texture and patterns on images, the same way as the human brain functions. OBIA is an established image analysis method that can be used to refine results produced by a CNN. This combined method was applied on two catchments in the semiarid Andes of Chile: the La Laguna and the Estero Derecho. In order to detect more numerous yet smaller landforms, very-high resolution Pleiades (0.5 m) and SPOT 7 (1.5 m) satellite imagery was used. Two CNN models of three convolutional and two max-pooling layers were built, trained and tested using a manually corrected reference inventory for the La Laguna catchment covered by high-resolution Pleiades imagery. *CNN_noCurv* used spectral bands, elevation and slope information while in the case of *CNN_wCurv*, planform and profile curvature layers were added to the input as well. The results of the heatmap produced were then cleaned and refined by using OBIA. The methods were then tested on the Estero Derecho catchment to investigate how feasible it is to transfer the method on another study area and data from a different sensor.

Both models produced good results on the Pleiades imagery but *CNN_wCurv* was found to be the better one with a mean total accuracy of 94.58% and producer and user accuracies ranging between 63.6 and 80.8%. However, when transferred to SPOT 7 imagery *CNN_wCurv* failed to detect the majority of landforms resulting in a large overestimation. On the other hand, *CNN_noCurv* had an accuracy of 73.15%. It was therefore found that both models are transferable and curvature layers can improve the classification on Pleiades imagery but are

ineffective on the lower resolution SPOT data. In addition to transferability, the new methods produced higher total and producer accuracies than previous attempts for automatic classification. Moreover, new landforms that were not included in the manual reference inventory have been discovered which indicates that the technique is able to outclass manual delineation as well. Given the challenges of rock glacier mapping, the method produced promising results and proved that CNN in combination with OBIA can be an effective tool in automatic landform classification. It was also found that other characteristics such as surface velocity, terrain roughness and mean slope likely plays an important role in detectability and transferability and more research is therefore needed to further improve the technique. This thesis demonstrates that CNN and OBIA can be used for efficient creation of rock glacier inventories.

Acknowledgements

I would like to thank my supervisor, Dr. Benjamin Aubrey Robson from the Department of Earth Sciences at the University of Bergen. Without his suggestions and help the completion of this thesis would not have been possible. I also wish to express my gratitude to the European Space Agency and Airbus Defence and Space, who provided the high-resolution satellite tri-stereos for this study. Last but not least, I would like to pay regards to Dr. Shelley MacDonell from CEAZA who was kind enough to send the manually corrected rock glacier inventories for reference.

Table of figures

List of abbreviations

°C	Degrees centigrade
µm/mm/cm/m/km	Micrometre/Millimetre/Centimetre/Metre/Kilometre
a^{-1}	Per year
Airbus DS	Airbus Defence and Space
AL	Active layer
AOI	Area Of Interest
ATCOR	Atmospheric and Topographic Correction
CEAZA	Centro de Estudios Avanzados en Zonas Áridas (Centre of Advanced Studies in Arid Zones)
CNN	Convolutional Neural Network
DEM	Digital Elevation Model
DGA	Dirección General de Aguas (National Water Directorate)
DInSAR	Differential Interferometric Synthetic Aperture Radar
DL	Deep Learning
ELA	Equilibrium line altitude
ENSO	El Niño – Southern Oscillation
ESA	European Space Agency
EO	Earth Observation
GCP	Ground Control Point
GDAL	Geospatial Data Abstraction Library
GEOBIA	Geographic Object-based Analysis
GIS	Geographic Information System
GPS	Global Positioning System
GPR	Ground Penetrating Radar
Gt	Gigatons
InSAR	Interferometric Synthetic Aperture Radar

Landsat MSS	Landsat Multispectral Scanner
Landsat TM	Landsat Thematic Mapper
$L\ s^{-1}$	Litres per second
MAAT	Mean annual air temperature
m.a.s.l	Metres above Sea Level
ML	Machine Learning
MSS	Multiscale Segmentation
MNDWI	Modified Normalised Difference Water Index
m.w.e.	Meter water equivalent
NDSI	Normalized Difference Snow Index
NDVI	Normalized Difference Vegetation Index
NDWI	Normalized Difference Water Index
NIR	Near-Infrared
OLR	One Level Representation
OBIA	Object Based Image Analysis
PBIA	Pixel Based Image Analysis
RPC	Rational Polynomial Coefficient
SAR	Synthetic Aperture Radar
SAVI	Soil Adjusted Vegetation Index
SLASP	Slope and Aspect
SPOT	System Pour l'Observation de la Terre (System for Earth Observation)
SRTM	Shuttle Radar Topography Mission
SVM	Support vector machine
TP	Tie point
TRI	Terrain Ruggedness Index
VRM	Vector Ruggedness Measure
WVEQ	Water Volume Equivalent

1. Introduction

This chapter will give an overview on the background of the research project. It shall explain the definition of rock glacier and why monitoring their changes caused by climate change in is crucial. An introduction of the methods used in this thesis will also be introduced.

1.1. Role of mountainous areas in a changing climate

Mountainous regions cover approximately 25% of continental surfaces and host about 26% of world's population. These regions have very complex geographical characteristics such as rapid and systematic climatic changes (precipitation, temperature) over very short distances, enhanced direct runoff and erosion or environmental factors such as different soil types (Beniston, 2003). Because of the rapid changes of elevations in relatively short distances, mountain areas are unique regions extremely sensitive to the effects of climate change.

Global changes in climate may increasingly threaten, or at least alter the capacity of mountain ecosystems to provide goods and services for both highland and lowland populations. In most mountainous regions, a warmer climate will lead to a reduction in the mass of glaciers, as well as snow-pack and permafrost. In the Alps for example, empirical and energy-balance models indicate that 30 – 50% of the existing mountain glacier mass could disappear by 2100 if global warming scenarios in the range of 2 – 4 °C indeed occur (Haeberli and Beniston, 1998). With an upward shift of 200 – 300 m in the equilibrium line altitude (ELA, which represents the level below which ablation rates exceed accumulation), the reduction in ice thickness of temperate glaciers could reach 1 – 2 m per year. As a result, many glaciers in the temperate mountain regions of the world would lose most of their mass within decades. As of 2020, the global annual mass change was -9.82 meter water equivalent (m.w.e.) while the total mass change since 1970 was at -248,37 m.w.e. according to the World Glacier Monitoring Service (2021). Changes in the climate regimes may have far-reaching consequences for freshwater supply in agriculture, tourism and hydro-power. These shifts would affect not only mountain populations, but also those living downstream of the mountains and who depend on mountain-fed water resources (Beniston, 1999). Mountains are the source areas of 50% of the world's rivers and 40% of the global population lives in the watersheds of rivers originating in the planet's different mountain ranges that provide freshwater supply (Beniston, 2003). Having a very long north – south extend, the Andes in South America is usually divided into tropical (north of ~20°S), dry (~20° – 35°S) and wet

(south of ~35°S) zones. In the tropical Andes, the monthly maximum contribution of glacial meltwater during a normal year is 61% in La Paz, Bolivia and 67% in Huaraz, Peru (Buytaert et al., 2016). Having less rainfall and more numerous cryospheric landforms, melt water is more significant in the Dry Andes as it makes up a greater proportion of streamflow. In the central part of the range, the glacier contribution to the streamflow can reach 67% in many basins (Peña and Nazarala, 1987). The awareness about the global importance of mountain areas has increased in the last decades. Along with this, the need for a better understanding of the functioning of mountain ecosystems and of the global change impacts on these ecosystems has been grown (Hofer, 2005).

1.2. The semiarid Andes

This project would focus on a region of the Central Andes (ca. 20° – 50° S) in Chile where a significant part of the country's population live and where water resources are vulnerable not only to climate change but also the expansion of mining and agriculture (Janke et al., 2017). The Sub-tropical Andes are characterised by a very dry climate because of their position on the eastern flank of the Pacific anticyclone (Clapperton, 1993) and the cold Humboldt current (Fiebig-Wittmaack et al., 2012). In the region, interannual climate variability is influenced by both the El Niño – Southern Oscillation (ENSO) and moisture levels in the extratropical lowlands east of the Andes (Placzek et al., 2009). The annual precipitation is less than 1000 mm falling mostly during the austral high summer (December – January). South from the latitude 30°S, winter (May – August) has a more significant amount of precipitation, coming with the northerly penetration of cyclonic depressions from the southwest and southeast (Clapperton, 1993). At high altitudes (~4000 m a.s.l.), precipitation ranges from ~200 mm at the northern edge to 700-800 mm a^{-1} at the southern end of the semiarid Andes (Schaffer et al., 2019). The arid and semiarid environments are often uniquely sensitive to climate change (Placzek et al., 2009). In these regions of Chile, the cryosphere is a major concern for local population, due to the impact of water resources (Rabatel et al., 2010). These zones of limited water resources correspond to areas with the highest population density (including the capital, Santiago de Chile), significant agricultural development and extensive mining activity. Water supply for these sectors is largely reliant on melt from seasonal snow and ice bodies from the Andean Cordillera (Favier et al., 2009, Azócar and Brenning, 2010a, Schaffer et al., 2019). For example, the glacier contribution to streamflow has been estimated at ~50% in the Juncal River Basin (Rodriguez et al., 2016), ~42 and ~67% for the Yeso River Basin (Ayala et al.,

2016) and 2 – 23% for the Huasco Basin (Gascoin et al., 2011). Due to the changing climate, a fall of precipitation and desertification can be observed. Therefore, a plan to develop an advanced water management policy has been recommended by the Chilean National Water Directorate (DGA) to adapt to a warming climate and to enforce the conservation of water sources. For this, an extensive study and observation of the hydrological system of every potential freshwater source is needed (Schaffer et al., 2019).

1.3. Rock glaciers and their importance

Rock glaciers are tongue-like masses of large, angular blocks, finer debris and ice (Allaby, 2013). They are a mixture of rock, sediment and ice and visible manifestations of cumulative deformation of ice-rich creeping mountain permafrost (Schaffer et al., 2019). Most rock glaciers are less sensitive to climate change than glaciers due their high concentration of rocks and debris in their bodies which provide protection (Janke et al., 2017) and can contain a significant amount of ice. The high ice-content can lead to deformation and a creeping motion of the rock glacier body. By the degree of this activity of movement, rock glaciers can be active or inactive. Inactive rock glaciers can be subdivided into the groups intact (inactive, but still containing ice) or relict (all the ice have melted) rock glaciers (Kääb, 2013). Based on their origin, Schaffer et al. (2019) distinguishes three classes of rock glaciers based on their origins: glaciogenic rock glaciers are formed from debris-covered glaciers, cryogenic rock glaciers are formed from the geological processes associated with permafrost and polygenic rock glaciers have a combined glaciogenic and cryogenic origin. Apart from these, several other definitions and classifications exist, since the origins of rock glaciers has been a subject of scientific debates (See Chapter 4). Compared to glaciers, the distribution and hydrological significance of rock glaciers have received little attention (Jones et al., 2018a), despite their significant role as water stores.

Because of the dry climate, the semiarid Andes contain only a small number of glaciers but a larger number of rock glaciers. It is in fact thought that rock glaciers contain the most significant store of fresh water in the semiarid Andes, because they are the predominant cryospheric landform (Azócar and Brenning, 2010b, Schaffer et al., 2019). In the case of some catchments, the rock glacier contribution to streamflow is estimated at 13 – 30% (Schaffer et al., 2019, Robson et al., 2020). This makes rock glaciers extremely important factors in the freshwater supply of the 900 000 habitants of the Elqui catchment and local industries which can affect many more people in the country. Thus, rock glaciers need to be

preserved and constantly monitored for a successful water resource management. For this reason, it is crucial to create and maintain up-to-date and accurate large-scale rock glacier inventories.

1.4. Remote Sensing for rock glaciers detection

The field measurements of mountainous regions can be extremely costly and logistically complicated. By using remote sensing (RS) data (with the inclusion of GIS technologies), it is possible to investigate glacial and periglacial areas that can be too time-consuming, dangerous or expensive to approach on field. Remote sensing is defined as the acquisition and measurement of information about certain properties of phenomena, objects or materials by a recording device not in physical contact with the features under surveillance (Khorram et al., 2012). It is an effective tool for rock glacier monitoring since it provides large coverage and repetitive acquisition (Khorram et al., 2012). Before the spread of satellite remote sensing, rock glaciers were studied with paper maps or aerial photos. For example, White (1979) mapped more than 600 rock glaciers of the San Juan Mountains, Colorado by using air photos and topographic maps. Although aerial photos have very-high resolution and allow high-precision photogrammtery, they have weaknesses as well. Early photographs were available only in black-and-white which limited their capabilities. Furthermore, aerial surveys are usually performed at irregular intervals with often incomplete spatial coverage. Aerial photography is still frequently used for rock glacier monitoring (Kaufmann, 2012), yet, the uptake of earth observation (EO) satellites in the latter half of the 20th century opened new horizons in the field of RS. EO satellites orbiting around the planet provide global coverage on a more systematic basis (Khorram et al., 2012) . Today, a wide range of remote sensing data is freely available. Satellite imagery can be downloaded from both national and international databases for image processing or spatial analyses. Satellite and aerial images are also available on web-map softwares such as Google Earth which provides easy access to processed and corrected imagery. Commercial satellites can provide very-high resolution imagery although these products can be costly.

1.5. Rock glacier delineation

Being near-identical to the surrounding paraglacial terrain, rock glaciers are more difficult to detect than clean ice or debris-covered glaciers. Early rock glacier inventories were created by

manual delineation of landforms on aerial photography (Wahrhaftig and Cox, 1959, Outcalt and Benedict, 1965, White, 1979). The method is still the most popular way for rock glacier inventory creation. It is usually performed on high-resolution aerial or satellite imagery using a GIS or other vector based-graphics tools (Jones et al., 2018c, Rangecroft et al., 2014, Pandey, 2019, Schmid et al., 2015). Manual methods are however time consuming and dependent on the consistency or local knowledge of the interpreter (Gjermundsen et al., 2011). Some attempts for the use of machine-learning have been made (Janke, 2001, Brenning, 2009, Brenning et al., 2012) using surface textures or morphological characteristics, although these methods have only been applied on small areas with a relatively small number of rock glaciers (Robson et al., 2020).

1.6. Methods used for this investigation

Deep learning (DL) is a class of machine-learning algorithms, that has recently become a hot topic as a new powerful method for image recognition and classification (Liangpei et al., 2016). These algorithms attempt to interpret imagery in the same way as a human operator would, relying not only on pixel values but reoccurring patterns and textures (Timilsina et al., 2019, Robson et al., 2020). Convolutional neural networks (CNN) are a group of DL models that are broadly used in the scientific community (Timilsina et al., 2019). CNNs are inspired by the brain's neural networks and have made important breakthroughs in image recognition (Zhang et al., 2019). They are a variant of multilayer neural networks, where images are handled as multidimensional inputs which are given and transformed over a series of hidden layers to reach the output (Sharma et al., 2017). CNNs rely on large sample datasets to train the algorithm to recognise recurring patterns within the datas and are typically utilised in applications where spectral characteristics are not sufficient (Robson et al., 2020). These algorithms have seen a massive rise of popularity, although, being a relatively young topic, many questions are still unanswered and further research and developments are needed to provide more effective and trustworthy methods. The CNNs that are used in classification of remote sensing data produce a heatmap with probability values for each pixel belonging to a class.

Object-based image analysis (OBIA) is an image analysis method that creates more or less homogenous objects through image segmentation as the basis of classification which allows the use of contextual, hierarchical and spatial characteristics of image objects (Robson et al., 2015, Rastner et al., 2014, Robson et al., 2020). OBIA has been successfully used in many

research projects to detect clean ice and debris-covered glaciers (Robson et al., 2015, Rastner et al., 2014, Kraaijenbrink et al., 2016, McNabb et al., 2016, Robson, 2016). The objective of this thesis is to develop a technique in order to automatically detect rock glaciers on different areas of the semiarid Andes, using high-resolution optical satellite imagery with the combination of CNN and OBIA. The method has been applied by Robson et al. (2020) who found that OBIA can be used to refine, reshape or correct results created by a CNN and to create meaningful polygons as rock glacier outlines out of a heatmap raster. The two methods together formed an effective way to automatically identify rock glaciers with promising results. This thesis investigates further possibilities by using higher resolution satellite imagery to identify smaller yet more numerous landforms.

2. Study Area

The study area is located in semiarid Andes of Chile – approximately between the latitudes 30°S and 30.5°S – around 120 km east to La Serena, near the Argentine border (Figure 1). Two different catchments were chosen for this study: The La Laguna (also known as Tapado) catchment and the Estero Derecho catchment. Both of them include a large number of rock glaciers and have been in focus of previous research.

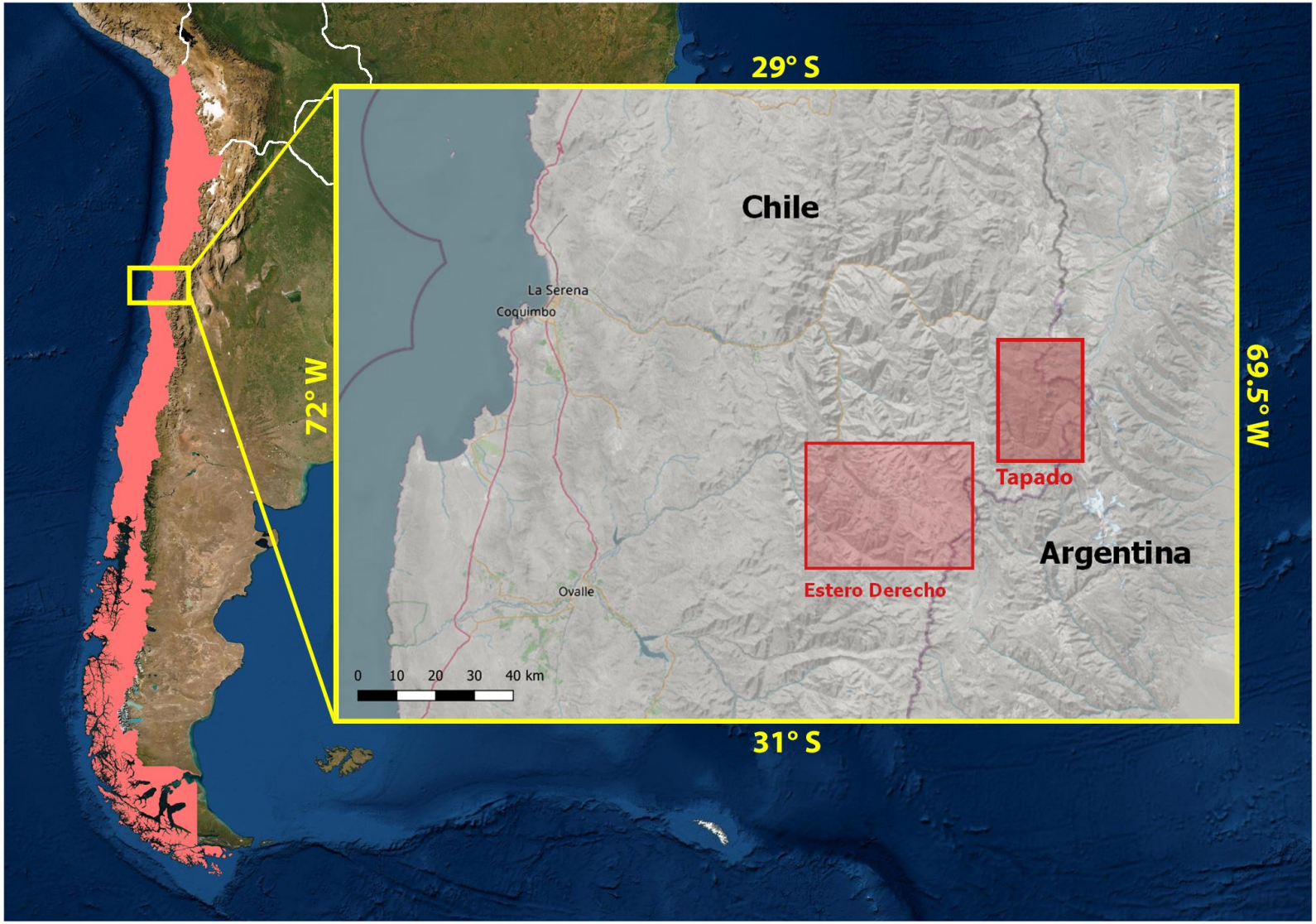

Figure 1: Location of the two study areas in the Chilean Andes.

2.1. Primary Study Zone

The primary study area is the La Laguna catchment, where the Tapado glacier and the glacial foreland (debris-covered glaciers, rock glaciers and moraines) form together the Tapado glacial complex (Figure 3). The region has a semiarid and cold climate. At the elevation of ~3000 m a.s.l., it has a mean precipitation of 167 mm per year measured between 1970 and 2009 and a mean annual air temperature (MAAT) of 8 °C recorded between 1974 and 2011. The MAAT has been reported to be rising by 0.17 °C per decade between 1974 and 2011 (Monnier et al., 2014a, Robson et al., 2020).

The Tapado glacier (located at 30.1°S, 69.9°W, 4500 – 5535 m a.s.l.) flowing on the side of the mountain *Cerro Tapado* is one of the few glaciers in the region (Sinclair and MacDonell, 2016). The mountain is mainly made of dacitic and rhyolitic materials from upper Paleozoic–Lower Trias (so-called *Pastos Blancos* Formation) and upper Oligocene–Lower Miocene (so-called *Doña Ana* Formation) periods (Monnier et al., 2014b). The area also consists of debris-covered glacier sections as well as 105 rock glaciers according to the DGA inventory. Some of the significant rock glaciers are the *Tapado Rock Glacier*, the *Las Tolas* (Figure 2), the *Empalme* and the *Llano de las Liebres* (Schaffer et al., 2019). Due to its complexity, these landform assemblages are hard to identify from surface observation (Monnier et al., 2014a). The area has been in the focus of research with particular emphasis on the hydrological functioning of the landforms within the catchment. When it comes to ice content of rock glaciers in the semiarid Andes, the values of 50% (Brenning, 2005, Azócar and Brenning, 2010b) and 60% (Schrott, 1996) have been assumed. Indirect geophysical measurements at two specific rock glaciers have been done: Monnier and Kinnard (2015) estimates an average ice content of 66% for the rock glacier *Llano de las Liebres* and Milana and Güel (2008) approximated an average ice content of 33.5% in another rock glacier adjacent to the *Cerro Tapado* (Milana and Güell, 2008, Schaffer et al., 2019).

It is assumed that the Tapado catchment actively supplies water to the lower semiarid areas of the Elqui river basin by contributing between 4 and 13% of the annual streamflow (Pourrier et al., 2014, Robson et al., 2020). By using a combination of the minimal glacier discharge data available and published discharge values measured at rock glaciers outside of the semiarid Andes, Schaffer et al. (2019) estimated the rock glacier contribution to the streamflow. They found that rock glaciers likely contributed 140, 300 and 930 L s^{-1} for a minimum, likely

maximum and extreme maximum scenario respectively, which indicates 9 – 20 % of the streamflow (Schaffer et al., 2019).

Figure 2: The Las Tolas rock glacier (Photograph: Benjamin Aubrey Robson).

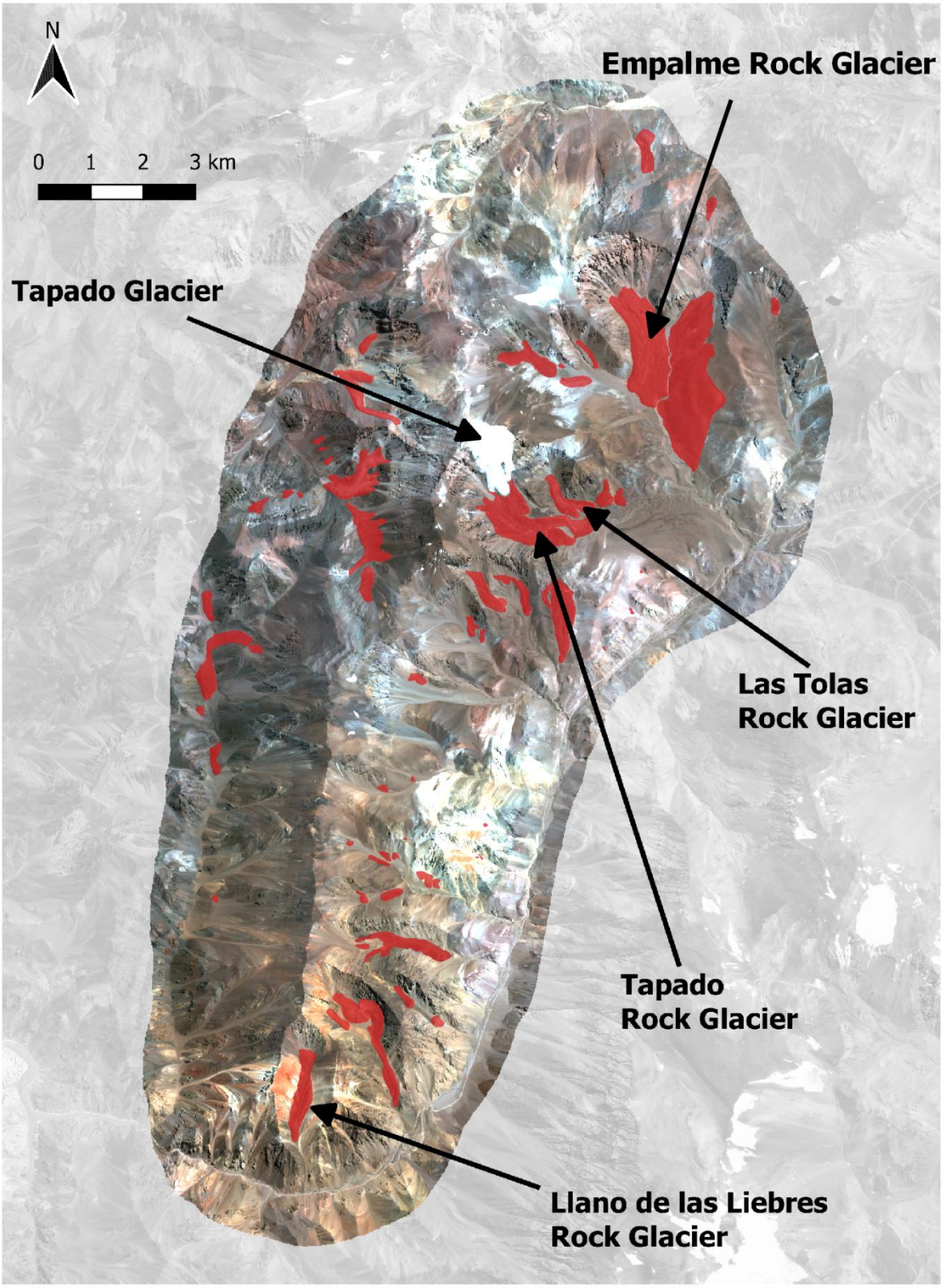

Figure 3: The La Laguna catchment with rock glaciers shown in red. Background image is an orthorectified Pleiades mosaic (highlighted) from 2020 combined with ESRI satellite map.

2.2. Secondary Study Zone

The secondary study area is located at the headwaters of the Elqui River in the Coquimbo Region within a reserve called Estero Derecho (Figure 4), where precipitation is increasing with the elevation reaching ~ 160 mm a^{-1} at 2900 m a.s.l in the Estero Derecho valley (de Pasquale et al., 2020). The specific study zone is a ~697 km^2 area within the Estero Derecho reserve at an average altitude of ~4000 m a.s.l. south west from the La Laguna catchment. The area does not contain glaciers, only a large number of rock glaciers. The most prominent ones are locally known as the *El Jote*, which is a inactive rock glacier and the *El Ternero* which is an active rock glacier, the largest one within Estero Derecho (de Pasquale et al., 2020). The only in-situ measurement in Estero Derecho was carried out on these two glaciers: de Pasquale et al. (2020) presented results of electrical resistivity and refraction seismic tomography profiles and proposed a diagnostic model representation for the differentiation between active and inactive rock glaciers. A map of the secondary study zone is shown in Figure 3.

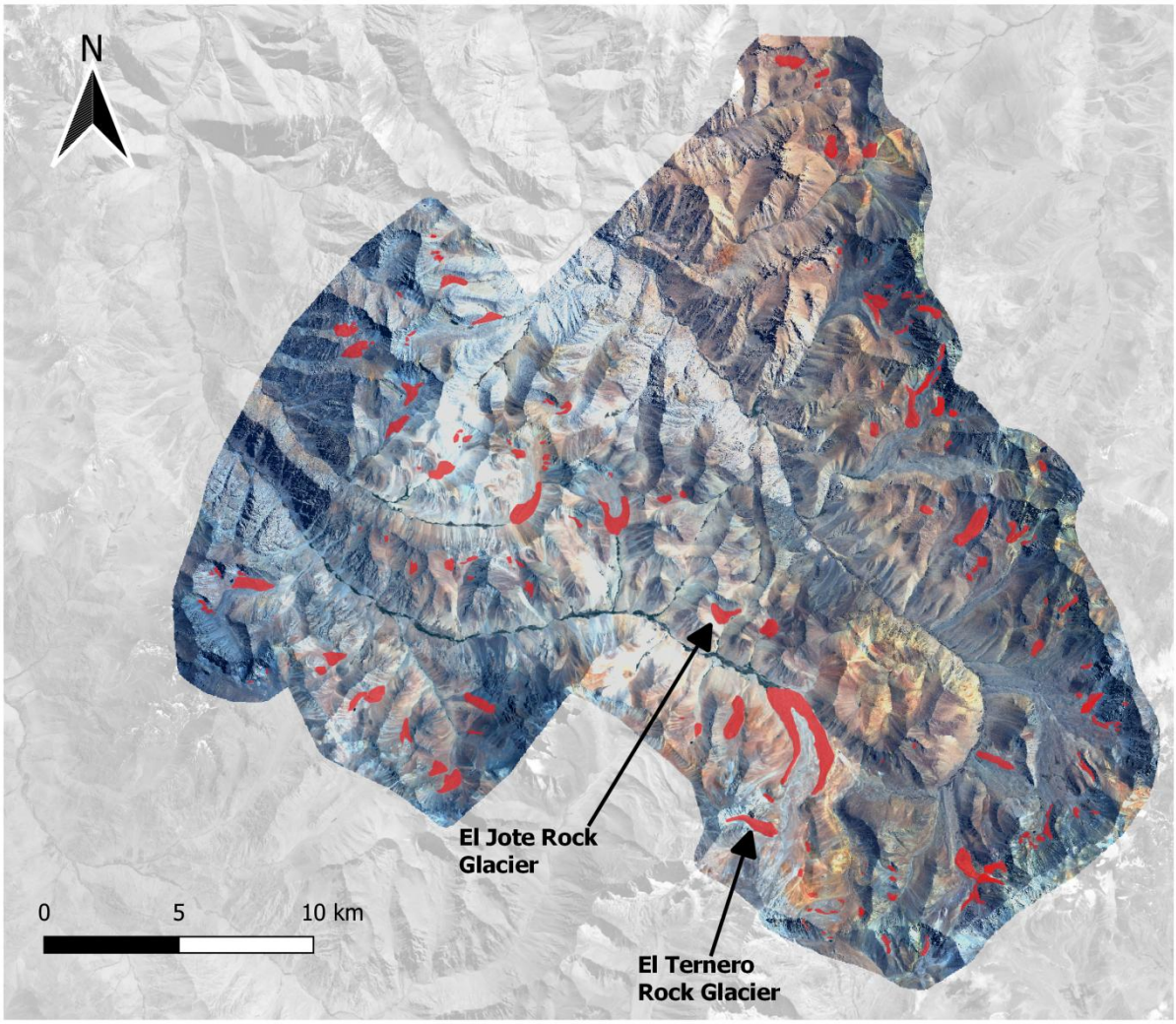

Figure 4: The Estero Derecho catchment with rock glaciers shown in red. Background image is an orthorectified Pleiades and SPOT mosaic (highlighted) and from 2020 combined with ESRI satellite map.

3. Objectives

The thesis will focus on two different study areas located in the semiarid Andes in Chile and investigate the possibilities of using remote sensing and machine learning to map the glacial and periglacial landforms. The investigation is focusing on the following main and sub-research questions:

What machine learning/deep learning methods and parameters provide the best results for landform detection in the primary study area?

a. **How transferable the newly developed method is to another periglacial catchment?**
b. **How well the newly developed method works with data from a different sensor?**

4. Background

This chapter discusses the theoretical background of the thesis starting with a detailed description of rock glaciers followed by optical satellite remote sensing and rock glacier mapping methods with reviews of relevant, published papers about previous research.

4.1. Rock glaciers

Besides the one used in the *Introduction* chapter, several other rock glacier definitions exist due to the disagreement on the content of the term (Berthling, 2011). Rangecroft et al. (2015) define them as glacier-shaped cryospheric landforms, a mixture of angular rock debris with a core of ice or ice-cemented fine class, usually with a distinct ridge and furrow surface pattern. Jones et al. (2018) describe rock glaciers as cryoshperic landforms that are formed by gravity-driven creep of accumulations of rock debris supersaturated within ice while others like Barsch (1996), Haeberli et al. (2006) or Robson et al. (2020) define them as landforms of unconsolidated, ice-rich material that are visible manifestations of permafrost. Formerly, rock glaciers were often thought to be a form of debris-covered glaciers. Since then, a number of fundamental differences have been established (Kääb, 2013). While debris-covered glaciers are composed almost exclusively of snow and ice (Schaffer et al., 2019) with a thin and discontinuous debris cover (Monnier and Kinnard, 2017), rock glaciers form rather a mix of debris with a core of ice (Rangecroft et al., 2015) with a several-metre-thick ice-free debris layer that thaws every summer (Monnier and Kinnard, 2017). Rock glaciers occur in most cold mountains on Earth. These include the Andes, the Rocky Mountains, the European Alps, the Pyrenees, the Caucasus region, the Central Asian mountain ranges, the Siberian mountain ranges, the Himalayas, the New Zealand Alps, Greenland, Antarctica, and the Arctic and Antarctic Islands (Barsch, 1996, Kääb, 2013). Based on recent space imagery, it can also be assumed that rock glacier-like features are located on the surface of Mars (Kääb, 2013).

4.1.1. Rock glaciers origins

The disagreements on the definition of rock glaciers reflect a long-standing academic debate about the origin of rock glaciers (Barsch, 1996, Berthling, 2011, Jones et al., 2019). Some researchers assume that the internal ice of the rock glaciers is of periglacial/permafrost origin (Barsch, 1996, Haeberli et al., 2006, Berthling, 2011, Jones et al., 2019), while others claim that it can also be originated from glaciers and that rock glaciers represent a continuum with

respect to mixing of ice and debris from variable sources (Whalley and Martin, 1992, Whalley and Azizi, 2003, Jones et al., 2019). Berthling (2011) called these two positions *permafrost creep school* and *continuum school*. He examined their debate and came to a conclusion that since rock glaciers are "visible expression of cumulative deformation by long-term creep of ice/debris mixtures under permafrost conditions", they would neither belong entirely to glacial or periglacial realm and it should be rather regarded as a cryo-conditioned landform (Berthling, 2011). Monnier and Kinnard (2015) suggested that rock glaciers can have periglacial, glacial and also mixed origins. They distinguished three different possibilities of glacier – rock glacier interactions that can result in rock glaciers:

1. The readvance(s) and superimposition/embedding of glaciers or debris-covered glaciers onto/into rock glaciers, with related geomorphological and thermal consequences (defined by the *permafrost school*)
2. The continuous derivation of a rock glacier from a debris-covered glacier by evolution of the surface morphology (see above) together with the conservation and creep of a massive and continuous core of glacier ice (defined by the *continuum school*)
3. The transformation of a debris-covered glacier into a rock glacier not only by the evolution of the surface morphology but also by the evolution of the inner structure, i.e. the transformation of the debris-covered continuous ice body into a perennially frozen ice – rock mixture by addition from the surface of debris and periglacial ice and fragmenting of the initial glacier ice core (Monnier and Kinnard, 2017).

Similarly, Schaffer et al. (2019) distinguishes three classes of rock glaciers based on their origins: glaciogenic rock glaciers are formed from debris-covered glaciers, cryogenic rock glaciers are formed from the geological processes associated with permafrost and polygenic rock glaciers have a combined glaciogenic and cryogenic origin (Schaffer et al., 2019).

4.1.2. Characteristics of rock glaciers

A fundamental characteristic of rock glaciers is their thermal state. In permafrost conditions, the surface layer consisting of debris prevent positive summer temperatures to reach down to the ground ice-containing permafrost body and the mixture of debris and ice remains frozen over the year, possibly even centuries (Haeberli et al., 2006, Kääb, 2013). Another important feature of rock glaciers is their displacement. The nature of the topography together with the pressure makes the ice-debris mixture of rock glaciers deform. In general, the movement of rock glaciers results a surface speed of centimetres to a few decimetres per year. However,

cases have been reported with surface velocities of several metres per year (Janke et al., 2013, Kääb, 2013, Jones et al., 2019). The surface speed depends on factors such as surface slope, composition and internal structure, thickness of ice-rich body or ground temperature (Kääb, 2013). Based on their kinematics, rock glaciers can be classified as active or inactive (Figure 5). *Active rock glaciers* can be characterised by distinctive flow-like morphometric features reflecting their visco-plastic properties. Some examples are ridge-and-furrow assemblages, steep and sharp crested front, light colour, swollen appearance and lack of vegetation cover (Barsch, 1996, Jones et al., 2019). *Inactive rock glaciers* do not contain enough ice for deformation and are therefore immobile. They generally have gentler, darker coloured frontal slopes and vegetation cover might also appear (Jones et al., 2018a, Barsch, 1996). *Relict rock glaciers* are in fact former rock glaciers that no longer contain ice. They generally have gentler and rounder slopes and might have extensive vegetation or even ponds on their surface (Giardino and Vitek, 1988, Barsch, 1996, Jones et al., 2018a). A fourth type is mentioned in some papers called pseudo-relict rock glaciers. It is an intermediate type between relict and inactive rock glacier, having locally isolated patches of permafrost (Barsch, 1996, Kellerer-Pirklbauer et al., 2010, Colucci et al., 2019).

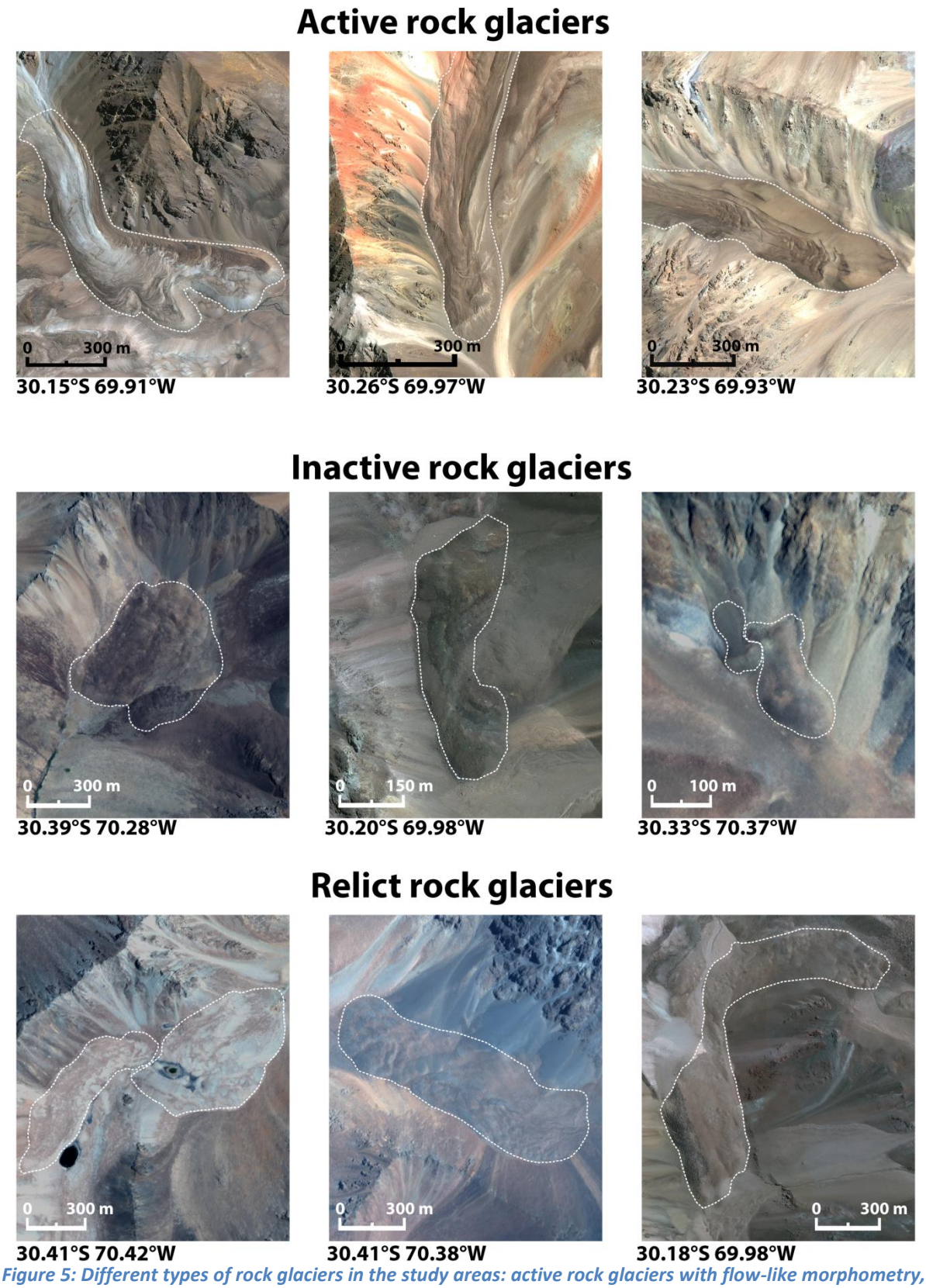

Figure 5: Different types of rock glaciers in the study areas: active rock glaciers with flow-like morphometry, furrows and light colour, inactive rock glaciers with gentler slopes and darker colour and relict rock glaciers with round slopes and ponds on their surface. The background images are the orthorectified Pleiades and SPOT mosaic maps (2020).

4.1.3.Rock glacier water storage and discharge

While glacier- and snowpack-derived meltwaters are heavily threatened by climate change, rock glaciers are climatically more resilient than glaciers as they respond to climate change at comparatively longer time scales. Therefore, under escalated climate warming, rock glaciers have an increased hydrologyical significance and become a larger component base flow to rivers and streams (Jones et al., 2018a). The water volume equivalent (WVEQ) of the world's rock glaciers is estimated to be 83.7 - 16.7 Gt, equivalent to ~68 – 102 trillion litres (Jones et al., 2018a, Jones et al., 2019). Figure 6 shows a more detailed distribution of WVEQ of rock glaciers around the globe.

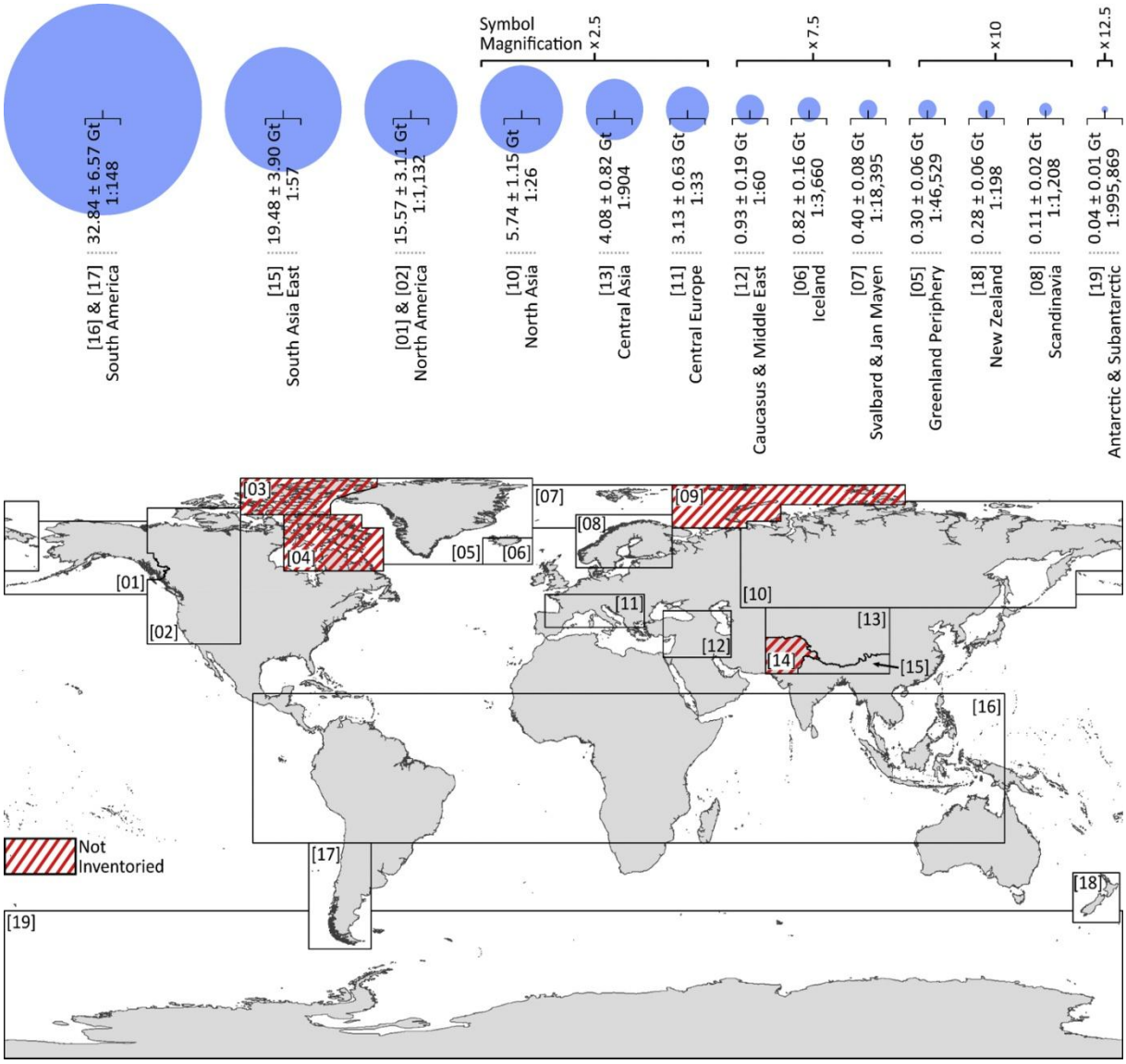

Figure 6: Near-global rock glacier WVEQ (Gt) and ratios of rock glacier-to-glacier WVEQ. Rock glacier WVEQs (blue circles) are sized proportionately to the whole. Rock glacier WVEQs reflect 50 ± 10% ice content by volume (Jones, et al., 2018).

Only a few studies have investigated the hydrological aspects of rock glacier water discharge. This is because of the lack of information on flowpaths and the extreme difficulty of rock glacier water discharge measurements with often multiple and/or inaccessible springs. Intact rock glacier discharge patterns are characterised by strong seasonal and diurnal variability, primarily determined by local weather conditions, the thermal conditions within the active layer (AL), and the physical mechanisms that control meltwater flow through the rock glacier (Krainer and Mostler, 2002, Krainer et al., 2007). Typically, discharge rates are highest during the spring/early summer snowmelt and gradually decline through summer and autumn to low or zero flow in the winter months. In addition, rock glacier discharge fluctuates strongly in response to rainfall events and periods of colder weather with snowfall (Jones et al., 2019). Apart from the study in the La Laguna catchment mentioned in Chapter 3, some other water discharge measurements have been carried out for example in the Canadian Rockies, where Gardner and Bajewski (1987) measured a water discharge of 90 – 270 L s^{-1} at the rock glacier *Hilda* or in the Alps, where Krainer and Mosler (2002) measured 5 – 310 L s^{-1} for the *Gößnitz* rock glacier in the Hohe Tauern Mountains. In the Central Andes of Argentina, the water discharge was measured at 2 – 5 L s^{-1} at the *Dos Lenguas* rock glacier (Schrott, 1996), and 230 – 1000 L s^{-1} at *Morenas Coloradas* (Trombotto et al., 1997).

4.1.4. Field surveys on rock glaciers

Fieldwork allows the geomorphological mapping of rock glaciers with terrestrial survey methods such as GPS, triangulation or laser ranging (Kääb and Weber, 2004). For example, Brenning et al. (2005) measured rock glacier front slope inclination in the dry Andes with a hand held clinometer. Mapping the internal structure of rock glacier bodies is usually more complicated. A few investigations used borehole drilling to gain information about the stratigraphy. Geophysical techniques can also be used: ground-penetrating radar (GPR) sends radar signals into the ground and receivers their reflection from layer boundaries or objects. High frequencies are used for high-resolution images of shallow structures while lower frequencies are used for deeper structures but with a lower resolution (Monnier et al., 2008). Fractions give information about rock glacier depth and internal composition. Monnier and Kinnard (2015a) conducted a GPR investigation on the surface of the *Llano las Liebres* rock glacier (located in the primary study area) and by recalculating the signal velocities and using fraction units, they gave a complete picture of a potential composition. Electrical resistivity tomography (ERT) measures the electrical resistivity of subsurface materials. By hammering

steel electrodes into the ground on every 2 metres and measuring resistivity with a georesistivimeter, Boaga et al. (2020) could make an estimation of the ratio of frozen ground in the *Schafberg* rock glacier in the Swiss Alps. The results were validated by temperature measurements. Guillemot et al. (2020) used seismic monitoring and checked the seasonal wave velocity changes in subsurface layers of different water content. Boreholes can also be used for study the mechanical processes: Arenson et al. (2002) took core samples and then installed temperature and deformation measurement tools to study the influence of internal structure and temperature on deformation. Other methods for deformation measurements, such as steel tapes or strain wires are also used (Kääb et al., 2003). If meltwater springs are accessible, water discharge can be measured with gauging stations and electrical conductivity sensors with salt dilution method, while water samples are taken for geochemical inspections (Krainer and Mostler, 2002, Krainer et al., 2007). Recently, an extensive study was carried out by Halla et al. (2021) in attempt to quantify ice content and water storage changes of an active rock glacier in the Dry Andes of Argentina by combining field measurements (ERT, and seismics) with remote sensing.

4.2. Optical satellite remote sensing

Remote sensing can be an effective solution for mapping mountainous areas that can be too time-consuming, dangerous or expensive to approach on field. Remote sensing is defined as the acquisition and measurement of information about certain properties of phenomena, objects or materials by a recording device not in physical contact with the features under surveillance (Khorram et al., 2012). It is an effective tool for rock glacier monitoring since it provides large coverage and repetitive acquisition (Khorram et al., 2012). Different types of active and passive satellite sensors exist. In this thesis, optical satellite RS will be in the main focus as the data used for the project were derived with that method. Before the availability of satellite images, aerial photos were used. Although they are still popular for rock glacier monitoring (Kääb et al., 1997, Kaufmann et al., 2018), the appearance of earth observation (EO) satellites in the latter half of the 20th century opened new horizons in the field of RS. EO satellites orbiting around the planet provide global coverage on a more regular basis (Khorram et al., 2012). Optical satellite sensors are passive RS systems that detect the solar radiation reflected from the surface. Most optical sensors produce multispectral images.

These sensors detect radiation in several wavelength bands of the electromagnetic range. The bands are typically the visible (red, green and blue) and infrared portions of the spectrum. Having information from different bands can be useful since different landcover types have a different reflectivity in each band (this is usually illustrated as reflectance curves, see Figure 7). It allows creating false colour composite images that allow visualising reflectance in wavelengths that are invisible for human eyes (Figure 7). These show that different landforms and landcover types have different reflectance on each band. Using different band ratios can be used to generate new data that show the statistical and mathematical relationship between the spectral bands (Schuckman and Dutton, 2018). In this way, band indices for different landcover types (NDVI for vegetation, NDSI for snow, NDWI for water, etc.) and other band ratios can be generated (Table 1) to highlight landforms. Some of them have proven to be useful for rock glacier classifications (Brenning, 2009, Kofler et al., 2020, Robson et al., 2020).

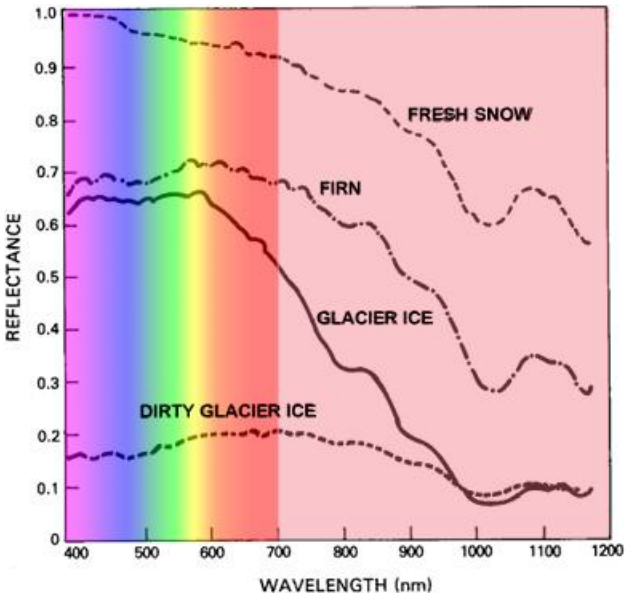

Figure 7: Reflectance curves of different types of ice within the visible and the infrared region (modified from Hall and Martinec, 1985).

Some satellites also produce panchromatic images that have a single band with information about the total light energy in the visible spectrum. It can collect higher amount of radiation per pixel and therefore is able to detect changes in smaller spatial extent. Thus, it has larger spatial resolution than the multispectral images (Mahyari and Yazdi, 2011).

Table 1: Popular indices used in landform classification.

Index acronym	Index name	Band formula
NDVI	Normalised Difference Vegetation Index	(NIR-Red) / (NIR+Red)
NDWI	Normalised Difference Water Index	(Green – NIR) / (Green + -NIR)
MNDWI	Modified Normalised Difference Water Index	(Green – SWIR) / (Green + SWIR)
NDSI	Normalised Difference Snow Index	(Green – NIR) / (Green + NIR)
SAVI	Soil Adjusted Vegetation Index	((NIR – Red) / (NIR + Red + 0.5)) * 1.5
LWM	Land and Water Mask	(SWIR/Green + 0.001) * 100

The possibility of different band compositions and ratios together with very high spatial resolution make optical RS extremely useful for remote sensing investigations. Its disadvantages include dependency on weather conditions, day, other environmental effects such as water column depth or clarity (Hedley et al., 2012) and the susceptibility to physical damage (McGrath and Ni Scanaill, 2013). Moreover, imagery with sub-metric spatial resolution can cost several hundred Euros depending on area size and sensor type.

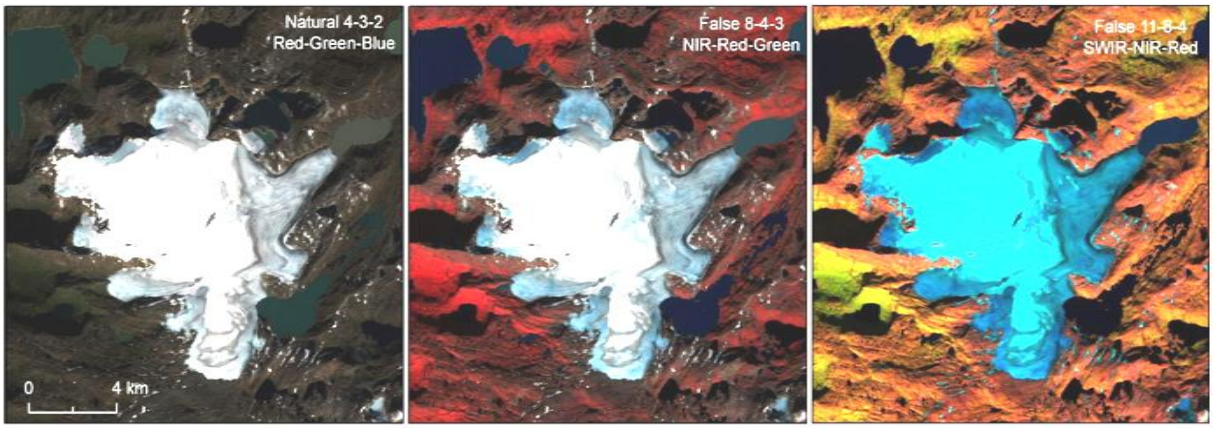

Figure 8: False colour composite variations of Sentinel-2 images of the Blåmannsisen glacier, Norway (Andreassen et al., 2021).

4.3. Digital Elevation Models

Digital elevation models (DEM) are 3D representations of the terrain. Freely available DEMs with large coverage are available. One of the most popular free DEM sets is the Shuttle Radar Topography Mission (SRTM) with a nearly global coverage and a spatial resolution of 1 arcsecond (30 m). Although SRTM is often the best DEM to find for a certain area, it should be noted that these products are from 2000 and therefore can be outdated. The 30 m spatial resolution of SRTM DEMs might also be insufficient to detect the morphology of smaller landforms. National DEMs created on a state level are generally more accurate and have a higher resolution. They exist for example in North America (Fereshtehpour and Karamouz, 2018), Europe (Wiederkehr and Möri, 2013) or Africa (Athmania and Achour, 2014). Freely available regional DEMs such as the ArcticDEM (Barr et al., 2018) or the High Mountain Asia DEM (Liu et al., 2019) also exist. Unfortunately, such national DEM dataset does not exist for the Chilean Andes.

The lack of suitable DEMs makes rock glacier investigations more difficult since elevation and topographic data are crucial for rock glacier mapping since the classification is usually based on geomorphometrical criteria. These include features like shape, slope steepness or surface topography (furrow and ridges) or relation to hillside (Villarroel et al., 2018b, Jones et al., 2019). Furthermore, by comparing two DEMs of the same area from different times, it is possible to detect changes in topography that indicate motion of active rock glaciers and allows the calculation of surface velocity. The lack of available national datasets often makes researchers create their own, project-specific DEMs. DEMs can be generated with different methods such as laser scanning (Triglav-Čekada et al., 2016), radar interferometry (InSAR) (Liu et al., 2013, Necsoiu et al., 2016, Villarroel et al., 2018a) or photogrammetry.

4.3.1. DEMs from photogrammetry

DEMs can be generated from optical imagery by using stereo-photogrammtery. This includes both aerial photos and optical satellite imagery. Photogrammetric determination of digital terrain models and their subsequent comparison is an effective a well-established technique to exactly define terrain surfaces or even their temporal changes (Kääb et al., 1997). The concept of photogrammetry is that by having at least two overlapping images of the same object taken from different positions, it is possible to retrieve 3D information or elevation. It uses the apparent displacement of an object viewed from different locations, a phenomenon called

stereoscopic parallax (Haldar, 2018). The absolute parallax is the distance between the principal point and the object on the image, it can be measured and by using geometric and parallax equations, the height of objects can be calculated:

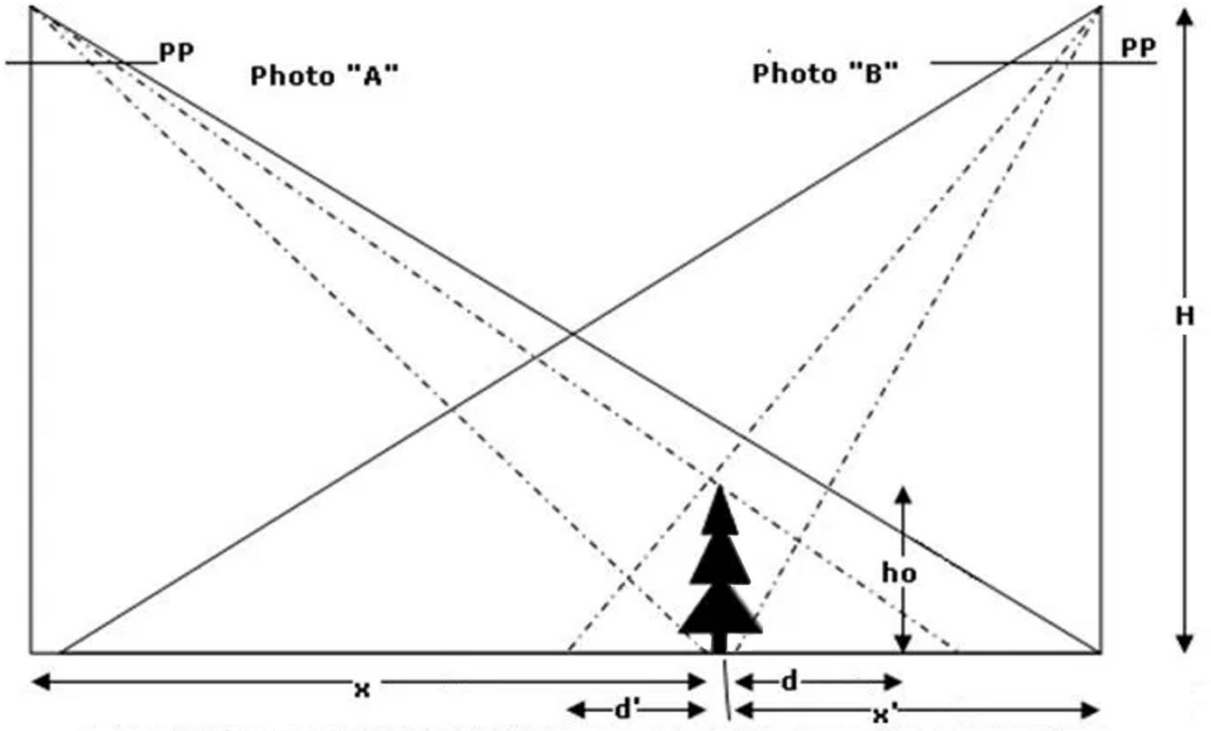

Figure 9: Simple example of stereo photgrammetry. The goal is to retrieve the height of the object (Hassani, 2018).

On the example by Hassani (2018) shown in Figure 9, H is the flying altitude, h_o is the height of the detected object, x and x' are the parallax of the object base on each image and d and d' are the displacement of the object base and object top. It can be seen that

$$\frac{h_o}{H} = \frac{(d + d')}{(x + x') + (d + d')}$$

x+x' can be defined as the absolute stereoscopic parallax and replaced with P, while d+d' is the parallax difference and can be replaced with ΔP. Therefore,

$$\frac{h_o}{H} = \frac{\Delta P}{P + \Delta P}$$

Thus, the height of the object is

$$h_0 = H\frac{\Delta P}{P + \Delta P}$$

, where H is the flying altitude, P is the absolute parallax and dP is the parallax difference between the top and the bottom of the object (Hassani, 2018). With today's computer technology, several tools have been developed to automatically extract DEMs from stereoscopic pairs (Gong and Fritsch, 2016, Shean et al., 2016). The general process of DEM generation consists of preprocessing the images (noise removal), matching corresponding points on them, triangulating (transforming image coordinates to ground coordinates) and geometrically modelling the satellite camera and the ground coordinate system (Wei and Bartels, 2012).

Both aerial and satellite photogrammetry have been used to generate DEMs for rock glacier monitoring. For example, Kääb et al. (1997) used aerial photogrammetry for the monitoring of the *Ruben* rock glacier in the Swiss alps . Monnier and Kinnard (2017) used DEMs from both aerial photos and GeoEye satellite image pairs to monitor the evolution of glacier – rock glacier transitional landforms in the Chilean Andes from 1955 to 2014. Bolch et al. (2019) used the technique as well on Pleiades and SPOT imagery to study the evolution and the ice content of ice – debris complexes in the Tien Shan region in Central Asia. Robson et al. (2020) used a Pleiades tri-stereo to extract a DEM for their automatic rock glacier detection. Photogrammetry has been recently used by Kääb et al. (2021) to create DEMs for rock glacier change monitoring in Tien Shan since the 50's.

4.4. Measuring surface velocity

With remote sensing data, it is also possible to detect the terrain's changes in time. Information on surface displacements and velocity can be useful to detect deforming landforms such as active rock glaciers.

4.4.1. Feature tracking

One solution is to examine the displacement of a landform by comparing multiple images taken at different times and tracking features between successive images. Feature tracking mostly use a computer-based normalized cross correlation algorithm that matches features on

the surface by giving an estimate of the similarity of image intensity values (Monnier and Kinnard, 2017, Debella-Gilo and Kääb, 2011). When performing feature tracking, it is crucial to choose an adequate search radius and a matching window that are used to identify features. The time interval between the images is also extremely important as the displacement should be significant enough to be measured while the feature needs to be still identifiable (Berthier et al., 2005). The method was used on rock glaciers by Monnier and Kinnard (2017), who investigated glacier-to-rock glacier evolution on both historical aerial photos and satellite images. Eriksen et al. (2018) tracked features to measure the acceleration of the *Ádjent* rock glacier, Norway on aerial photos and Blöthe et al. (2020) applied the technique on RapidEye satellite imagery to obtain surface velocity fields of active rock glaciers in the Argentine Andes.

4.4.2.Radar interferometry

Another method is Synthetic Aperture Radar Interferometry (InSAR), also known as Differential InSAR (DInSAR). In contrast to optical remote sensing, radar is an active remote sensing system as it sends microwave signals to the surface and receives the backscattered echo. The advantage of SAR remote sensing is that it is independent from weather conditions and sunlight. InSAR uses the phase difference of two radar images covering approximately the same area acquired at different times from slightly different positions. It can be performed when the correlation degree, known as coherence, between the images is sufficiently high. The phase difference is related to the surface – sensor distance (thus the elevation of the area) and it is possible to detect changes and deformations of the topography during the time interval of the two images (Liu et al., 2013). In order to exploit the surface displacement, the effects caused by the topography should be removed. When performing InSAR, an interferogram is created where phase values are mapped in the range π to $-\pi$. To get actual values, a process called phase unwrapping should be performed (Villarroel et al., 2018a). Since the displacement and the phase difference is proportional to the wavelength of the radar signal, surface velocity can be calculated. InSAR is a popular method for monitoring mountainous areas (Strozzi et al., 2020) including rock glaciers. For instance, Liu et al. (2013) described the kinematic state of 59 active rock glaciers in Sierra Neva, California while Strozzi et al. (2020) used InSAR to compute velocity time series of multiple active rock glaciers in the Alps, Greenland and the Andes.

4.5. Delineating rock glaciers on remote sensing data

Remote sensing techniques have quickly become essential tools for large scale mapping and classification of both artificial and natural objects. Different methods have been used to detect and delineate glaciers (Fang et al., 2015, Robson et al., 2015) and debris-covered glaciers (Robson et al., 2015, Lippl et al., 2018, Sahu and Gupta, 2018) using automated or semi-automated methods. However, these methods proved to be insufficient for rock glacier identification.

4.5.1. Challenges of rock glacier mapping

The special characteristics of rock glaciers require considerable efforts for their mapping process (Marcer, 2020). Because of their spectral similarity to the surrounding paraglacial bedrock where they originate from, rock glaciers are more difficult to detect on remote sensing data than glaciers or debris-covered glaciers. Moreover, the deformation of rock glaciers is often too low to maintain radar coherence and to use SAR for detection (Robson et al., 2020). Velocity rates from InSAR and feature tracking only allows the identification of fast deforming rock glaciers but not inactive ones. Therefore, most rock glacier inventories are made by using high-resolution optical imagery (Perucca and Esper Angillieri, 2011, Schmid et al., 2015, Barcaza et al., 2017, Jones et al., 2018b, Robson et al., 2020) since it allows large-scale geomorphological surveys (Jones et al., 2018a).

4.5.2. Manual delineation

Due to the previously mentioned challenges of rock glacier detection, automatic mapping methods are difficult to develop. Early rock glacier inventories were made manually. Wahrhaftig and Cox (1959) detected rock glaciers in the Alaska Range on air photos and recorded extensive rates of rock glacier movements by measuring the distance between the headwall and the boulders. Another example is Outcalt and Benedict (1965), who used manual delineation on vertical aerial photographs to examine the possible origins of rock glaciers of in the Colorado Front Range. Manual interpretation relies on identifying surface features indicative of rock glaciers such as ridges, furrow and steep frontal slopes (Jones et al., 2018c, Robson et al., 2020). The technique is still a fundamental method for rock glacier mapping (Scotti et al., 2013, Rangecroft et al., 2014, Jones et al., 2018c). The work most often takes place within a workspace of a GIS tool like QGIS or ESRI ArcGIS (Zeze and Liu, 2018), but other programs can be used as well. Tanarro et al. (2018) used the CAD software

Microstation to map debris-covered glaciers and rock glaciers, while Rangecroft et al. (2014), Jones et al. (2018) and Pandey (2019) used the freely available Google Earth Pro that provides high-resolution, usually cloud-free, orthorectified satellite and aerial imagery free of charge in contrary to costly commercial satellite imagery. It should be noted that the use of Google Earth impedes automation of workflows and analysis is restricted to the manual creation of polygons within the software (Robson et al., 2020). Non-optical data has also been used: for example, Villaroel et al. (2018) manually identified active rock glaciers of the Dry Andes on interferograms generated from Senitnel-1 images. The main advantage of manual delineation is that a human operator with good field knowledge is able to produce very accurate rock glacier inventories, although it makes the method inherently subjective (Jones et al., 2019). Further, the technique demands a significant amount of time and manpower and can be slow and tedious especially with large study areas.

4.5.3.Attempts for automation

While much effort has been put into automatic mapping and monitoring of glaciers based on satellite imagery, rock glaciers and also debris-covered glaciers have received less attention and constitute a greater challenge for remote sensing techniques since their debris surface does not produce a distinct spectral signal (Brenning, 2009). Early automatic methods classified each individual pixel by the value stored in them. Berta (1982) used spectral signatures from Landsat Multispectral Scanner (MSS) imagery and performed a maximum likelihood classification followed by various enhancement techniques on each band. However, she concluded that the techniques employed provided an insufficient method for accurate identification of rock glaciers and that Landsat MSS has proven to be ineffective (Berta, 1982). Based on Berta's (1982) findings, Janke (2001) used the thematic bands of Landsat Thematic Mapper (TM) imagery, image enhancement and DEM data to establish a modelling procedure for rock glacier identification. He used different combinations of enhancements and ran an unsupervised classification reaching an overall accuracy of 81.0%. The model had significant limitations due to the low resolution of the Landsat TM scenes (Janke, 2001). Brenning (2009) compared eleven different statistical and machine learning techniques in a benchmarking exercise for rock glacier detection. He used training points derived from SRTM and Landsat data. He found that the penalized linear discriminant analysis provided the best result with the detection of 70% of the rock glacier points (Brenning, 2009). Linear discriminant analysis is statistical method to separate classes and

determine their boundaries. Brenning et al. (2012) examined four different classification methods to detect rock glacier flow structures on IKONOS imagery using Gabor filters that are used for feature extraction and texture analysis. It was found that including texture to terrain attributes improves the classification accuracy.

Table 2: Overview of past methods of rock glacier mapping.

Delineation method	Advantage	Disadvantage	Examples
Manual interpretation on topographic maps	Easy and cheap access to maps Topographic and elevation information already depicted	Maps can be outdated or inaccurate Time-consuming	White (1979)
Manual interpretation on aerial photos	High-resolution images Existed before satellites (useful for historical investigation)	Air surveys are sporadic Data often difficult to access Sometimes only grayscale images are available Time-consuming	Wahrhafting and Cox (1959) Outcalt and Benedict (1965) Kaufmann et al. (2018)
Manual interpretation on satellite imagery	High-resolution images Global coverage on regular basis Imagery with multiple bands	Commercial products are costly Time-consuming	Falaschi et al. (2014) Monnier and Kinnard (2017) Kääb et al. (2021)
Manual interpretation on Google Earth	Very-high resolution, pre-processed imagery Free of charge	Data extraction is very limited Impedes automation Time-consuming	Rangecroft et al. (2014) Schmid et al. (2015) Pandey et al.(2019)
Pixel-based automatic classification on satellite imagery	Early attempts for automation Significantly faster method	Difficult to achieve good results Spectral values of single pixels are insufficient	Janke et al. (2001) Brenning (2009) Brenning et al. (2012)

4.6. Object-based image analysis

As the spatial resolution of satellite imagery has increased, the relationship between the objects to be classified and the pixel sizes has changed (Figure 10). Around the year 2000, GIS and image processing started to grow rapidly through object-based image analysis (OBIA) (Blaschke, 2010). OBIA creates near-homogenous objects, which serve as the basis of subsequent classification (Drăguţ et al., 2014, Robson et al., 2020). Some research refer to OBIA as Geographic object-based image analysis (GEOBIA) (Blaschke et al., 2014).

4.6.1. Difference between OBIA and pixel-based methods

Pixel-based image analysis (PBIA) analyses individual image pixels and the values contained in them. PBIA classifies pixels based on this information. This can be problematic when the spatial resolution of the image is too high or the target object is too complex and has pixels of different spectral values (e. g. parts of landforms that are covered with debris, snow, vegetation or shadow)(Figure 9). In contrary of PBIA, OBIA create meaningful-image objects, extracts their information and assess their characteristics in scale (Blaschke et al., 2014). It is also capable of classification based not only on spectral values but also spatial contextual information such as shape, texture and relationships between the objects (Blaschke, 2010, Rastner et al., 2014). The importance of contextual information in classification of landforms on remote sensing data has been well known in the scientific community for decades. Kettig and Landgrebe (1976) found that classifying individual pixels by not only their own spectral values but also those of their neighbours as well gives a better overview of the context of the scene and produces better results (Kettig and Landgrebe, 1976). As the spatial resolution of imagery is improving the role of contextual information is growing further. The use of the homogenous objects of OBIA also helps to avoid the salt-and-pepper effect cause by noisy pixels. Another main advantage of OBIA lies in its post-processing capabilities: it allows correcting reshaping, refining results or deleting false classifications (Rastner et al., 2014).

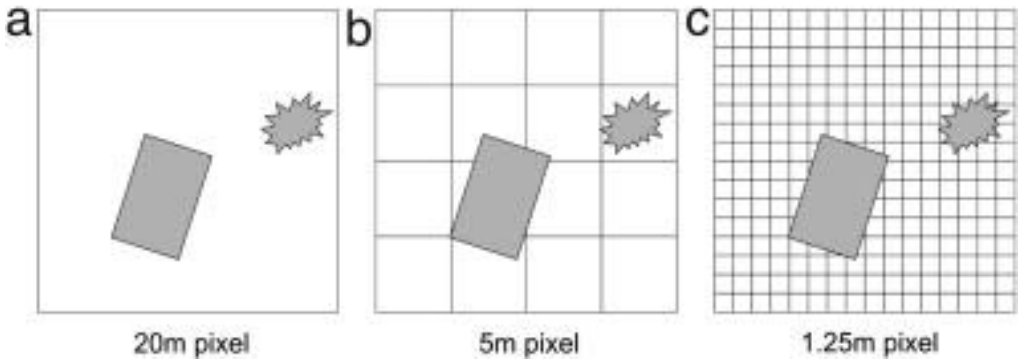

Figure 10: Relationship between objects under consideration and spatial resolution: (a) low resolution: pixels significantly larger than objects, sub-pixel techniques needed. (b) medium resolution: pixel and objects sizes are of the same order, pixel-by-pixel techniques are appropriate. (c) high resolution: pixels are significantly smaller than object, regionalisation of pixels into groups of pixels and finally objects is needed (Blaschke, 2010).

4.6.2.Multiresolution segmentation

According to Rastner et al. (2014), OBIA usually starts with the bottom-up process of multiresolution segmentation that merges the pixels of the image into groups (objects). Additional object hierarchical levels can also be used to further merge image objects (Figure 11).

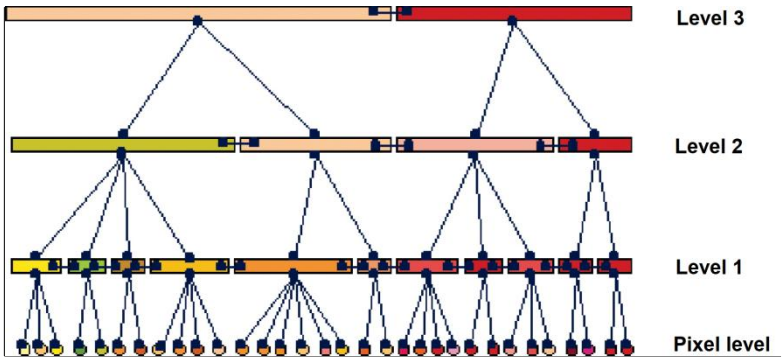

Figure 11: Hierarchical network of image objects with a three-level multiresoltuion segmentation (edited from Benz et al., 2004).

Multiresoltuion segmentation is based on three parameters: scale, shape and compactness. The *scale* parameter influences the size of individual objects and the *shape* defines the textural homogeneity of the resulting image object. Determining the right scale is crucial, since different regions are found at different scales of analysis. OBIA is linked with multiscale analysis concepts. Both one level representations (OLR) (Lang and Langanke, 2006) and multiscale segmentations (MSS) (Burnett and Blaschke, 2003) have been applied for OBIA. Both concepts have their advantage: For a high resolution image, for example, at coarse scales we can discriminate fields or forest stands, while at finer scales we can discriminate individual trees or plants: parameters and thresholds in a typical single-scale segmentation

algorithm must therefore be tuned to the correct scale for analysis. It is, however, often not possible to determine the correct scale of analysis in advance because different kinds of images require different scales of analysis, and furthermore, in many cases, significant objects appear at different scales of analysis of the same image (Blaschke, 2010). The parameter *compactness* optimizes the resulting objects in regard to the overall compactness within the shape criterion (Figure 12). Moreover, the input datasets such as the different satellite bands can be weighted in the process based on their importance in the segmentation (Robson et al., 2015). This allows influencing the creation of objects according to size, shape and number.

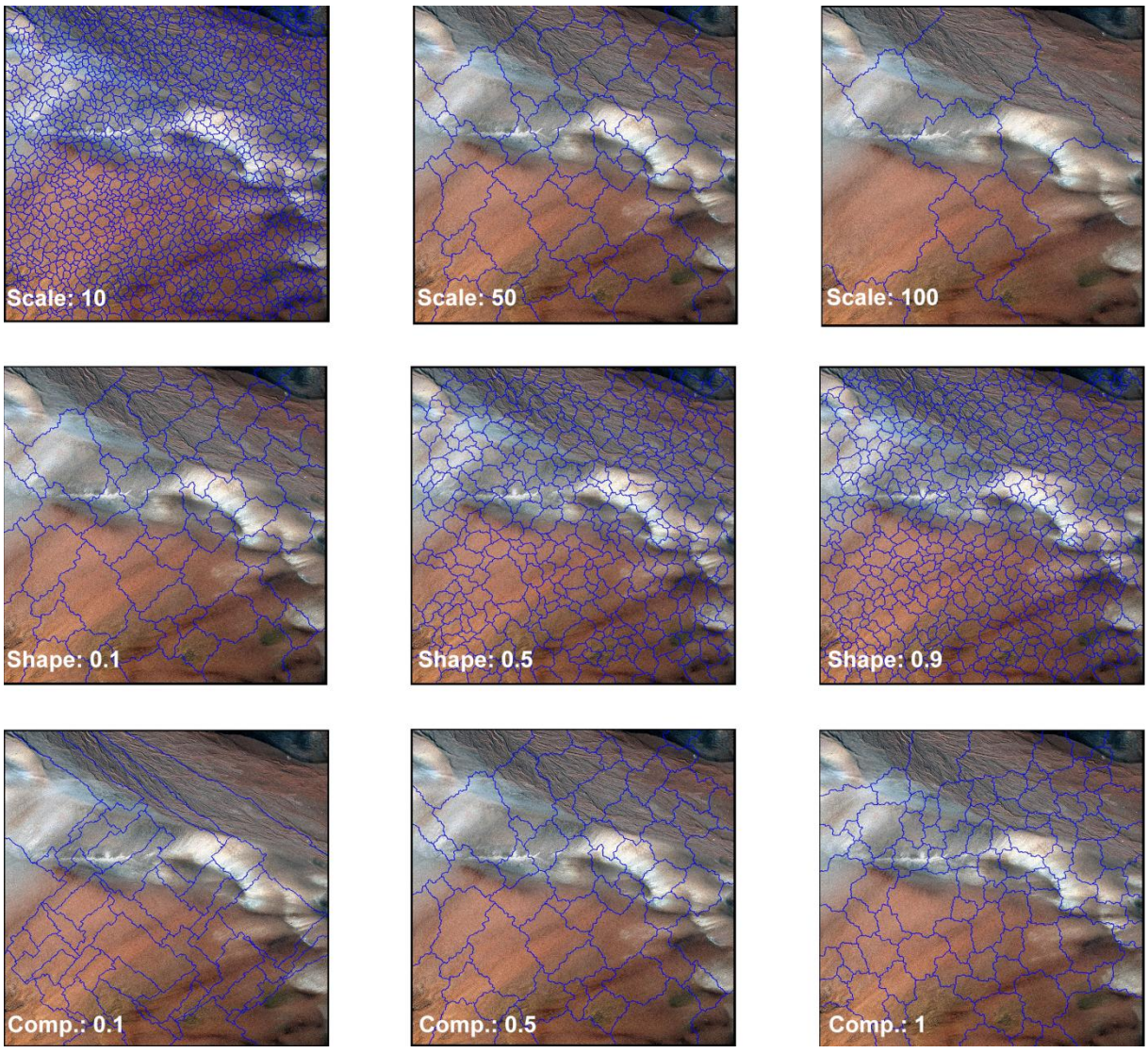

Figure 12: Results of multiresolution segmentations performed on an orthorectified Pleiades mosaic with different scale (top row), shape (middle row) and compactness (bottom row) parameters.

As Benz et al. (2004) state, to guarantee a definite hierarchy over the spatial shape of all objects, object borders must follow object boundaries of the one-step lower level and the lower segmentation must be constrained by the border of the one-step higher level. Further, it

is possible to perform segmentation levels with different parameters or data weighting and to correct object shapes by regrouping sub-objects (Benz et al., 2004). Its complexity makes image segmentation one of the most critical steps within OBIA (Drăguţ et al., 2014, Robson et al., 2020).

4.6.3.Classification methods

After the segmentation, the image can be classified. The classification can be performed with machine learning by using samples to train the algorithm to assign each image object to separate classes. Different supervised classification methods exist. One of the simplest algorithm is the k-nearest neighbour which determines the class of an object by investigating the k closest training samples (Ma et al., 2010). Another example, the random forest classification builds multiple decision trees based on randomly bootstrapped training data and takes the mode of the results (Sonobe et al., 2014). Support vector machine (SVM) is a widely used supervised classification method for classification of remote sensing data. It separates classes by creating a hyperplane that maximises the margin between the classes. The datapoints closest to the hyperplane are called support vectors (Ji and Gong, 2018). In a support vector classification, this hyperplane acts as a border between classes. SVM is the method of finding the best border between classes by using kernel functions. These machine-learning methods are suitable for tasks where the whole image needs to be classified (e. g. landcover mapping).

However, when there is only one target class that needs to be detected, another classification method called threshold-based classification can be more appropriate. This technique works on a threshold basis, which means the inclusion or exclusion of image objects based on their different characteristics. Various object features such as image layer values, area, shape, or relation to neighbouring objects can be set as fix thresholds via a trial-and-error basis. Values can also be set according to well-established classification procedures from the literature such as the band ratio or the combination of slope and thermal information (Rastner et al., 2014). A special type of threshold-based classifications is the fuzzy logic classification. Its name refers to how the objects are grouped by fuzzy propositional functions. Instead of using sharp thresholds, fuzzy logic gives objects values within the range 0 (false/non-member) to 1 (true/member). This way, fuzzy logic is much better in approximating the real world (Benz et al., 2004).

4.6.4.OBIA for glacier and rock glacier detection

OBIA has become an established method within remote sensing (Blaschke et al., 2014, Robson et al., 2020). It has been successfully used in many research studies to detect clean ice and debris-covered glaciers (Rastner et al., 2014, Robson et al., 2015, Kraaijenbrink et al., 2016, McNabb et al., 2016, Robson, 2016). Rastner et al. (2014) compared OBIA and PBIA for glacier mapping in Greenland, the Himalayas and Canada using Landsat and ASTER datasets. They found that OBIA outperformed PBIA with ~3 % in total and with 12% in the processing of debris-covered glaciers (Rastner et al., 2014). Robson et al. (2015) used OBIA to automatically map debris-covered glaciers. They concluded that OBIA gives better results when synthetic aperture radar (SAR) coherence is added to optical imagery and topography, and reached an accuracy of 91% against manually delineated outlines (Robson et al., 2015). When it comes to rock glaciers, fewer studies have been conducted on using OBIA for rock glacier mapping. Recently however, Robson et al. (2020) found that OBIA is suitable for classification correction and refinement for rock glacier detection carried out with a convolutional neurl network (see next section).

4.7. Convolutional Neural Networks

Convolutional neural networks (CNN) are a branch of deep-learning (DL) methods. They are inspired by the brain's neural networks, where neurons respond to particular features of the vision such as differently oriented edges. The concept of DL is to build a network which can similarly detect features on an input image. During the training, labelled samples from each class are sent through the CNN. The CNN transforms them to an output while learning progressively higher-level features (Litjens et al., 2017, Ma et al., 2019). CNNs typically consist of three different types of hierarchical structures: convolutional layers, pooling layers and fully connected layers (Ma et al., 2019, Robson et al., 2020). The input image is first convolved with a moving kernel filter of a fixed size that is looking for a distinct feature, for example a straight, horizontal edge. The input image and the feature are compared with a pixel value multiplication. A rectified linear unit (ReLU) activation function can be used to change all negative values to zero. This operation is repeated with every other feature filter. After the feature filters have hovered over every input, the results are stored in feature maps (Figure 13).

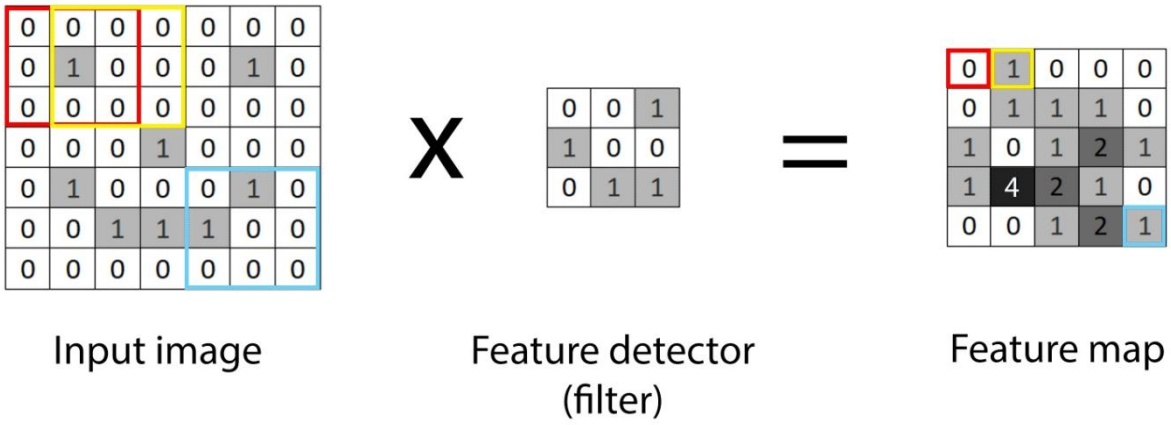

Figure 13: Work of a feature detector as it hovers over the input image (modified from Raju and Shanthi, 2020).

Pooling layers reduce the output's dimensions. Again, a fixed sized (usually 2x2) kernel is moved through the image and picks a representative value. The average pooling uses the mean value, while max pooling picks the highest one to represent the pixels under the kernel (Yani et al., 2019) (Figure 14). Multiple convolutional layers can be stacked up together and be interspaced by pooling layers (Robson et al., 2020).

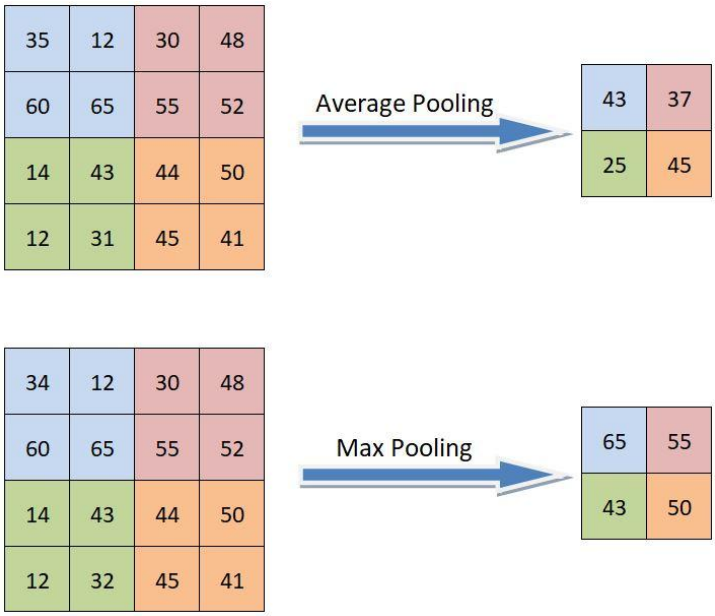

Figure 14: Outputs of a 2x2 average pooling and a 2x2 max pooling layer (modified from Yani et al., 2019).

The process where the input image is going through convolutions and pooling layers is called feature extraction (Phung and Rhee, 2019). The classification starts when the fully connected layer converts the filtered outputs into a vector. It compares to the vectors created from the training data by value division and determines a probability value for each class (Chatterjee, 2019) (Figure 15).

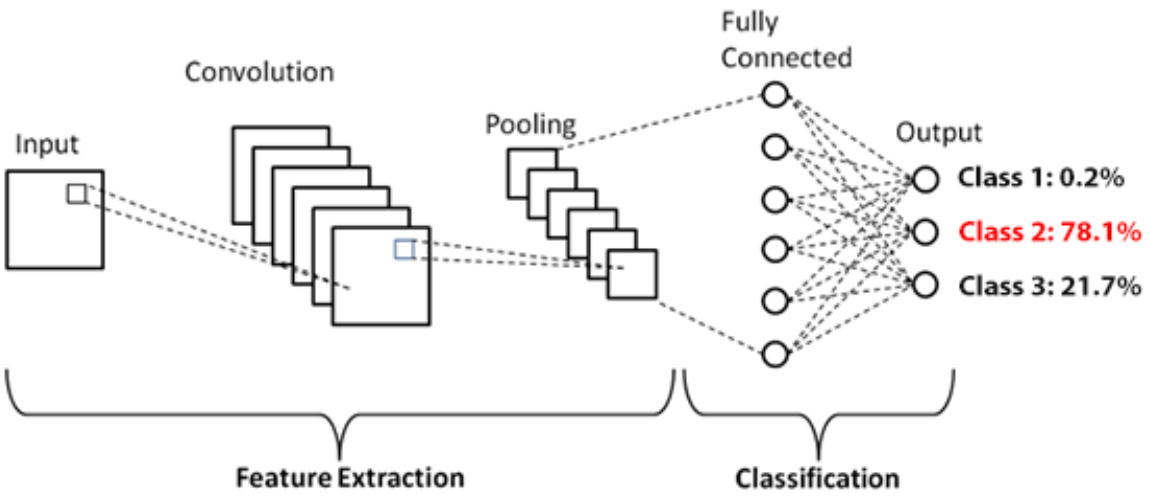

Figure 15: A schematic diagram of a basic CNN architecture. A feature detecting kernel is scanning the input image and performs the convolution. A pooling layer reduces the dimensions and the fully connected layer determines the probability of the input belonging to each class (modified from Phung and Rhee, 2019).

CNNs have made breakthrough in remote sensing image processing due to their ability to extract deep features (Li et al., 2020) They are typically used in applications where spectral characteristics alone are insufficient (Robson et al., 2020). It has been successfully used in many remote sensing investigations to automatically detect natural or artificial objects. As an example, Alshehhi et al. (2017) used CNN to extracted roads and buildings for urban landcover analysis. Csillik et al. (2018) detected individual citrus trees from high-resolution drone imagery, while Mohajerani et al. (2019) applied CNN to automatically map glacier calving margins on Landsat 5, 7 and 8 data.

4.7.1.Challenges of CNN

Being a relatively new method, CNN classification on RS data has its own difficulties. Early CNNs had problems with preserving the spatial reference of the input data and using multilayer features to improve the scene classification from different aspects (Erzhu et al., 2017). Song et al. (2019) have listed the challenges of classification with CNN on remote sensing data as follows:

1. Insufficient training data in RS: training datasets are much less than image datasets in the computer vision since the preparation of RS training data are time-consuming. RS

scientists who devote to deep-learning-based research are limited, and less of them pay more effort in RS training dataset production.

2. RS image-specific CNN models: there is a need for studies on CNNs that work with data acquired with different sensors.
3. Time efficiency: The majority of studies focus on classification accuracy and very few on CNN's time efficiency during training.
4. High-level CNN-based applications in RS image classification: More attention should be drawn in higher level CNN-based applications, e.g., high-accuracy extraction of semantic information on scenes, extraction of more complex objects, super-resolution reconstruction, multi-label remote sensing image retrieval and so on.

Another potential issue is the phenomenon of under- or over-fitting. If the architecture is too simplistic or the training is not extensive enough, the CNN will be under-fitted and will fail to adequately recognize objects. On the other hand, if the CNN is too deep and over-parameterized, over-fitting may occur. Over-fitting makes the model highly biased by the training data and its ability to generalize becomes weak (Wang et al., 2018) which may lead to misclassifications of inputs that differ too much from the training samples.

4.7.2.CNN for rock glacier mapping

Two studies have been conducted on CNN detection of rock glaciers. Marcer (2020) extracted points from rock glaciers and stable ground from SPOT 6 optical imagery, and trained a CNN with a model architecture of 3 convolutional layers (each with a 3 x 3 kernel) and a max-pooling layer after the first convolutional layer. The CNN was tested on another area where it successfully identified around 60-70% of the rock glaciers, although the heatmap produced contained a significant number of false positives (Figure 16/a). Robson et al. (2020) performed an analysis using Sentinel-2, Pleiades imagery and topography information. A CNN was built and trained with the model architecture 3x3x70, 7x7x40, 3x3x20, 1x1x12, 3x3x12 with max pooling applied after the third and fifth layers. To fix the false results of the CNN heatmap, the results were then further refined with OBIA using multi-level image segmentation and threshold-based classification. The classification had a total accuracy of 72% on Sentinel data and 76.8% on Pleiades (Robson et al., 2020) (Figure 16/b).

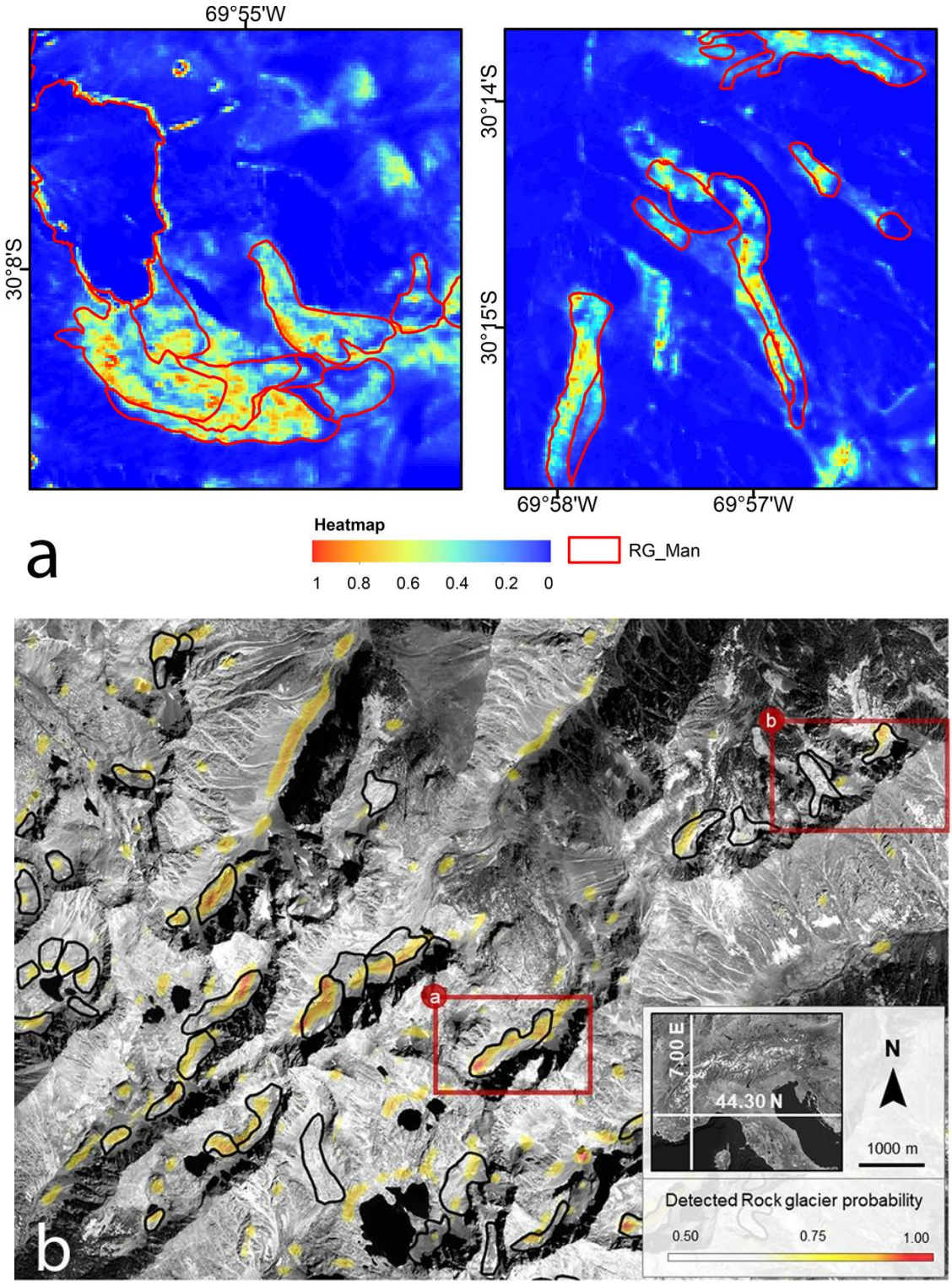

Figure 16: Rock glacier heatmaps in comparison with manual outlines created by Marcer (2020) [a] and Robson et al. (2020) [b].

5. Datasets

The objective was to test the new method not only on different areas but also on different sensors. Therefore, for this project work, imagery from different satellites was needed. New images from Airbus Defence and Space (Airbus DS) owned satellites were ordered through an application at the European Space Agency (ESA): two Pleiades tri-stereos with a resolution of 0.5 m and a SPOT 7 tri-stereo with a resolution of 1.5 m were obtained. One Pleiades tri-stereo covers the entire Tapado region, including the La Laguna catchment. The second Pleiades tri-stereo covers the southern area of Estero Derecho while the SPOT 7 images cover the northern part (Figure 17). As the data were used for a research project, the products were provided by ESA free of charge. A freely available SRTM elevation model was also downloaded to be used as a reference when collecting ground control points and tiepoints during the pre-processing (see chapter 6). An overview of the datasets used is shown in Table 3.

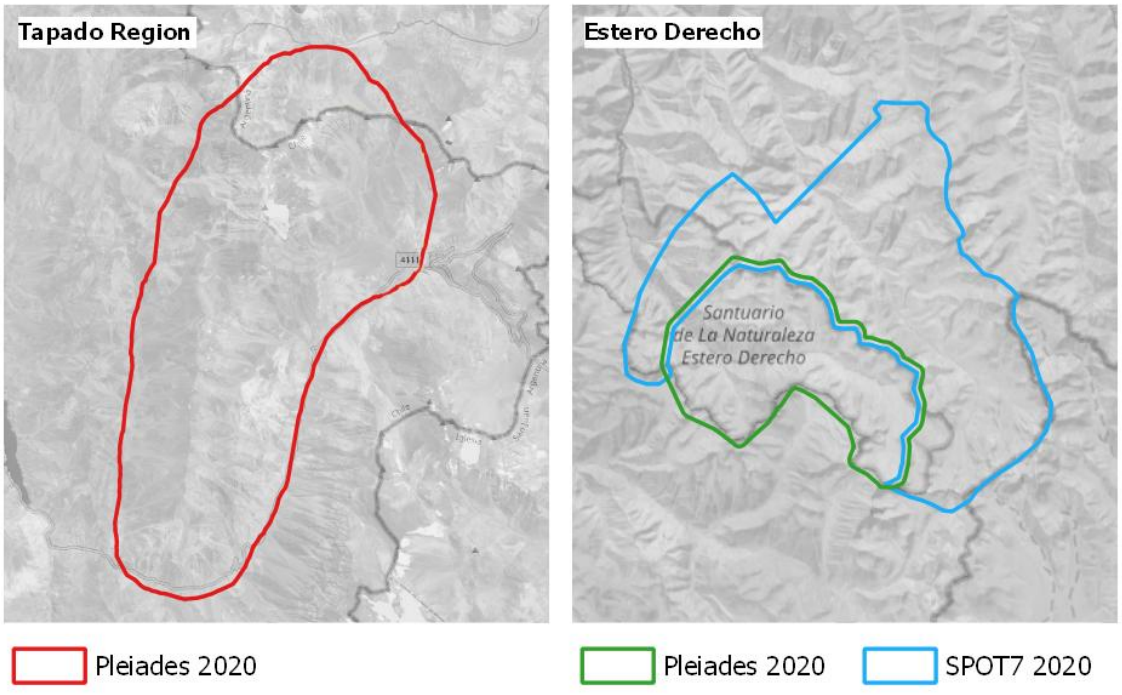

Figure 17: Coverage of the satellite imagery acquired.

Table 3: Datasets used for the investigation.

Scene ID	Date	Sensor	Resolution (m)	Area
DIM_PHR1B_202003011456539_SEN_4839452101	01/03/2020	Pleiades	0.5	Tapado
DIM_PHR1B_202003011457165_SEN_4839453101	01/03/2020	Pleiades	0.5	Tapado
DIM_PHR1B_202003011457376_SEN_4839562101	01/03/2020	Pleiades	0.5	Tapado
DIM_PHR1A_202001031453393_SEN_4749701101	01/03/2020	Pleiades	0.5	Estero Derecho
DIM_PHR1A_202001031454241_SEN_4749701101	01/03/2020	Pleiades	0.5	Estero Derecho
DIM_PHR1A_202001031453300_SEN_4749701101	01/03/2020	Pleiades	0.5	Estero Derecho
DIM_SPOT7_202003021424185_SEN_4835547101	02/03/2020	SPOT 7	1.5	Estero Derecho
DIM_SPOT7_202003021424467_SEN_4835548101	02/03/2020	SPOT 7	1.5	Estero Derecho
DIM_SPOT7_202003021424326_SEN_4835549101	02/03/2020	SPOT 7	1.5	Estero Derecho
SRTM_S31W071	11-22/02/2000	SRTM	30	30-31°S; 70-71°W
SRTM_S31W070	11-22/02/2000	SRTM	30	30-31°S; 69-70°W

6. Methods

After obtaining all the necessary images, the processing started; the workflow can be divided into three main steps: pre-processing, classification and result analysis. For this project, multiple different GIS and image processing tools were used for the specific steps. The pre-processing and the CNN testing were initially run on a 64-bit operating system with an Intel® Core™ i5-6300HQ CPU @ 2.30GHz and 8 GB RAM. This was later replaced by a more powerful machine, a 64-bit operating system with an Intel® Core™ Processor (Haswell no TSX) CPU @ 2.50GHz (16 processors) and 64 GB RAM. A detailed overview of the workflow is depicted in Figure 18.

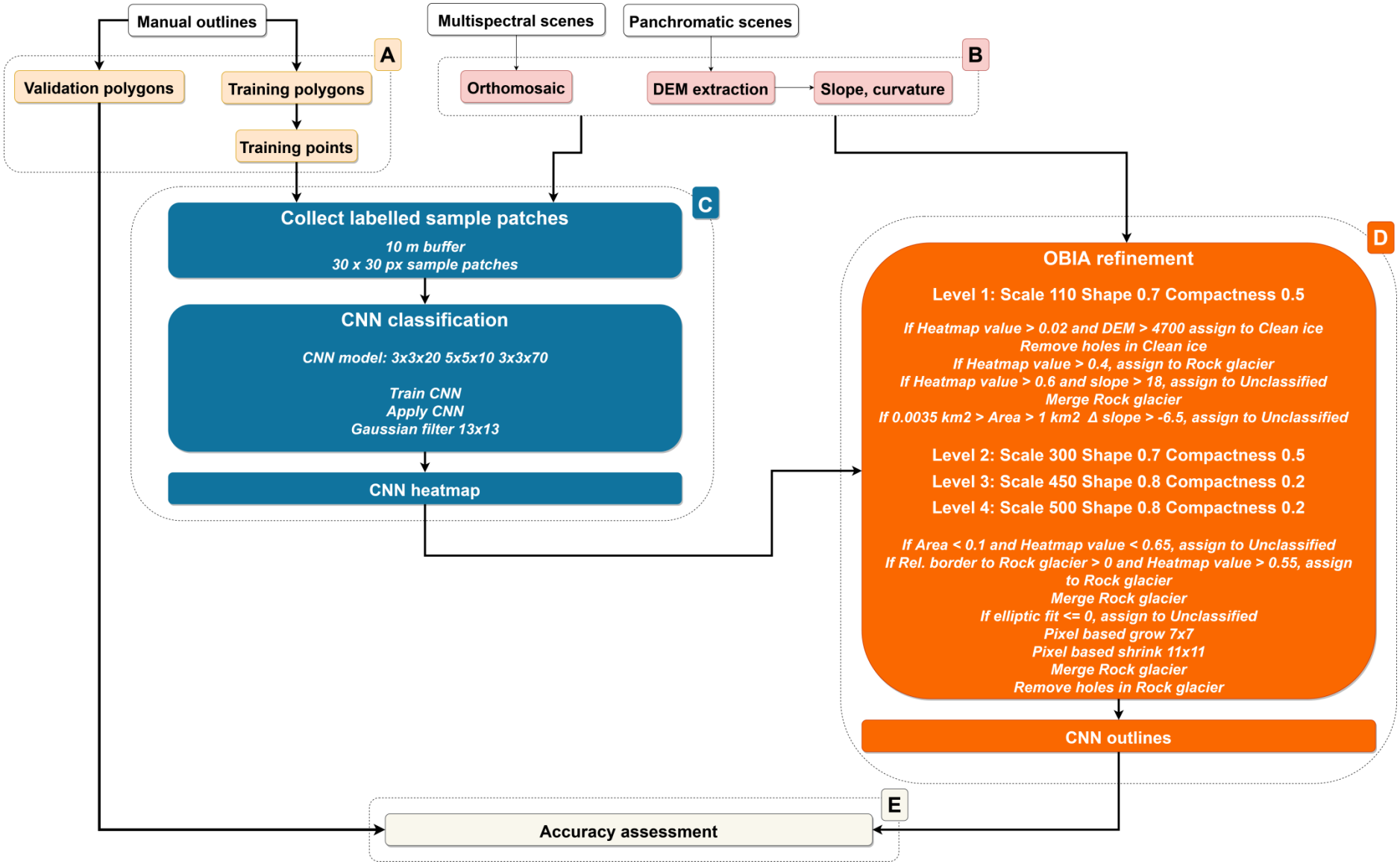

Figure 18: Chart of the workflow: Training and validation data creation in QGIS (A) Image pre-processing in PCI Geomatica (B), CNN classification (C) and OBIA refinement in eCognition (D) followed by an accuracy assessment in ArcGIS (E).

6.1. Image pre-processing

The optical tri-stereo images ordered from ESA came with a multispectral and a panchromatic image. The first goal was to use the panchromatic scenes to extract elevation information by generating an elevation model and then use that to retrieve slope and curvature information. The pansharpened spectral bands were used to create high-resolution orthomosaics. To keep consistency, every pre-processing step was executed on all products by using the same parameters. For pre-processing, the image processing software PCI Geomatica (today known as Catalyst) was used.

6.1.1. DEM extraction

The panchromatic bands of stereo and tri-stereos were used for DEM extraction with satellite photogrammetry. The Geomatica tool OrthoEngine allows DEM extraction from panchromatic scenes with collecting ground control points (GCP) and tiepoints (TP). Since every set of imageries had a rational polynomial coefficient (RPC) file that allows the software to determine the location of the data with high precision, only tiepoints were collected. Tiepoints were collected automatically by using a Fast Fourier Phase Matching algorithm. To limit the search radius not only in XY but also a vertical Z direction, it is possible to enhance the TP collection accuracy by using an existing DEM. For this reason, a standard 30 metre SRTM DEM was used which is freely available to download. After collecting tiepoints, the XY residuals were checked for each. Points with large residuals were inactivated and the model was recomputed until the overall residual was below 0.1 pixels. In total, 50 tiepoints were used for the Pleaides tri-stereos and 46 for the SPOT 7 tri-stereo. Following this, epipolar images were created for all three images to increase the speed of the correlation process and to reduce the possibility of incorrect matches. As a DEM extraction technique, the more time-consuming yet more precise Semi-Global Matching (SGM) method was applied. SGM has been shown to outperform the Normalised Cross-Correlation method and thereby produce cleaner DEMs (Hirschmuller, 2008). The pixel sample interval was set for a spatial resolution of 1 metre for the two Pleiades DEMs and 3 metres for the SPOT DEM. Lower intervals would cause nearly the same DEM accuracy but with an exponentially longer processing time. Since the study areas are almost entirely free of artificial objects and vegetation, a surface model was sufficient and did not need further corrections (Figure 19).

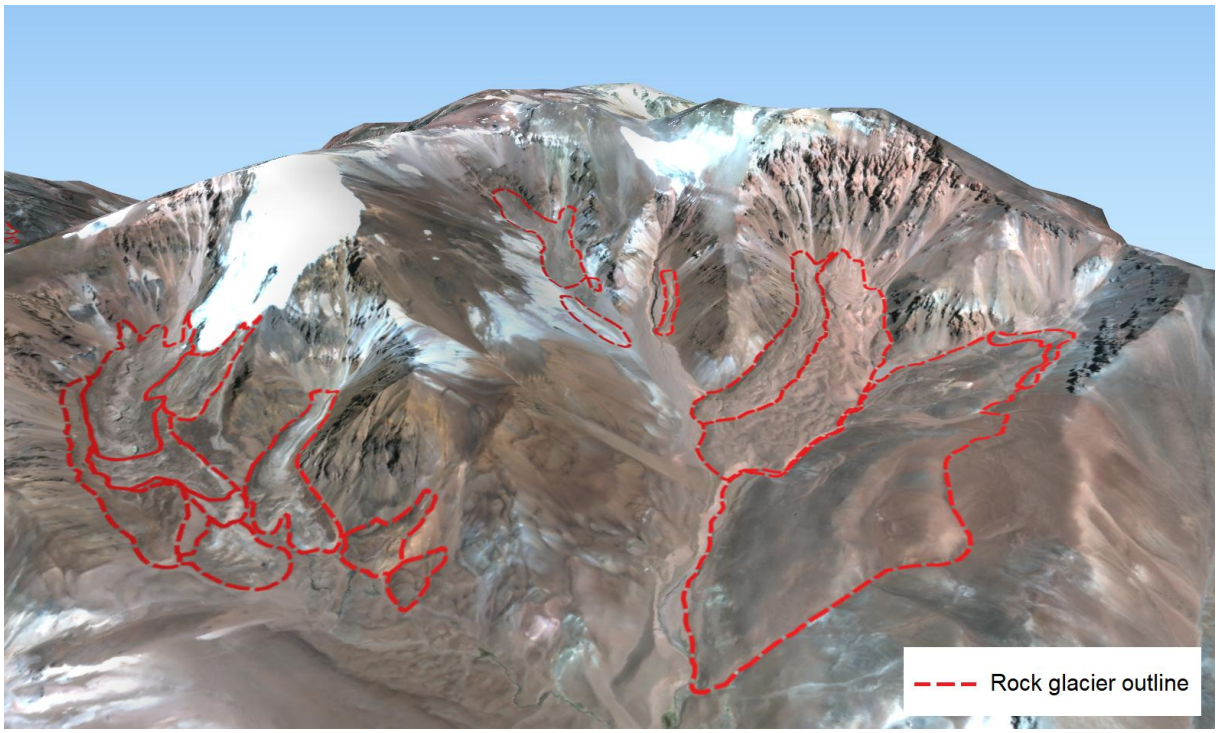

Figure 19: 3D view of the Tapado glacial complex using the extracted Pleiades DEM and orthomosaic.

6.1.2.Slope and Curvature Extraction

Elevation rasters allow the extraction of additional geomorphometric features. Slope layers were extracted from each DEM by using the Geomatica algorithm SLASP (Slope and Aspect). SLASP uses elevation values held in a DEM to calculate the corresponding slope and aspect angles. The slope algorithm used in this function is pixel-based, meaning that there is no second- or third-order polynomial surface fitting process. This also means that the slope and aspect maps may uncover some existing artifacts from the elevation channel. The values in the slope channel range between 0 and 90 degrees, and are used to describe the angle of incline or decline at a given pixel (Geomatica, 2020). The SLAPS algorithm is based on the method defined by Corripio (2003).

Planform and profile curvature layers were extracted with ESRI ArcGIS. Planform curvature relates to the convergence and divergence of flow across a surface. The profile curvature is parallel to the slope and indicates the direction of maximum slope. It affects the acceleration and deceleration of flow across the surface. The planform curvature (commonly called as plan curvature) is perpendicular to the direction of the maximum slope (ESRI, 2016) (Figure 16). A subset of the extracted topographic layers is shown in Figure 21.

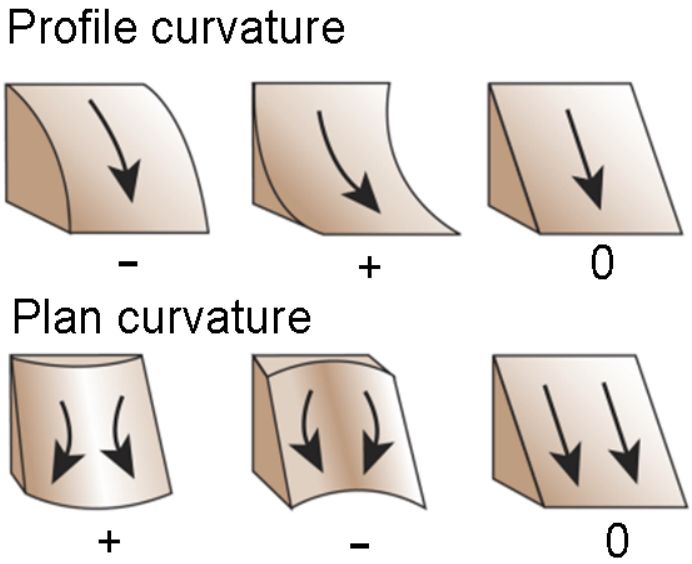

Figure 20: Profile and plan curvatures (ESRI, 2016).

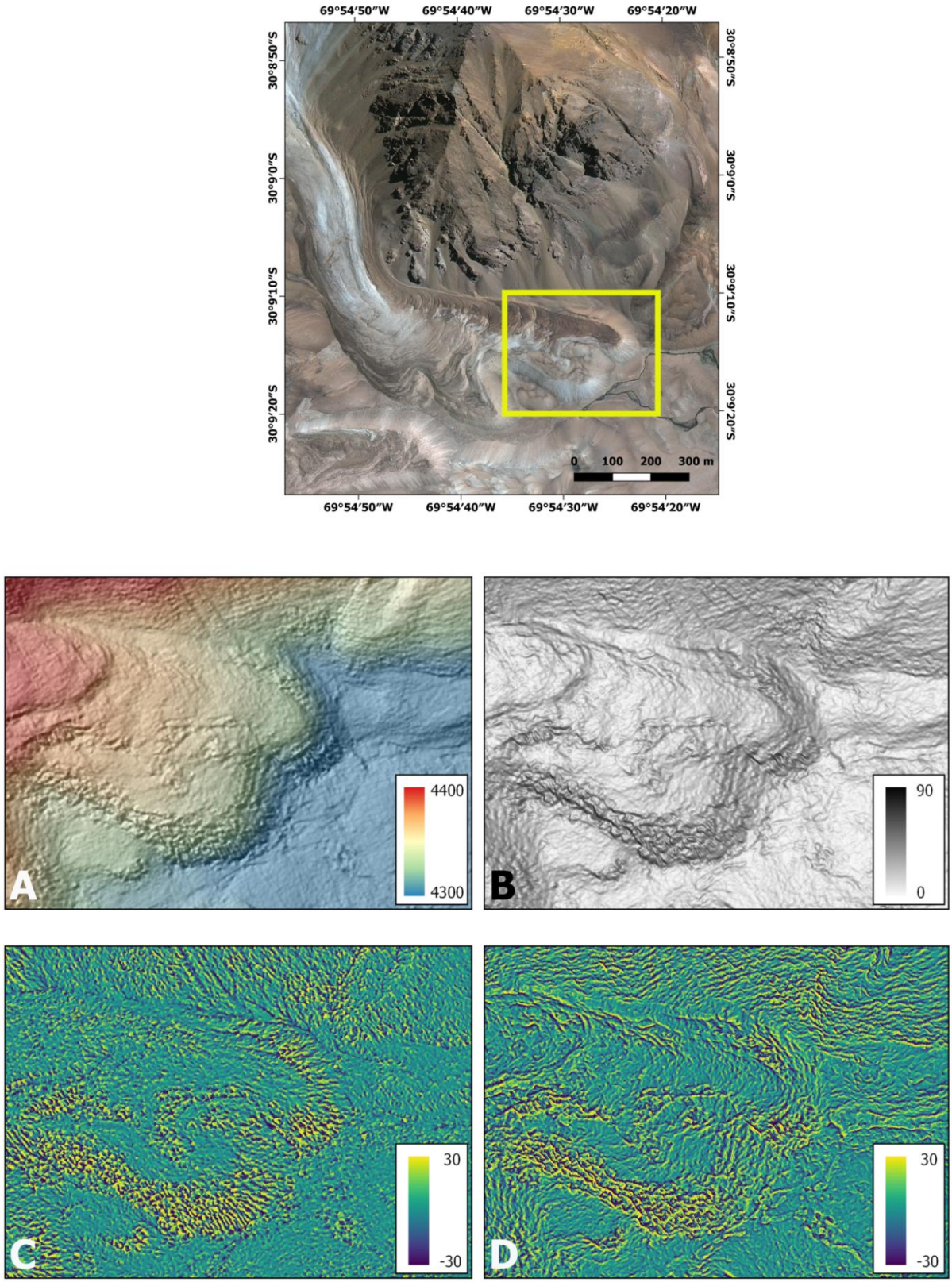

Figure 21: DEM with hillshade (A), slope (B), planform (C) and profile curvature (D) layers of the Las Tolas rock glacier extracted from a 2020 Pleiades tri-stereo.

6.1.3.Atmospheric correction

RS images are often degraded due to atmospheric effects. When the radiation travels to the atmosphere, it may be absorbed or scattered by the constituent particles of the atmosphere (Tyagi and Bhosle, 2011). Therefore, the radiance detected by the sensor does not consist only of the radiance reflected by the ground but also radiance from the atmosphere. Atmospheric correction needs to be applied to remove radiances from other sources and extract the reflectance of the surface. These effects on satellite images depend on several factors such as area location, acquisition date/time, weather conditions or sensor type. For a transferable pre-processing method for images from different date and satellites, atmospheric correction was necessary for the project. Several methods for ground reflectance estimation exist (Bilal et al., 2019). In this project, the tool ATCOR (Atmospheric and Topographic Correction) described by Richter & Schläpfer (2005) was used to perform atmospheric correction. Embedded in Geomatica, ATCOR extracts information such as solar zenith, azimuth, calibration coefficient or ban-channel combination from the metadata of the images to reduce the atmospheric and illumination effects like haze. ATCOR provides several workflows for atmospheric corrections: The *Top of the Atmosphere (TOA) Reflectance* workflow is the most basic one of them. The workflow converts pixel values to physical reflectance, as measured above the atmosphere. It normalizes images based on radiance values and image acquisition times, using only the required image information. The *Haze Removal* workflow allows calculating water and clouding masks for the input scene, and removing haze from images before performing atmospheric correction, thematic classification, or creating a mosaic. The ATCOR *Ground Reflectance* workflow allows calculating the reflectance values at ground level to remove atmospheric effects in satellite imagery, preparing the images for analysis under different atmospheric conditions. The workflow generates a reflectance image at ground level, corrected from atmospheric (aerosol type and water vapour) and terrain effects (Geomatica, 2013).

6.1.4. Orthomosaic generation

Since the multispectral bands had a lower resolution than the panchromatic bands, they were first pansharpened in order to create the most detailed orthomosaic. The multispectral and the panchromatic images were fused to obtain an image with a spectral resolution of the former and a spatial resolution of the latter. This was followed by orthoimage generation and mosaicking. During the mosaic preparation, a cutline was automatically generated and colour balancing was applied. The final orthomosaic was used to get high-resolution spectral information for the image classification.

6.2. Layer preparation

After creating/processing all satellite derived information, the layers were prepared for the classification.

6.2.1. Ground truth data

For training and testing the classification, an ESRI shapefile of manually delineated landforms were used as reference. The ground truth data was based on a glacier/rock glacier inventory by Nicole Schaffer and Shelley MacDonell (2020) from CEAZA. It was originally used by Robson et al. (2020) for their rock glacier detection and was corrected after several over and underestimates of rock glacier size and missing polygons were noticed (Robson et al., 2020). The attribute table included landform classifications made by the DGA and CEAZA. The shapefile was imported to QGIS where 30% of the polygons were randomly extracted as validation polygons. The remaining 70% was declared as training polygons. This was followed by a random sample point generation within the training polygons. Approximately 6000 points were generated: ca. 500 within the rock glacier outlines and ca. 150 for clean-ice. The largest proportion of the area was stable ground; therefore the remaining points were assigned to the stable ground category. The new *la_laguna_training_points.shp* was then exported. For the Estero Derecho region, a new landform inventory was provided by CEAZA. The outlines were primarily made by Eduardo Yañez under the supervision of Nicole Schaffer and Shelley MacDonell and it is based on Digital Globe, SPOT and GeoEye imagery from 2006-2014 along with Google Earth Pro. The inventory was cut to the area of interest (AOI)

of the two zones and exported as *estero_pleiades.shp* for the area covered by the Pleiades data and *estero_spot.shp* for the area of SPOT imagery. A field *cnn_class* was created in each shapefiles to store the classes to use in the CNN classification: *rock_glacier*, *clean_ice* or *stable_ground*.

6.2.2. Rescaling

When using CNN in eCognition, the algorithm generates a probability heatmap for each class ranging from 0 to 1 (Robson et al., 2020). This requires every input layers to have values normalized between these two numbers. Furthermore, the CNN tool in eCognition needs every layer bands to have a bit depth of 32. Therefore, before importing them to eCognition, every image bands were transformed in Geomatica with the SCALE tool. The output value range was set to 0 to 1 and the bit depth to 32-real. The bands were then loaded into the eCognition project.

6.3. Deep-learning

Once every data file was prepared, the deep-learning stage in eCognition Developer could start. The classification workflow was mostly based on previous papers on CNN in eCognition (Csillik et al., 2018, Timilsina et al., 2019, Robson et al., 2020) as well as the official CNN tool manual by Trimble. The first classification included the multispectral, elevation and slope layers. For the second one, curvature layers were added to compare the final results and find out if curvature can make an improvement. For the simplicity, these two classification methods were respectively named *CNN_noCurv* and *CNN_wCurv* classifications. A project file in was created with the rescaled image layers imported along with the *la_laguna_training_points.shp* shapefile.

6.3.1. Create classes

A buffer of 10 metres was added to every training point, creating circular regions. A chessboard segmentation was then performed with an object size of 100,000 to create small groups of pixels as objects. The objects that were overlapping with the buffer zones of the training points were assigned to the class defined in the *cnn_class* field of training point shapefiles (rock glacier, clean ice or stable ground). This way, the targets become larger then a single pixel which allows having more samples available to train the CNN.

6.3.2.Create labelled sample patches

Labelled sample patches were created for all three classes with a size of 30x30 pixels. In total, 20,000 labelled patches were collected. 5000 samples were generated for rock glaciers. Since the largest proportion of the images was comprised of stable ground, a greater number (13,000) of samples was created for stable ground. Being much easier to detect due to its spectral features, only 2000 samples were collected for clean ice. The samples were stored in TIFF format.

6.3.3.Build and test CNN

The experiment of finding the best CNN model used a trial and error basis. To save time, four small test areas with prominent rock glaciers were defined. If the CNN gave good results on all of the subsets, it was tested on the whole area. The model that proved to be the most accurate one had the architecture 3x3x20, 5x5x10, 3x3x70 with max pooling applied to the first and third layer (Figure 22). The model was trained on the sample data with a learning rate 0.0015. A 13x13 Gaussian smoothing was applied to the results and the heatmaps for all three classes were saved as three bands of a single TIFF file (Figure 23).

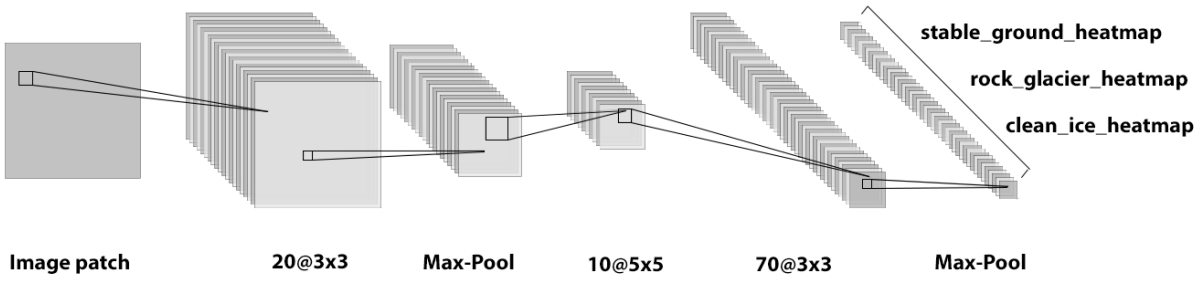

Figure 22: Diagram of the CNN architecture that proved to be the most effective for rock glacier detection.

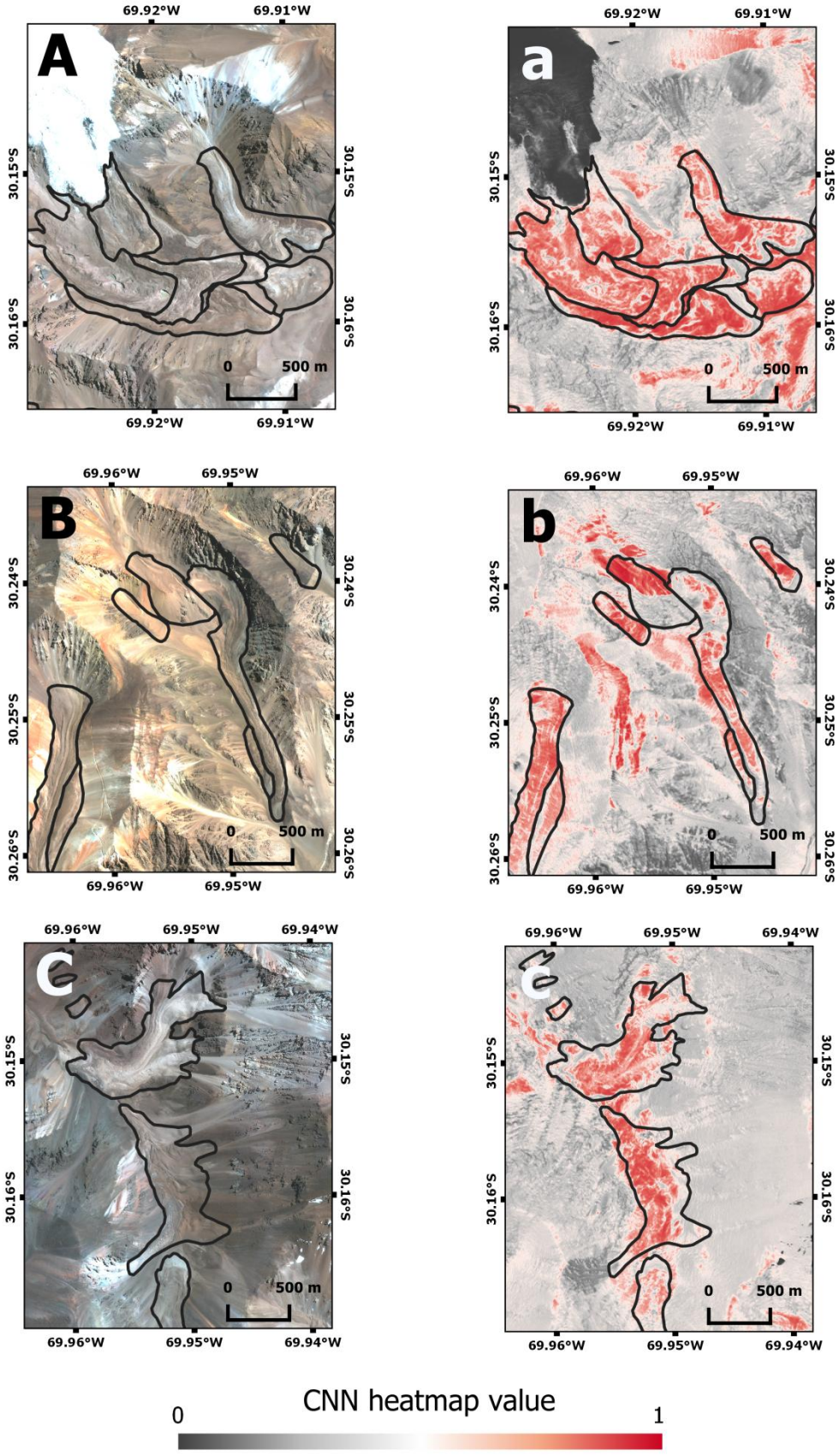

Figure 23: Manually corrected rock glacier outlines on the Pleiades orthomosaic (A – C) and on the CNN heatmap (a – c).

6.4. OBIA

To refine the results, a new project was opened in eCognition. This time, the unscaled image layers were used in order to use original values instead of numbers between 0 and 1. This is especially useful when defining slope or elevation thresholds. In total, 4 different levels of multiresolution segmentation were performed with classification steps on the first and fourth (Table 4). The first level had a scale of 110 with shape and compactness parameters of 0.7 and 0.5. This level was used to first classify clean ice, identify rock glacier hotspots with high heatmap values and delete false positives. By using trial-and-error, the scale and shape values were gradually increased while the compactness was decreased. The final level had a scale of 500 with 0.8 for shape and 0.2 for compactness. All segmentation levels used a weight of 1 for the spectral layers and 2 for slope (Table 4).

Table 4: Parameters of multiresolution segmentations.

Segmentation	Scale	Shape	Compactness	Weights	Operation
Level 1	**110**	**0.7**	**0.5**	RGB+NIR: 1 Slope: 2	Clean ice classification; detection of rock glacier "hotspots"
Level 2	**300**	**0.7**	**0.5**	RGB+NIR: 1 Slope: 2	-
Level 3	**450**	**0.8**	**0.2**	RGB+NIR: 1 Slope: 2	-
Level 4	**500**	**0.8**	**0.2**	RGB+NIR: 1 Slope: 2	Rock glacier expansion/refinement; stable ground classification

6.4.1. Classification of clean ice

The first task after performing the first level of segmentation was to detect areas with clean ice and exclude it from further analyses. The spectral characteristics make clean ice suitable to be delineated by solely using OBIA (Robson et al., 2015). In this paper however the CNN results were used to make sure the model is capable of recognising all classes from the training data. First, image objects with a clean ice heatmap value more than 0.02 and a mean elevation higher than 4700 m were extracted and assigned to the class *Clean ice*. The, holes

enclosed by clean ice objects were removed and neighbouring objects were merged. The outlines were then exported as shapefiles.

6.4.2.Identifying rock glacier hotspots

The next step was to identify the areas where the rock glacier heatmap values were high and where the expansion can be started from:

- Areas where the rock glacier heatmap value was more than 0.5 (50% probability) were extracted
- Then, due to the large number of false positives, a slope threshold was used to remove gentler areas
- The results were merged together
- Objects that were too small or too large for being rock glaciers were removed
- Finally, a threshold for slope difference to neighbours was applied

6.4.3.Expansion and refinement

Further refinement of the outlines was performed after the fourth level of multiresolution segmentation.

- A threshold using the newly calculated mean heatmap values was applied to remove more false positives
- Then, the remaining outlines were expanded using the neighbouring objects with higher heatmap values
- Objects with a too irregular shape were removed by using the elliptic fit feature
- Finally, the holes were filled and pixel-based grow (kernel 7x7) then shrink (kernel 11x11) were applied to refine the outlines
- The results were exported as shapefiles

6.4.4. Application on the other areas

eCognition allows saving the finished ruleset in a special .dcp format which then can be loaded and used within other eCognition workspaces. After finalizing the ruleset, both the CNN classification and the OBIA refinement was saved and the methods were repeated on the

2020 Pleiades data and the 2020 SPOT 7 data of Estero Derecho. Since these scenes did not contain clean ice, the steps for its classification were skipped.

6.5. Accuracy assessment

After creating the outlines for every study site, the accuracy of the classification was quantified by comparing the total area percentage classified as rock glacier with the manual outlines. Due to its simplicity, this method neglects errors of omission and commission, which over large areas can cancel each other out (Robson et al., 2020). Therefore, a confusion matrix was generated in ESRI ArcGIS by using 1000 randomly generated points to calculate the user accuracy (the percentage of correct classification) and the producer accuracy (the percentage of rock glacier areas that were successfully detected by the method). The kappa coefficient which indicates how much the accuracy has been influenced by coincidence, was also calculated.

7. Results

Overall, the three study zones contained 37.59 km^2 of rock glaciers according to the manual reference. The first *CNN_noCurv* classification that used the spectral bands, elevation and slope managed to classify 31.82 km^2 which means a slight underestimation of 15.4% and a total accuracy of 84.6%. When plan and profile curvature layers were included in the classification, *CNN_wCurv* resulted in much more false positives with a total rock glacier area of 56.38 km^2. In this case, an extremely high overestimation of 50.01% can be observed, which produced an overall accuracy of 49.99%. *CNN_noCurv* had relatively satisfying values within the confusion matrix with user accuracies ranging between 58.3 and 80.2% giving a mean user accuracy of 72.83%. Producer accuracies ranged between 64.0 and 98.4% which indicates a mean producer accuracy of 78.4%. With planform and profile curvature layers added to the input set, the average user accuracy from the three computed confusion matrix of *CNN_wCurv* was 71.23% while the mean producer accuracy was 76.43% which can be considered as good (see the comparison with previous methods in chapter 8). The mean kappa coefficient was 0.69 for both *CNN_noCurv* and *CNN_wCurv*. The results are summarized in Table 5.

The results were also exported to the cloud-based GIS software ArcGIS Online and are now available online as an ESRI ArcGIS webmap on:
https://www.arcgis.com/home/item.html?id=4afd394ad36542cdadf115196dfbfb35

Table 5: Overview of all classification results.

Sensor	Area	Rock glacier area (km²)	Classification	Area mapped (km²)	Underestimation (%)	Overestimation (%)	Area accuracy (%)	User accuracy (%)	Producer accuracy (%)
Pleiades	La Laguna catchment (validation only)	5.39	***CNN_noCurv***	6.82	26.46	-	**73.54**	**90.6**	**59.2**
			CNN_wCurv	5.45	0.15	-	**81.59**	**89.7**	**81.4**
Pleiades	La Laguna catchment (whole area)	12.01	***CNN_noCurv***	8.39	43.16	-	**56.82**	**80.2**	**72.8**
			CNN_wCurv	11.39	5.44	-	**94.56**	**86.7**	**74.1**
Pleiades	Estero Derecho – North	11.11	***CNN_noCurv***	8.88	25.11	-	**74.89**	**80.0**	**64.0**
			CNN_wCurv	11.71	-	5.40	**94.60**	**80.8**	**63.6**
SPOT 7	Estero Derecho – South	14.47	***CNN_noCurv***	14.55	-	26.85	**73.15**	**58.3**	**98.4**
			CNN_wCurv	33.28	-	190.15	**0**	**46.2**	**91.6**

7.1. Pleiades imagery

The analysis for the La Laguna catchment and the northern side of Estero Derecho was performed using Pleiades imagery. These two areas together contain 23.13 km^2 of rock glaciers. The first *CNN_noCurv* classification mapped 20.28 km^2 and reached an accuracy of 85.95%. *CNN_wCurv* method had a similar result mapping 20.10 km^2, thus, its accuracy on these areas was 84.93%.

7.1.1. La Laguna catchment

The first study zone was the La Laguna catchment. It should be mentioned that this was the area where the training of the CNN was done and where 30% of the rock glaciers were used for validation. The validation polygons had a total area of 5.39 km^2. In this case, *CNN_withCurv* outperformed *CNN_noCurv*. While the former mapped 5.47 km^2 reaching an overestimation of 0.15%, the latter detected 6.819 km^2, indicating and overestimation of 26.46%. This shows an accuracy of 73.54% for *CNN_noCurv* and 98.59% for *CNN_wCurv*. To assess the entire classification of the area, a confusion matrix was computed. *CNN_noCurv* had a user accuracy of 80.2% a producer accuracy of 72.8% and a kappa coefficient 0.75. *CNN_wCurv* had better results with a user accuracy of 86.7% and a user accuracy of 74.1%. When looking at the whole catchment, both *CNN_noCurv* and *CNN_wCurv* managed to map the majority of the landforms: 51 out of the total 70 (Figure 24).

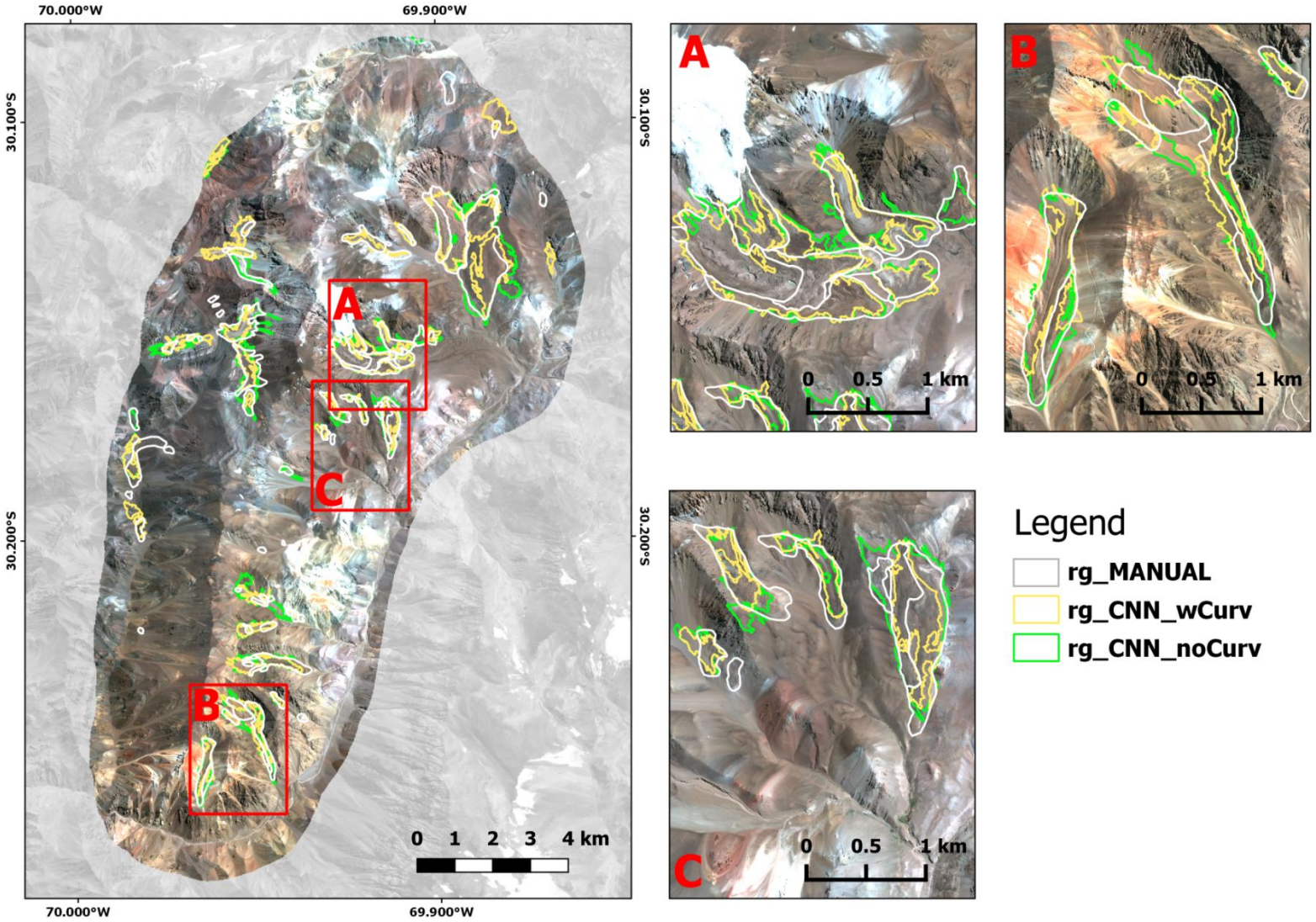

Figure 24: Comparison of the CNN_noCurv, CNN_wCurv and the manually corrected rock glacier outlines for the La Laguna catchment. The map shows that the presence of most rock glaciers was detected by both classifications. Background image is the orthorectified 2020 Pleiades mosaic.

7.1.2.Estero Derecho

On the second Pleiades imagery, *CNN_wCurv* proved to be more accurate again. It was able to map 31 rock glaciers out of a total 48, while *CNN_noCurv* found only 24 (Figure 25). While the confusion matrix showed roughly similar values (~80% user accuracy, ~64% producer accuracy, 96-97% total classification accuracy), *CNN_wCurv* mapped 11.71 km^2 out of 11.11 km^2 reaching an slight overestimation of 5.40% and an accuracy of 94.6%. In contrast, *CNN_noCurv* which detected only 8.88km^2 that caused an underestimation of 25.11% and an accuracy of 74.89%. The kappa coefficient was 0.69 for both classifications.

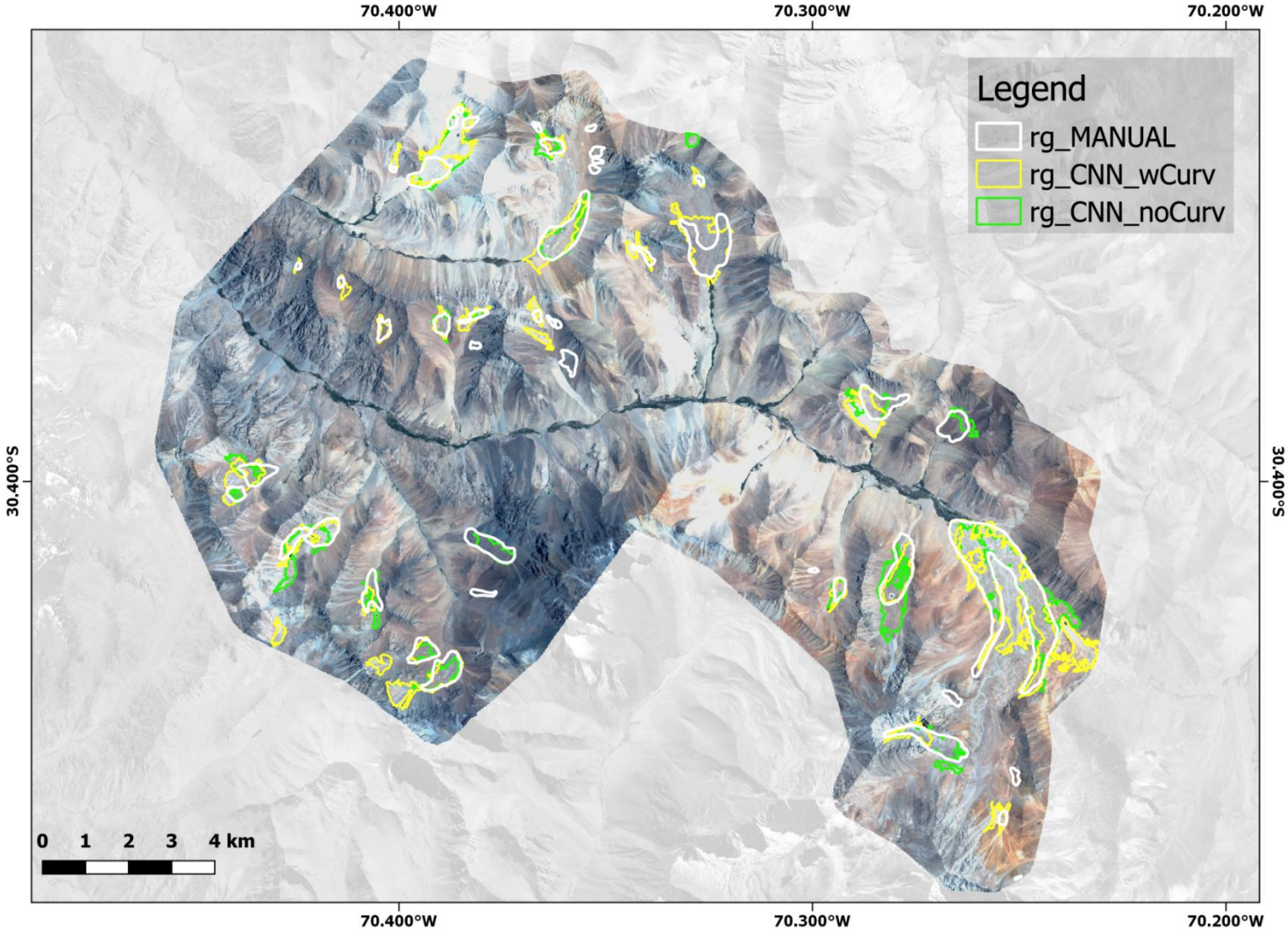

Figure 25: Comparison of the CNN_noCurv, CNN_wCurv and the manually corrected rock glacier outlines for southern side of Estero Derecho. Background image is the orthorectified 2020 Pleiades mosaic.

7.2. SPOT7 imagery

The northern side of Estero Derecho was covered by lower resolution SPOT 7 imagery. When transferred the method to SPOT data, *CNN_noCurv* successfully detected 43 out of the 125 landforms classifying 14.55 km^2 as rock glacier (Figure 26). Compared to the original 11.47 km^2, this represents an overestimation of 26.85% and an accuracy of 73.15%. The user accuracy was 70% and the producer accuracy 58.3%. The kappa coefficient was 0.63. On the other hand, the values of *CNN_wCurv* dropped drastically after the transfer to SPOT 7 data. Although it was able to detect the presence of 32 features, *CNN_wCurv* resulted in a large number of false positives of a total area of 33.28 km^2 which is almost three times as large as the actual rock glacier area and therefore the total accuracy was 0%. The user accuracy was measured at 14.6% while the producer accuracy at 46.2%.

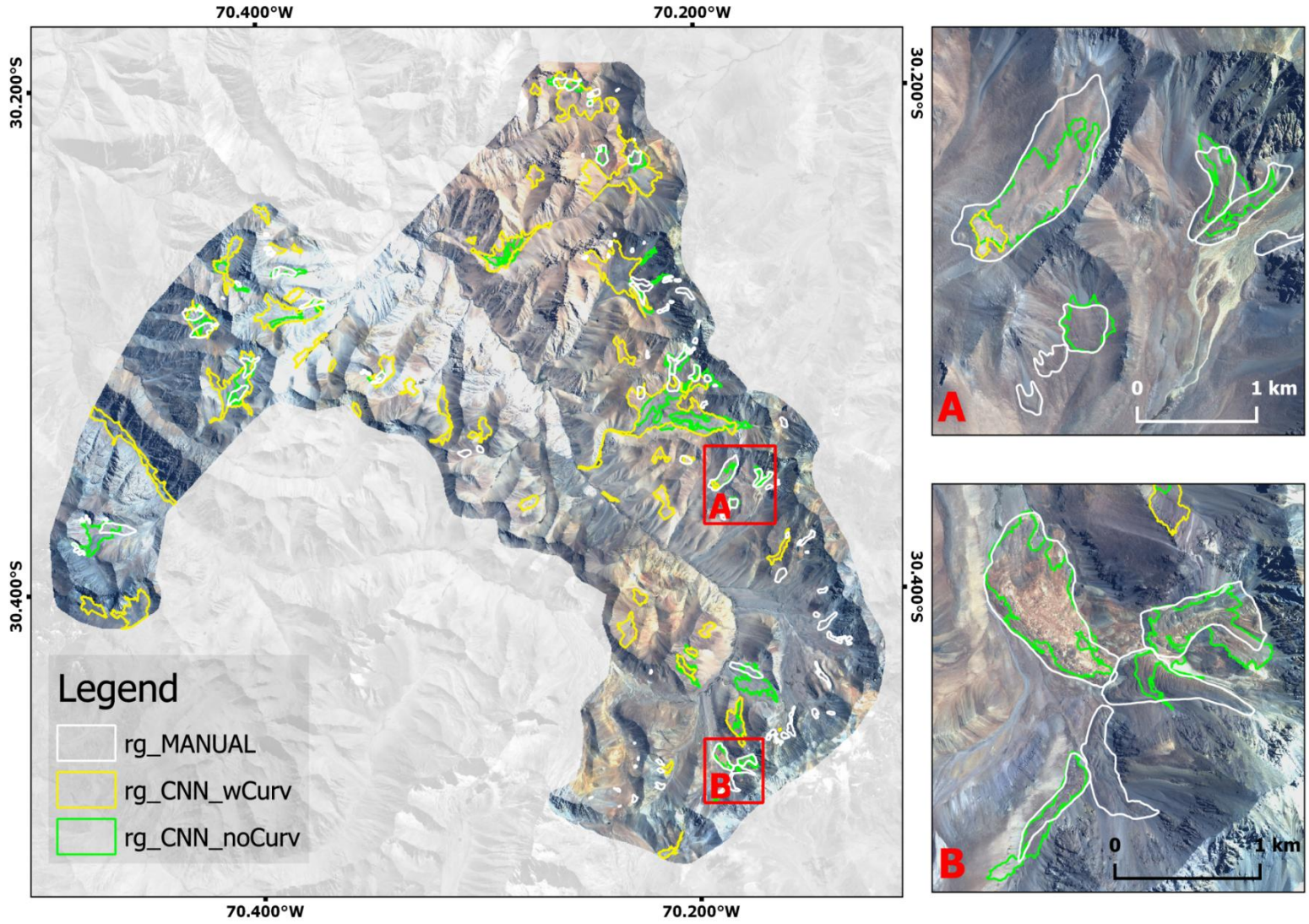

Figure 26: Comparison of the CNN_noCurv, CNN_wCurv and the manually corrected rock glacier outlines for northern side of Estero Derecho. As subsets A and B show, many rock glaciers could be mapped only by CNN_noCurv while CNN_wCurv proved to be highly inaccurate. Background image is the orthorectified SPOT mosaic.

7.3. Accuracy of individual rock glaciers

The accuracy for individual rock glaciers has also been studied. The area of each landform was extracted from both the manually corrected inventory and the CNN classifications. However, some rock glaciers that were spatially close to each other have been identified as one landform by the CNN or have been merged together as a result of the OBIA refinement. In these cases, the combined area of the landform assemblages was used as reference. Overall, both classifications managed to detect the largest landforms while the lowest accuracies were in general those of the smallest rock glaciers.

7.3.1. Results for CNN_noCurv

When the curvature layers were not included, the classification mapped 29 rock glaciers or groups of rock glaciers larger than 0.05 km^2 out of a total 32. Using the same area-based benchmark, 20 out of 25 landform groups were succesfully detected on the Pleiades imagery showing the southern Estero Derecho. On the Pleiades imageries, very small rock glaciers were mostly missed by the classification, medium sized (between 0.05 and 1 km^2) ones were mapped rather accurately while very large ones were classified with slight under or overestimations. The largest landform mapped was a nearly 4 km^2 large assemblage which includes the *Empalme* rock glacier. This landfrom was mapped 4.3 km^2 by *CNN_noCurv*. When it comes to the transfer to the SPOT 7 imagery of northern Estero Derecho, *CNN_noCurv* mapped 20 out of 40 landform groups. 15 of them were those larger than 0.2 km^2. Overall, the accuracy of the classification drops when transferred to imagery from another sensor, however the largest and most significant rock glaciers were still sucessfully mapped. The scatterplot (Figure 27) shows that while smaller landforms were more likely to be missed, larger ones were generally detected on all three study areas.

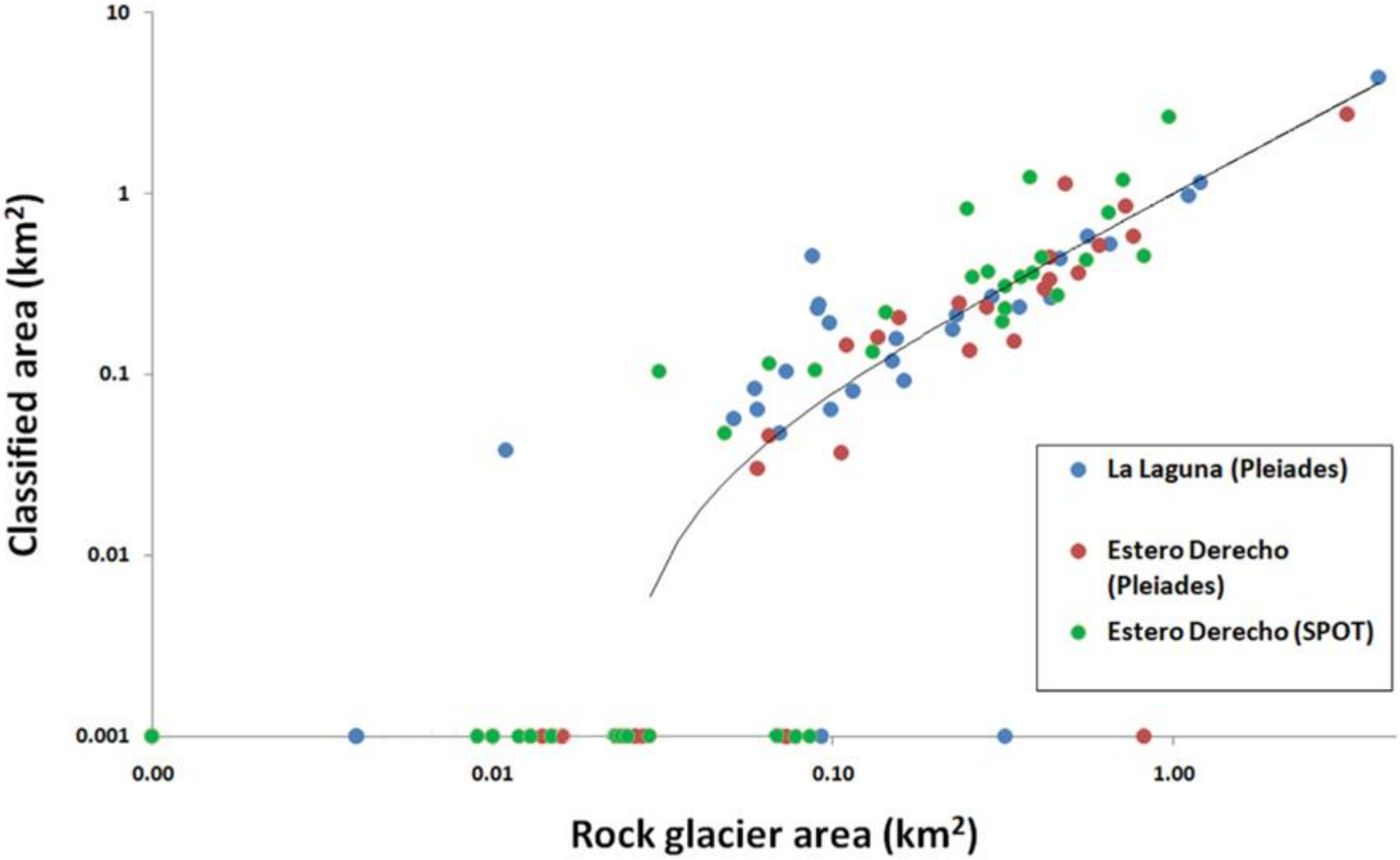

Figure 27: Scatterplot showing rock glaciers mapped by CNN_noCurv against the manually corrected outlines.

7.3.2.Results for CNN_wCurv

When planform and profile curvature layers were added to the investigation, the classification produced better results with every 32 rock glacier larger than 0.05 km^2 being mapped. Improvements were observed on the Pleiades image of Estero Derecho as well, where only 4 medium or large rock glaciers were left unmapped out of a total 25. This shows advancement for the Pleiades data, although the scatterplot shows frequent underestimations. On the other hand, when the method was transferred to SPOT 7 data, the classification failed to adequately distinguish rock glaciers from other non-targets producing very low accuracy values. In total, only 13 rock glaciers were mapped. Two of them were smaller than 0.05 km^2 and 11 were medium sized rock glaciers that were mapped out of a total 42. On the scatterplot (Figure 28), it is visible that while most rock glaciers on the Pleaides imagery was mapped, *CNN_wCurv* missed a large number of landforms when transferred to SPOT data.

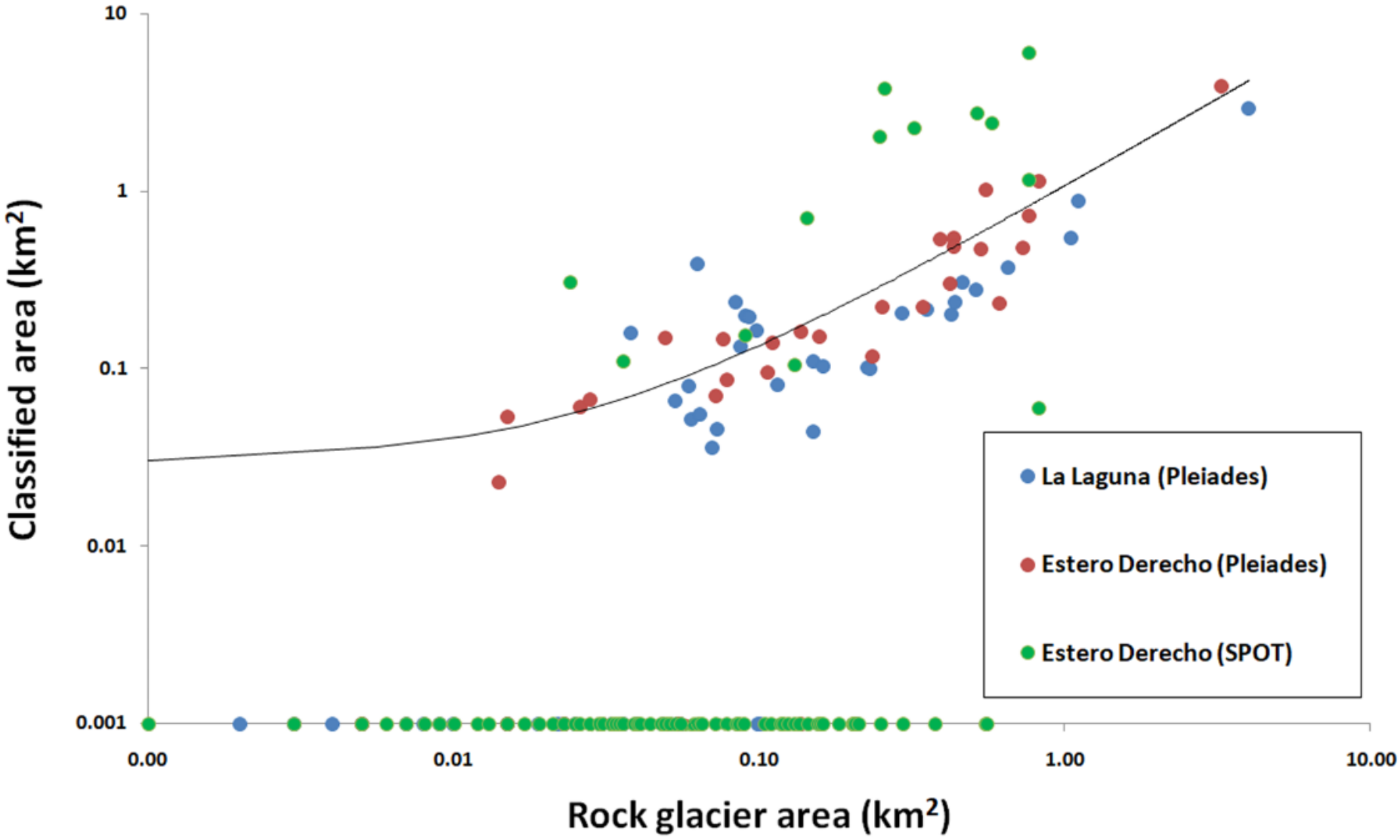

Figure 28: Scatterplot showing rock glaciers mapped by CNN_wCurv against the manually corrected outlines.

7.4. Comparison with velocity rates

The two classifications were compared to velocity information in order to find out if there is any correlation between mapping accuracy and surface velocity rates (Figure 29). Two complete velocity rasters were used, both of them generated by Benjamin Aubrey Robson at the Department of Geography of the University of Bergen. For the La Laguna catchment, the velocity information was extracted by feature tracking using 2012 GeoEye and a 2020 Pleiades images. Velocity rates of the Estero Derecho region were gained from InSAR on Sentinel-1 imagery from 2015 to 2019. Mean surface velocities were calculated and rock glaciers faster than 0.1 m a^{-1} were then compared to their accuracy (Figure 30). Both *CNN_noCurv* and *CNN_wCurv* showed weak correlation between mapping accuracy and surface velocity. The accuracy of rock glaciers between 0.1 and 0.5 vary greatly between 0% and 98.7%. Rock glaciers faster than 0.5 m a^{-1} were mapped with more confidence. When comparing the two classifications, the scatterplots show that the correlations are low in both cases: 0.364 for CNN_noCurv and 0.345 for CNN_wCurv. In addition, it is also visible that *CNN_wCurv* had generally higher accuracies for active rock glaciers.

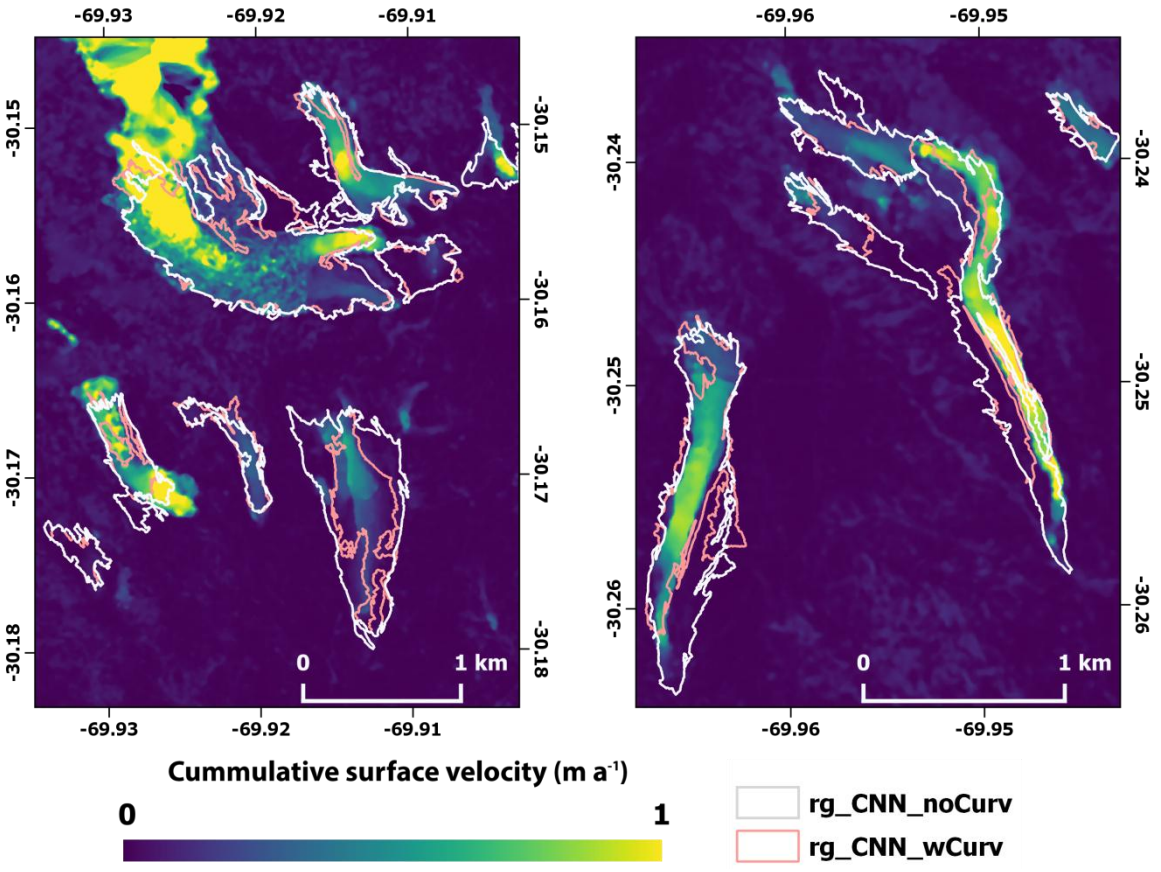

Figure 29: Classification outlines with surface velocity rates.

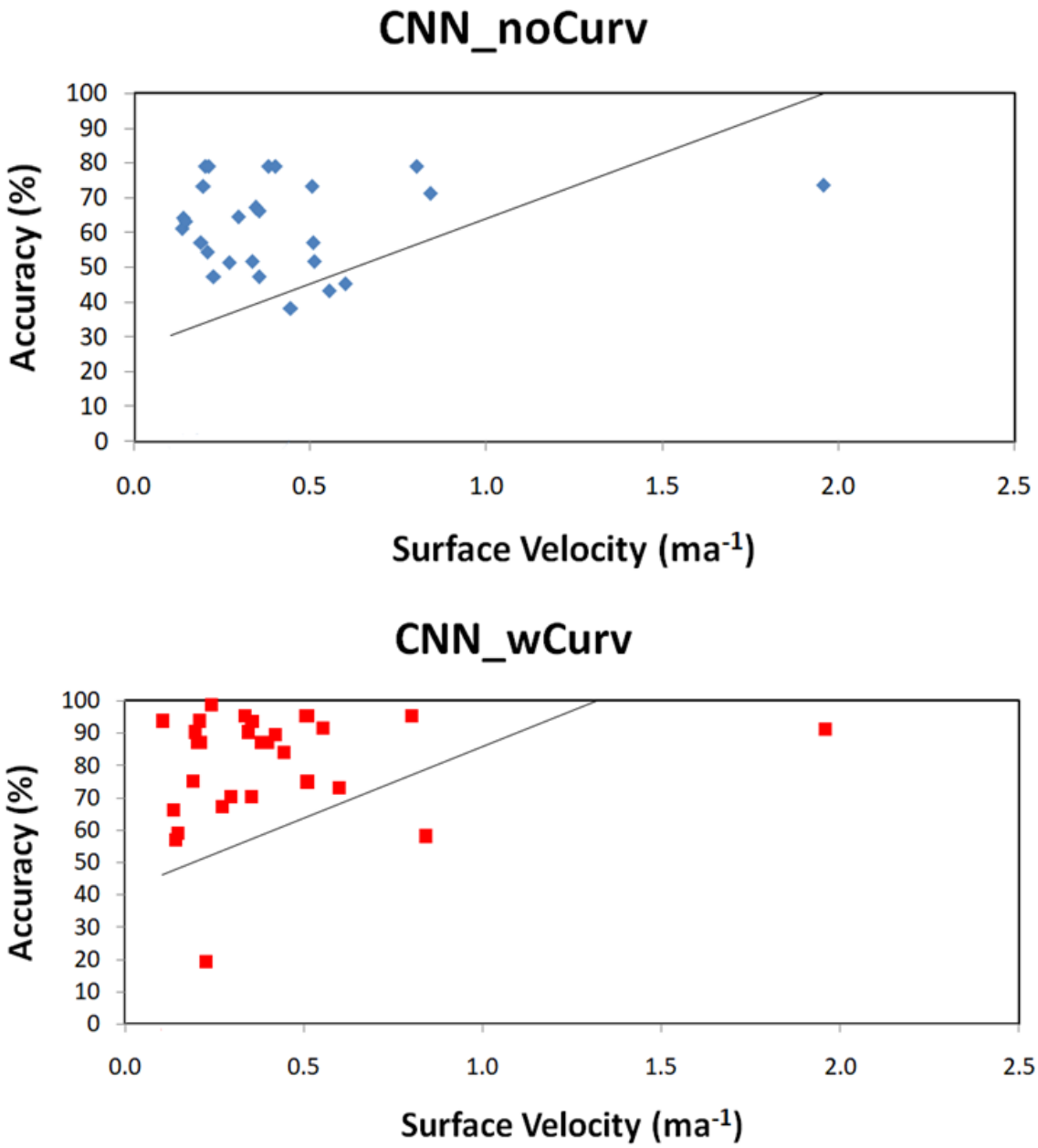

Figure 30: Scatterplots showing the relationship between rock glacier surface velocity and mapping accuracy of detected rock glaciers.

7.5. Comparison with other geomorphometric characteristics

In order to investigate connection between accuracy and other geomorphometric characteristics, the accuracies were compared with the slope, and mean roughness of rock glaciers. The comparison was performed the same way as with the velocity rates: geomorphometric information was extracted and then the mean values for each landforms/landform groups were compared to the mapping accuracy.

7.5.1. Slope

When looking at the slope values of the mapped landforms, it is visible that gentler rock glaciers were detected more successfully (Figure 31). The results also show that every rock glacier steeper than 30° was missed by the classifications not only on the SPOT data but also on the two Pleiades images. On the other hand, landforms gentler than 15° have been mapped with a mean accuracy of 56.8% by *CNN_noCurv* and 62.9% by *CNN_wCurv*. Again, the correlation between accuracy and mean slope proved to be weak: 0.127 for *CNN_noCurv* and only 0.111 in the case of *CNN_wCurv*. However, when the results of the transfer to SPOT data are excluded, the correlation for *CNN_wCurv* becomes 0.379. Therefore, it can be concluded that slope possibly had an influence in the classification of Pleiades imagery.

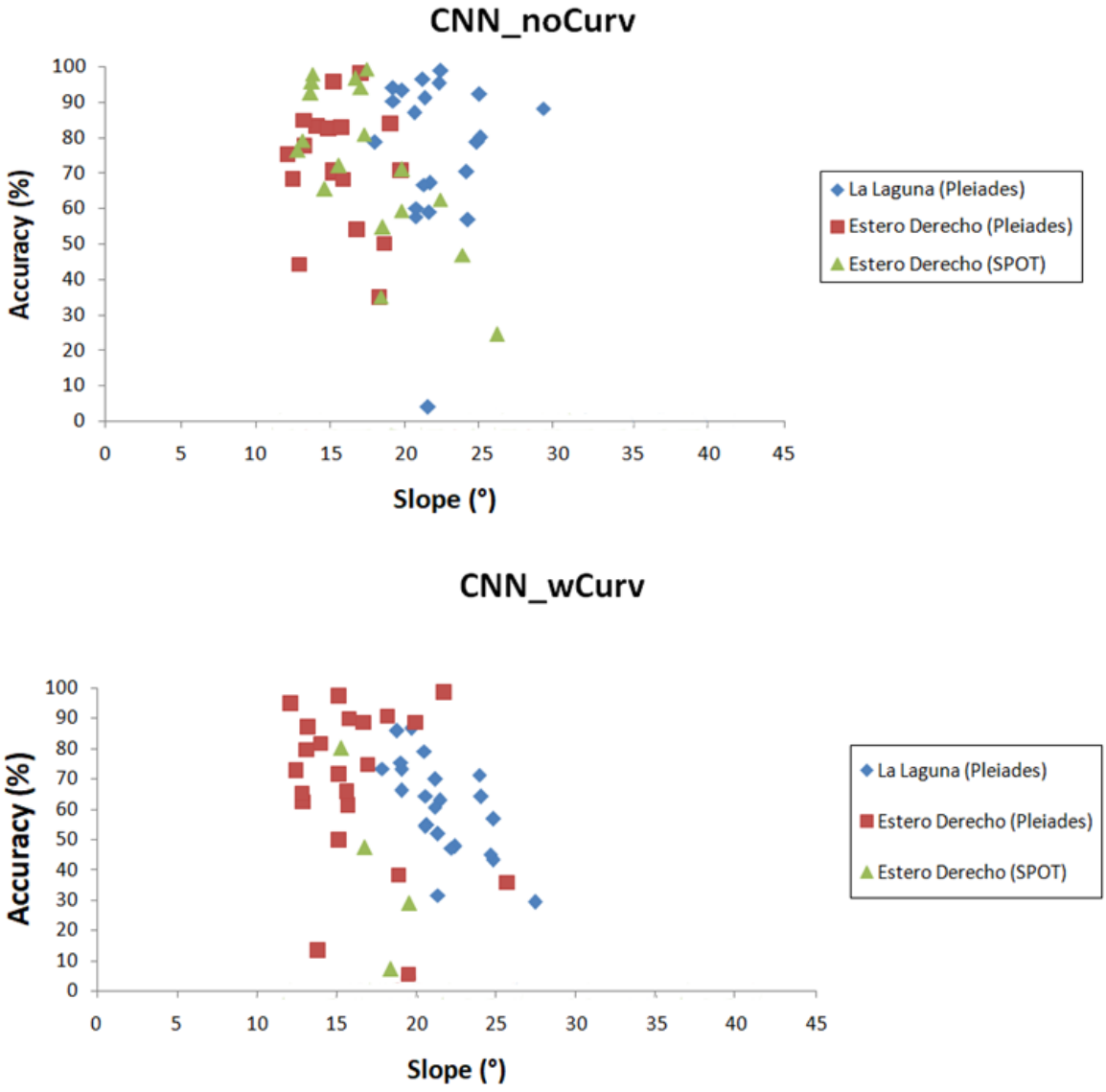

Figure 31: Relationship between classification accuracy and slope of detected rock glaciers.

7.5.2. Terrain roughness

The tool Geospatial Data Abstraction Library (GDAL) was used to extract information about the terrain irregularity. It is calculated by the largest inter-cell difference of a pixel and its surroundings. Then, the mean terrain roughness for each rock glacier was extracted. The scatter plots indicate a relationship between surface roughness and mapping accuracy (Figure 32). Of rock glaciers with a roughness value larger than 0.1, *CNN_noCurv* detected 12%. Given its weak performance on the SPOT data, this value for *CNN_wCurv* is only 4%. Landforms mapped with higher accuracies had generally lower roughness level. For example, *CNN_wCurv* successfully identified every landform with a roughness lower than 0.5 with an average accuracy of 72.1%. The correlation between terrain roughness and classification accuracy was 0.140 for *CNN_noCurv* and 0.288 for *CNN_wCurv*.

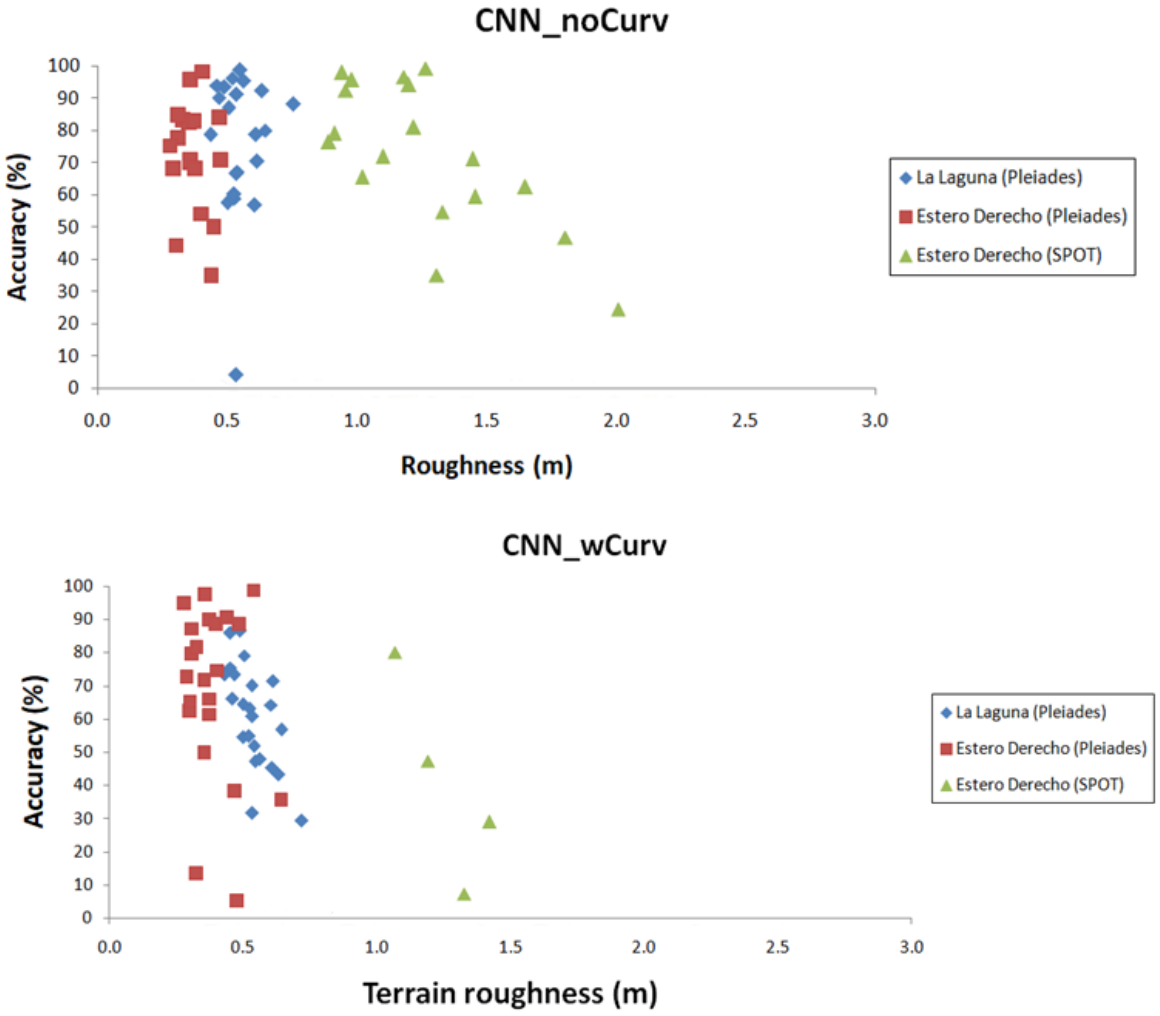

Figure 32: Relationship between classification accuracy and roughness of detected rock glaciers.

7.5.3. Aspect and compactness

Accuracies were also compared with aspect and roundness. The compactness of the reference outlines were computed by using the Polsby – Popper test. Originally studying gerrymandering, Polsby and Popper (1991) introduced a score that describes the compactness of a shape with using its area and perimeter:

$$PP = \frac{4\pi A}{P^2}$$

,where PP is the Polsby – Popper score, A is the area and P is the perimeter. This way, the compactness of a circle equals 1 while more irregular shapes have lower values (Polsby and Popper, 1991). However, the results did not show any relationship. Landforms of different aspect and compactness were mapped with a wide range of accuracy by both classifications. The scatterplots can be found in Appendices 1 – 2.

8. Discussion

The main objective of the thesis was to develop an automated method for rock glacier mapping using deep-learning and OBIA that can be equally applied to another study area and data from a different sensor. In this chapter, the results and effectiveness of the newly developed classification methods will be discussed with a particular focus on their transferability. A comparison with previous rock glacier mapping techniques and suggestions for future developments will also be given.

8.1. Transferability of the method

The sub-research questions of this thesis focus on how transferable the newly developed methods are. After training and testing the classifications *CNN_noCurv* and *CNN_wCruv* on Pleiades imagery of the La Laguna catchment, both were transferred to a different periglacial zone. The second test was conducted on a different study area, the southern part of Estero Derecho by still using Pleiades imagery. Lastly, the third classification was performed with both the study area and the sensor being different from what the CNN was trained on: a SPOT 7 tri-stereo was used that covered the northern part of Estero Derecho. The new inputs from SPOT 7 imagery had only a 1.5 m spatial resolution in contrast to the Pleiades that has 0.5 m. Overall, the presented method proved to be transferable between different areas and imagery although the accuracy dropped when curvature data was included. It was found that geomorphometric factors such as curvature, slope or surface roughness and differences in sensor specifications played an important role in the transfer and affected its successfulness.

The first *CNN_noCurv* method used only spectral bands, elevation and slope information. It performed well on the Pleiades images: The mean total accuracy was 65.85%. The user accuracy was significantly high, an average of 80.1% with over 80% in both areas. The producer accuracy was 72.8% on the La Laguna catchment and 64% for Estero Derecho, indicating a mean accuracy of 56.8%. When transferred to SPOT 7 data, the user accuracy dropped to 58.3% while the producer accuracy rose to 98.4% (Figure 37). It still managed to map a significant part mostly of the larger rock glaciers. During the second part of the rock glacier mapping, the method was repeated with planform and profile curvature layers included in the dataset (*CNN_wCurv*) to see how they would affect the classification. It was found that curvature helps rock glacier mapping when used on the same sensor data as the CNN was trained on. Apart from a marginally lower producer accuracy for Estero Derecho,

CNN_wCurv managed to outperform *CNN_noCurv* in every kind of accuracies. However, when transferred to SPOT 7 imagery, the accuracy of *CNN_wCurv* dropped drastically misclassifying different large areas as rock glaciers and by producing an enormous overestimation. On the other hand, several real rock glaciers were missed and therefore the classification has been considered unsuccessful.

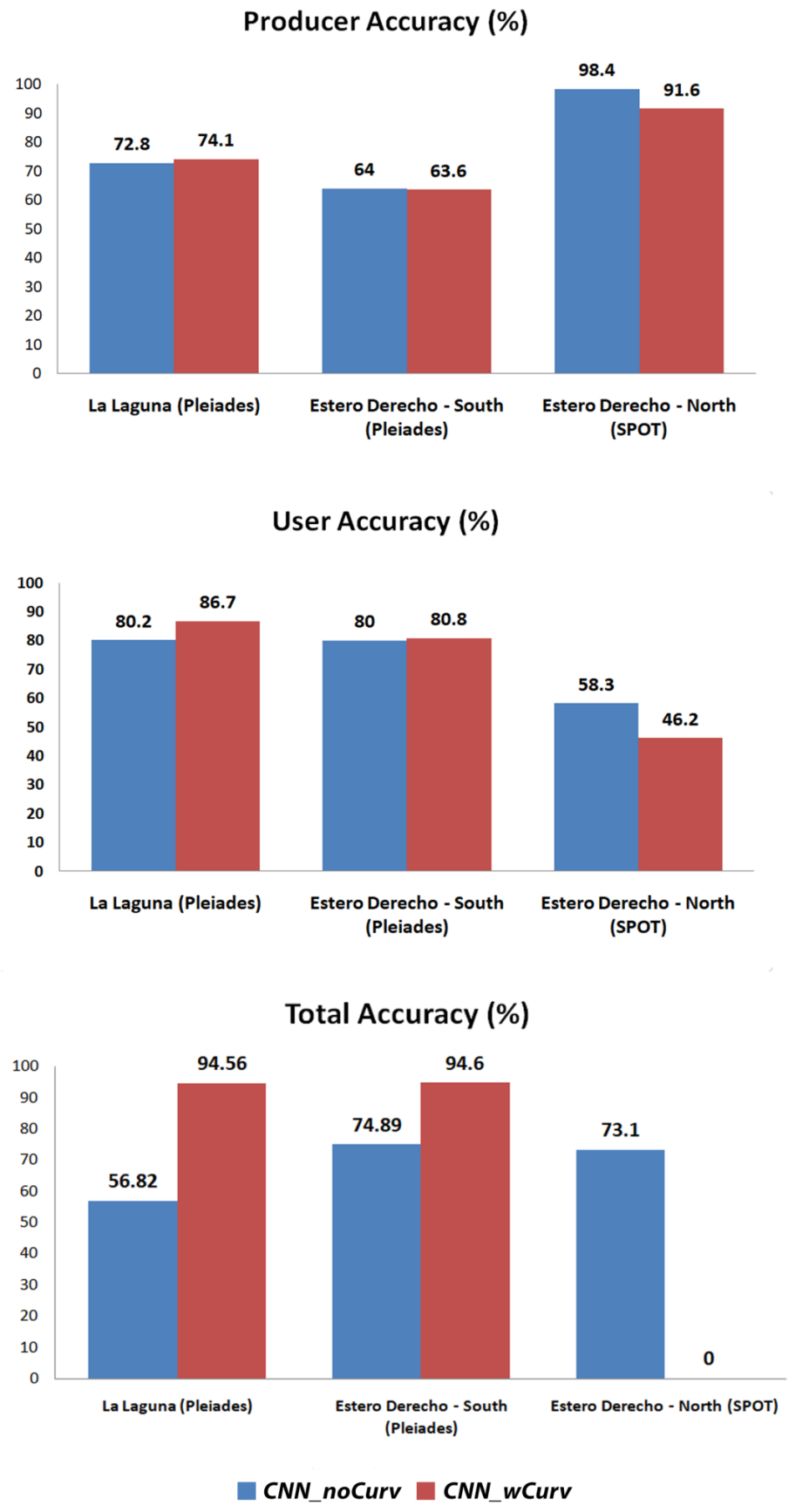

Figure 33: Changes of accruacy rates during the transfers of the classifcations.

8.1.1.Role of curvature data

This inconsistency may have different reasons. One can be the difference between spatial resolution of SPOT 7 and Pleiades and the characteristics of curvature. The layer the CNN was trained on had a 0.5 m resolution and therefore was a very detailed dataset. Curvature can vary in space greatly. This is especially true on rock glacier surfaces where ridges, furrows, slopes or even lakes can alternate and a high resolution curvature layer is able to show these small changes. When compared to Pleiades, SPOT 7 imagery has a much lower resolution and its curvature layers looks coarser when visualised (Figure 38). The CNN was trained on 30 x 30 pixels large sample patches which would be an area of 60 x 60 m for Pleiades but only 45x45 m in the case of SPOT 7. Another reason can be the complexity of the CNN model. As Wang et al. (2018) described, a too deep and overly parameterised CNN can cause overfitting. It is therefore possible that by using more layers, the CNN became too biased by the training data, failed to generalize and work adequately on data from a different sensor.

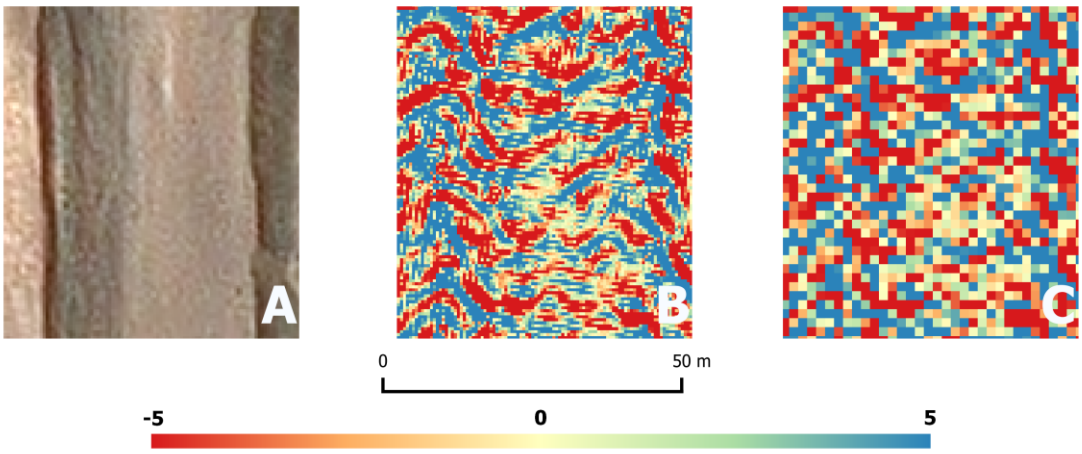

Figure 34: Curvature layers extracted from a furrow on the Las Tolas rock glacier (A) with 0.5 (B) and 1.5 (C) metres spatial resolution).

As a conclusion, adding curvature layers did improve the classification, but only when applied on data from the same sensor that the CNN was trained with. Working only with elevation and slope layers had lower accuracies on the Pleiades imagery but the method was well transferable to SPOT 7 imagery and did manage to map the larger, more significant rock glaciers.

8.1.2.Difference of terrain roughness

Closely related to surface curvature, terrain roughness also show significant differences between Pleiades and SPOT data. The comparison of accuracy and terrain roughness presented in chapter 7 showed that rock glaciers on the SPOT image had a significantly higher roughness value. During an investigation of their role, the roughness layers of Pleaides were first resampled to make sure the devation is not caused by the spatial resolution difference. While the rock glaciers of the two Pleiades images had an average value of 0.556 m, the mean roughness of the landforms on the SPOT data was 1.531 m (Figure 39). In addition, it was found that the average size of rock glacier on the SPOT image was half of those on the Pleiades data. As pointed out in the previous chapter, these factors have likely played a role in the classification and the different values on the SPOT probably caused further complications in the transfer.

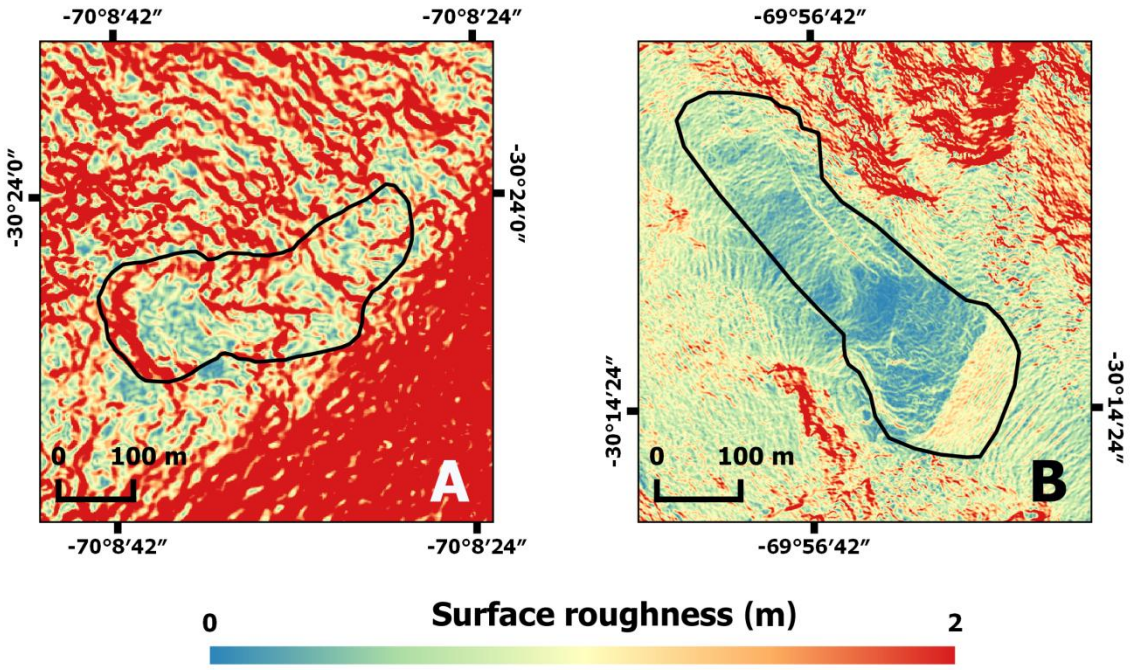

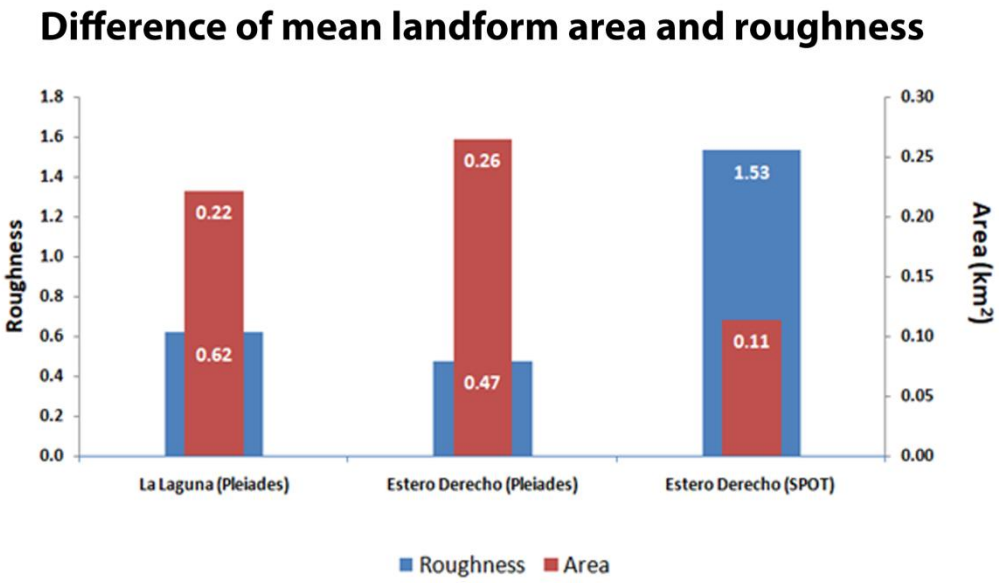

Figure 35: Differences of surface roughness during the transfer between Pleiades and SPOT 7 imagery. When visualized, it is visible that roughness values are generally higher ont the SPOT imagery (A) than on the Pleiades data (B).

8.1.3. Difference in sensor specifications

Although its influence is likely marginal, it should be noted that the multispectral bands of Pleiades and SPOT lie on different wavelength regions (Table 6). Therefore, a point with a given reflectance might have different pixel values on a Pleiades and on a SPOT image. This slight difference in spectral signatures further aggravates the transfer between different sensors.

Table 6: Sensor specifications of Pleiades and SPOT satellites (earth.esa.int).

Spectral bands	Pleiades	SPOT
Panchromatic	470 – 830 nm	450 – 750 nm
BLUE	450 – 530 nm	450 – 520 nm
GREEN	520 – 590 nm	530 – 600 nm
RED	620 – 700 nm	625 – 690 nm
Near-Infrared	775 – 915 nm	760 – 890 nm

8.2. Detection of new rock glaciers

In addition of the transferability, a major advantage of the method was found during visual inspection of the allegedly false positives in the results. After checking the satellite imagery, it was found that many of these polygons were in fact small individual rock glaciers that were not included in the inventory used for training and validation purposes. These landforms were generally 0.1 – 0.2 km^2 in size and had characteristics similar of rock glaciers. Some landforms were found to have a distinct lobate shape with flow-like morphometry, steep frontal slopes with ridges and furrows on the surface or gentler, rounder slopes and lighter shades (Figure 36 – 37). In total, seven landforms that are possibly rock glaciers were found by the CNN over all three study zones. The velocity rates did not show any motion in these areas, which assumes that these landforms are inactive. Creating a complete and up-to-date rock glacier inventory for the semiarid Andes can be challenging (Schaffer et al., 2019), especially for the region of Estero Derecho which is less well studied than other areas (de Pasquale et al., 2020, Valois et al., 2020). It is therefore possible that the CNN classification managed to map inactive rock glaciers that were missed by the manual delineation and were not included in the reference inventory. In this case, it was shown that the automatic method is capable of outclassing even manual correction which indicates a major improvement.

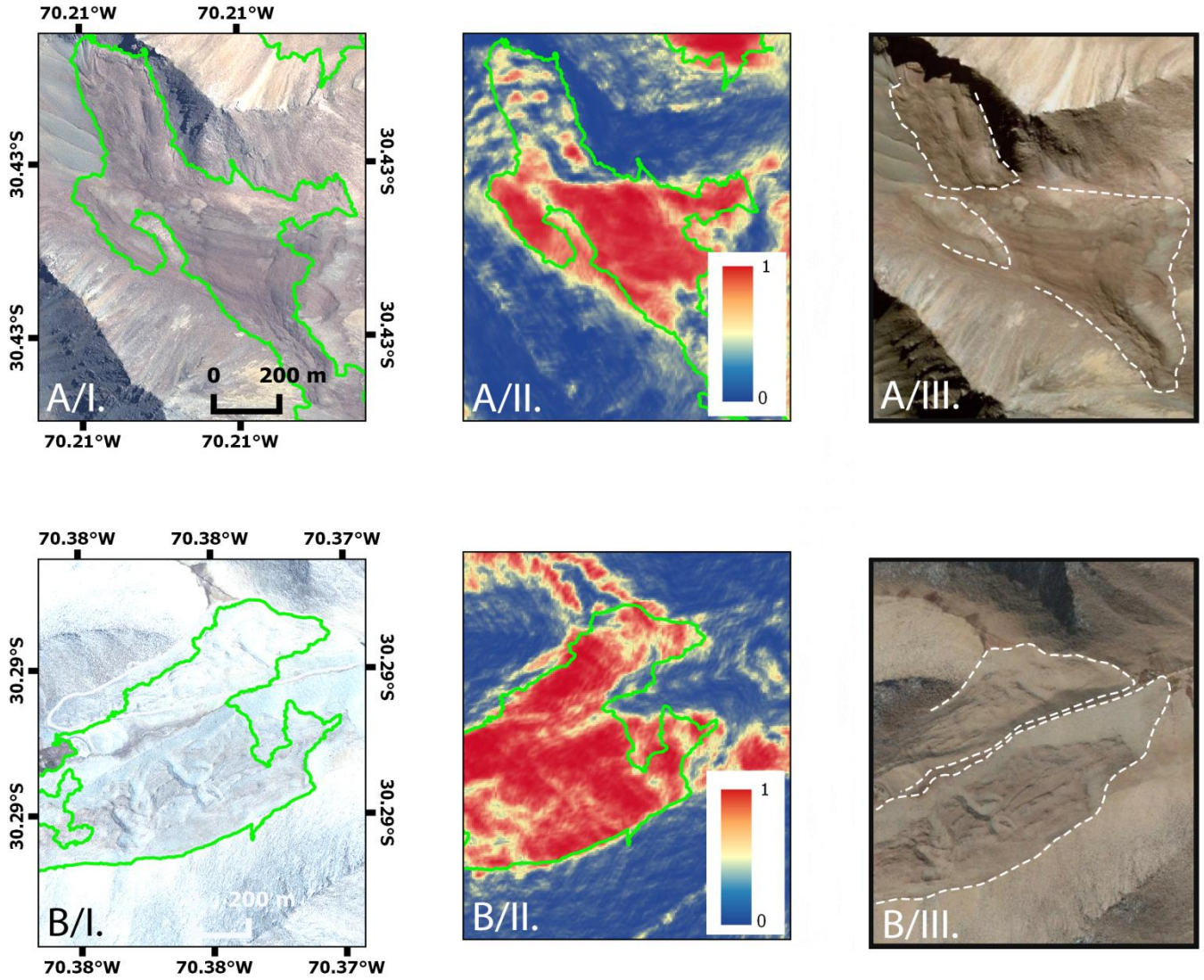

9.

Figure 36: Examples of rock glaciers detected by the CNN but not included in the manual reference depicted on the 2020 SPOT orthomosaic (I.), the CNN heatmap (II.) and on Google Earth Pro(© 2021 Maxar Technologies) with their distinct front highlighted manually.

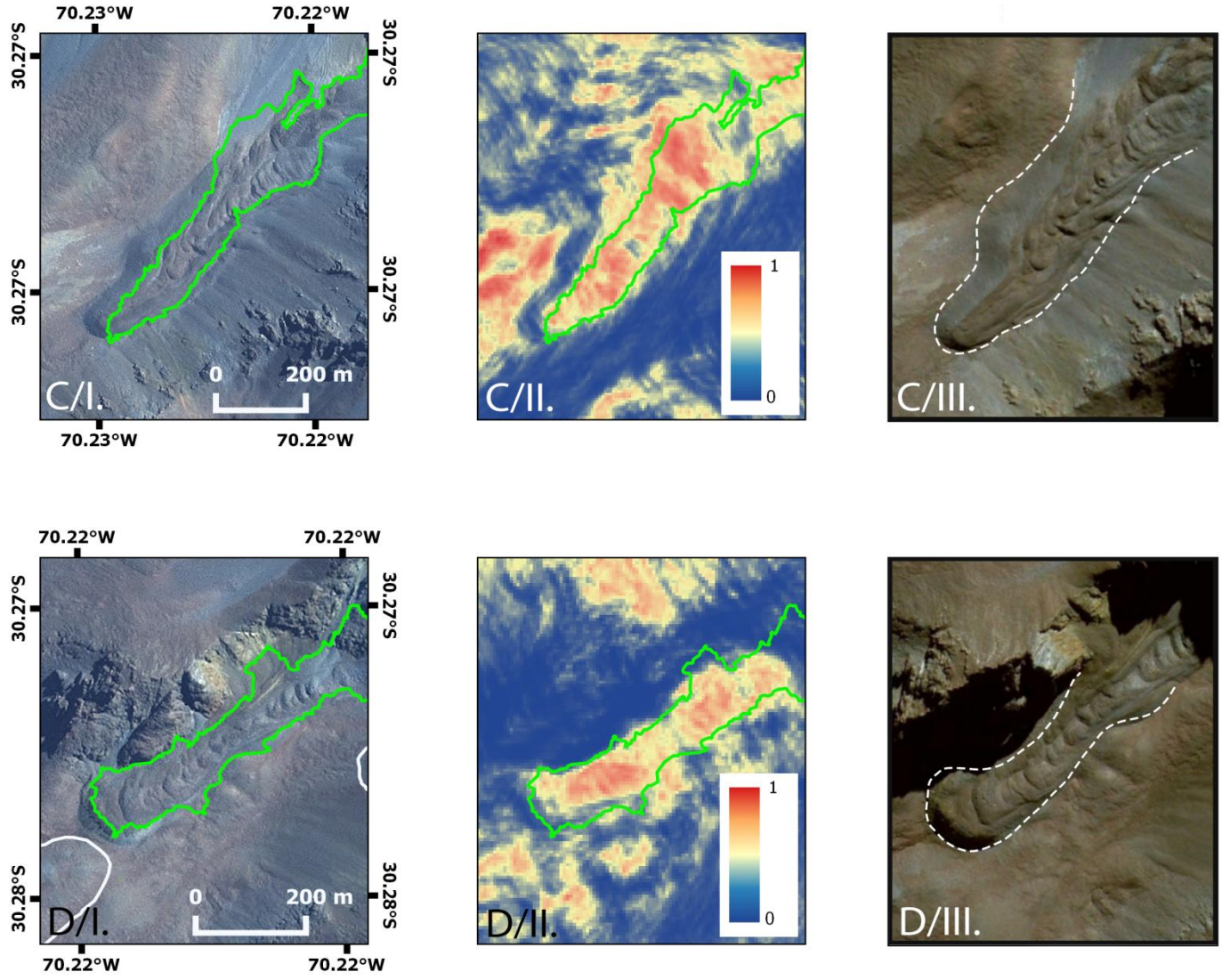

10.

Figure 37: Examples of rock glaciers detected by the CNN but not included in the manual reference depicted on the 2020 SPOT orthomosaic (I.), the CNN heatmap (II.) and on Google Earth Pro (© 2021 Maxar Technologies) with their distinct front highlighted manually.

8.3. Inaccuracies in the classification

Despite their promising results, the classifications still contain errors in the form of false positives or false negatives. After all tests and accuracy assessments were done, the results were inspected together with the satellite imagery to find potential reasons of the inaccuracies. With the exclusion of *CNN_wCurv*'s performance on the SPOT 7 imagery, the results of the accuracy assessments show the classifications' user accuracy were high, while the producer's accuracy remained generally lower. This indicates that while most of the area what the method identified as rock glacier was mapped correctly, there were a lot of rock glacier areas that were not detected. The number of false positives was mainly smaller than the one of false negatives. Apart from the polygons that were found to be rock glaciers not included in the reference inventory, false positives occurred when the CNN misclassified talus slopes, fluvial deposits or other rock glacier-like features with ridges, furrows (Figure 38). In certain cases, the false positives consisted of the bedrock surrounding actual rock glaciers. As stated in the literature on rock glacier mapping, the misclassifications of these areas is a common phenomenon and the differentiation between rock glaciers and their surroundings pose as one the main challenges of rock glacier detection.

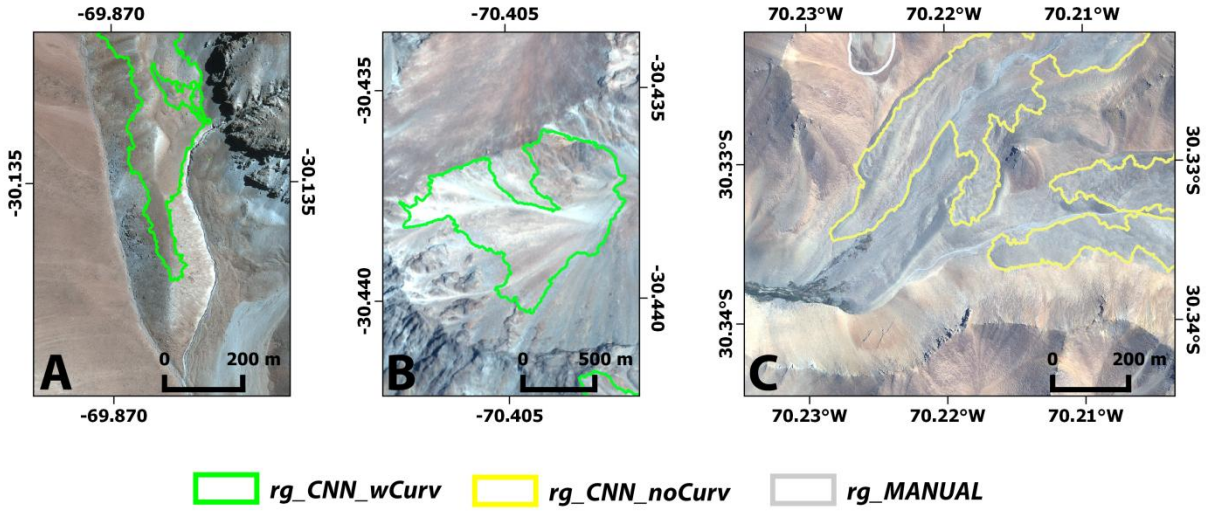

Figure 38: Lobate shaped feature (A), talus slopes (B) and fluvial deposits (C) wrongly classified as rock glaciers. Background images are the 2020 SPOT and Pleiades orthmosaics.

The classifications have also underestimated or missed certain landforms. The main reason of undetected rock glaciers is the settings of the OBIA refinement. As mentioned in Chapter 6, an area threshold was partially applied after the last multiresolution segmentation, with a large number of landforms smaller than 0.1 km^2 being removed. This allowed to clean the dataset

from a large number of false positives but also removed a significant proportion of smaller rock glacier outlines as well. Overall, the reference dataset contained 86 landforms smaller than 0.1 km^2 representing 34.12% of the whole inventory. The scatter plots showing the relationship between mapping accuracy and landform area (Figure 27 – 28) show that both classifications detected less than 20% of all landforms of those smaller than 0.1 km^2 (13.08% for *CNN_noCurv* and 18.46 % for *CNN_wCurv*) and the OBIA cleaning of these small outlines is likely to have a major role in these low accuracies.

8.3.1. Missing frontal slopes

Trends in underestimation of larger rock glacier were spotted as well. Generally, the CNN classifications had a tendency not to include the steep frontal slopes of the landforms. The visualisation of the outlines together with the satellite imagery showed that both *CNN_noCurv* and *CNN_wCurv* had a tendency to map only ridges and furrows on the upper plateau of rock glaciers but not the steep slope at their front (Figure 39). On the contrary, the manually corrected outlines included these slopes which often represented a very large proportion of the entire polygon area (Figure 31). Since this dataset was used as ground truth in the accuracy assessment, the results showed significant underestimations. Different factors could have led to this phenomenon. The most likely reason is the spectral and morphological difference between the undetected parts and the rest of the rock glacier body. The missed slopes were usually very long and much steeper. In the La Laguna catchment for example, in the case of the better performing *CNN_wCurv*, the average steepness of the detected rock glacier areas was 18.6° while the mean slope of the missed parts was 27.2° indicating that the method tended to miss the steepest parts (i. e. frontal slopes). Further, differences of colour on the multispectral imagery can be observed as well. These characteristics make these large frontal slopes more similar to ordinary talus slopes or hill sides and could have created confusion in the CNN. It is also probable that while the majority of the training patches were collected from the rock glacier plateaus, only a small number of samples was generated on the frontal slopes and the training data was insufficient to recognise these areas as rock glaciers.

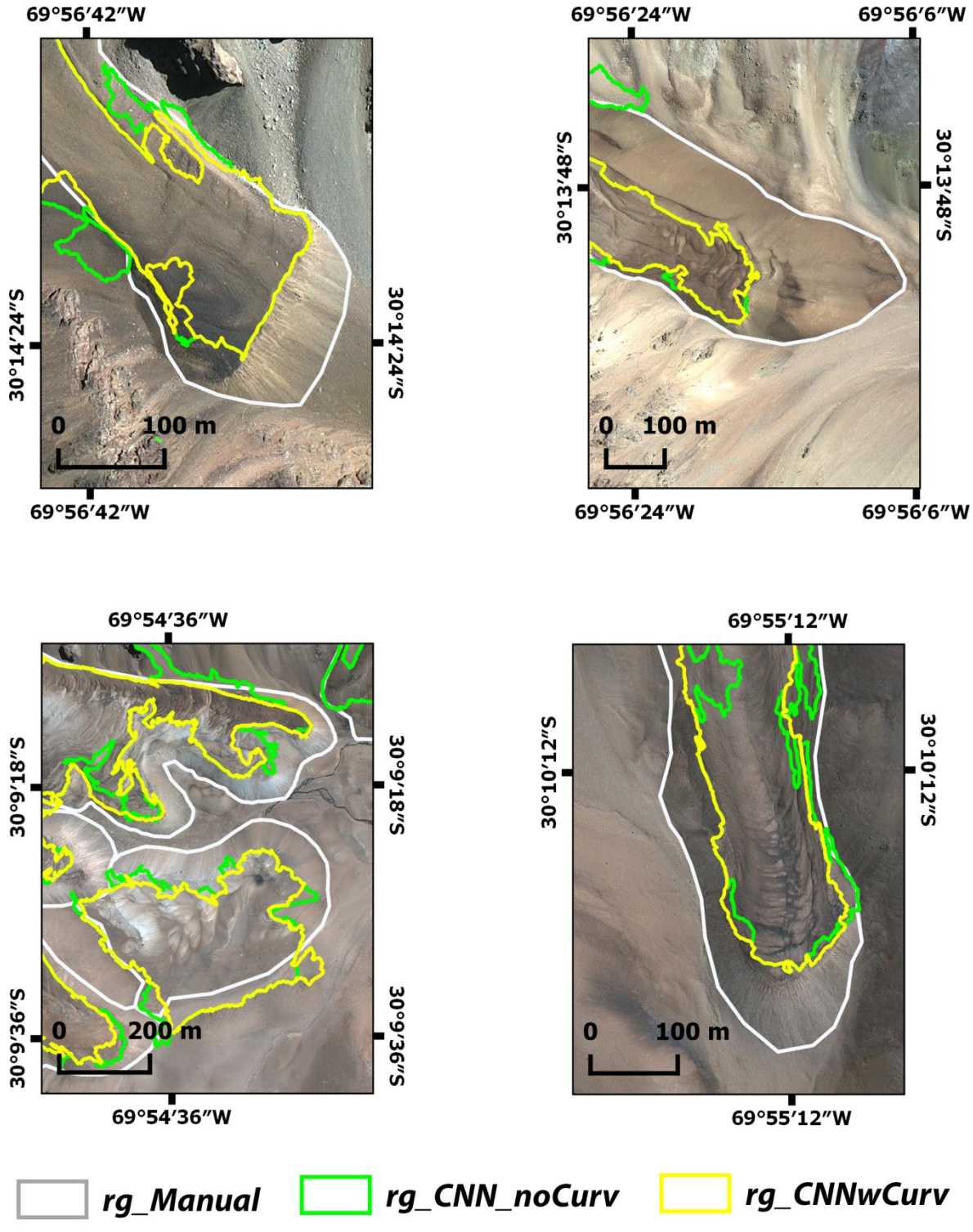

Figure 39: Comparison of manually corrected and the automatically generated outlines. The figure shows that the morphometric and spectral difference led the classifications not to include the frontal slopes in the outlines.

8.4. Effects of data artefacts

In addition to the problems listed above, the errors and artefacts of the input data should also be mentioned. Errors while performing satellite photogrammetry can occur when the software failed to match image points and the correlation remains zero in an area. This could lead to false values in the DEM that will influence the extraction of other geomorphometric information (Figure 40).

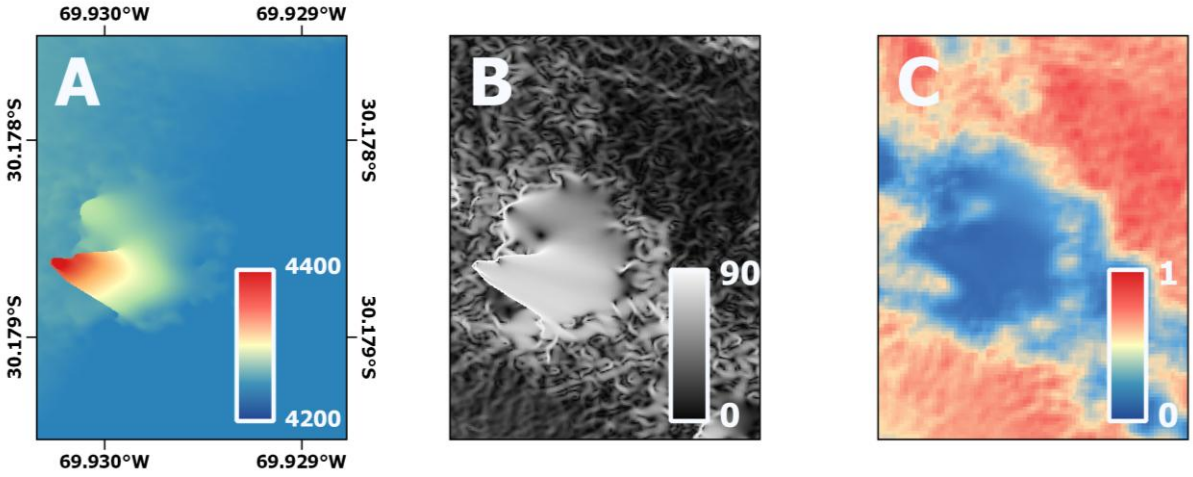

Figure 40: Error from image matching affecting the DEM (A), the slope layer (B) and the final CNN heatmap (C).

Oversaturated pixels on a certain spectral bands can also occur. Single event upsets are caused by energetic particles that produces electrical signal in the sensor and are extremely common in the South Atlantic Anomaly. These artefacts manifest as small, discoloured patches on true colour images since it usually affects only one spectral band and is able to lead to false values in the final heatmap (Figure 41). Despite the relatively low occurrence of these errors, poor data quality is able to affect the effectiveness of the classification. Therefore in more serious cases, manual correction needs to be considered.

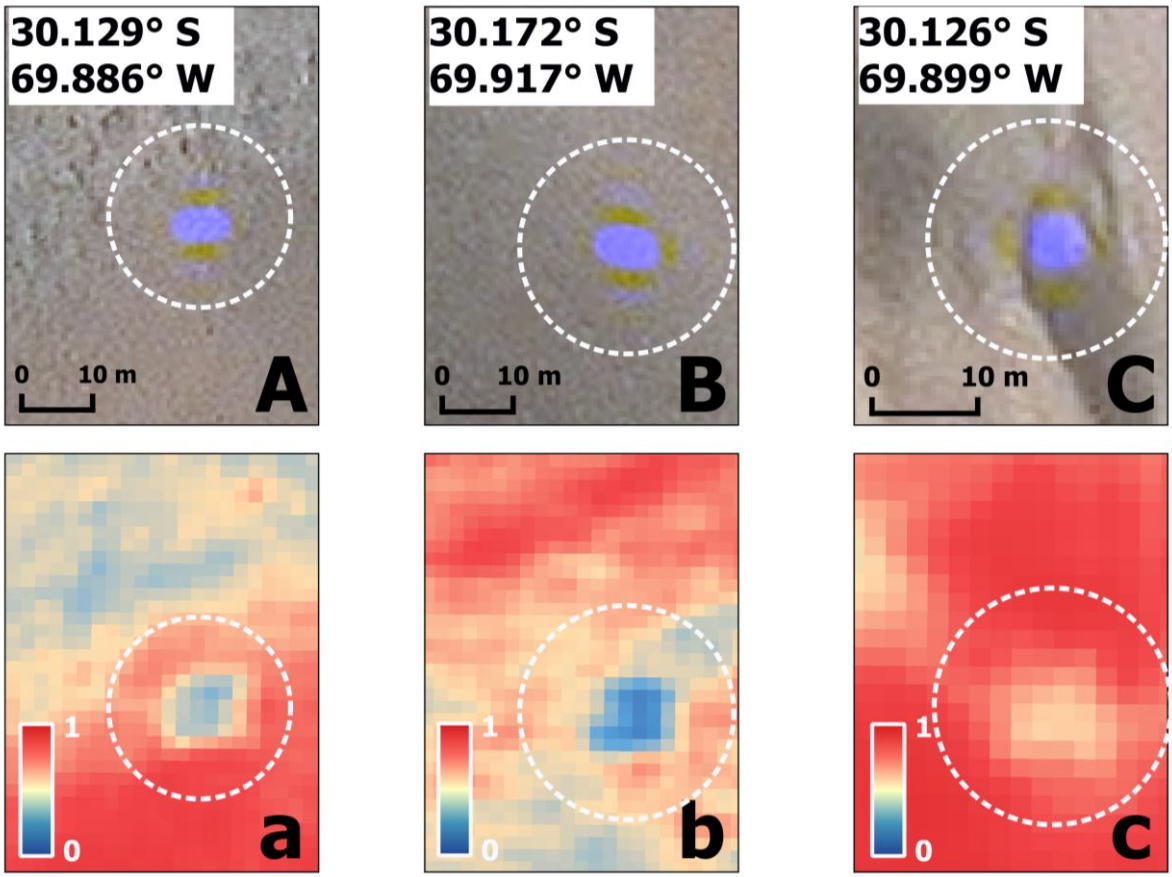

Figure 41: Examples of single event upsets on the blue band of the 2020 Pleiades orthomosaic (A-C) that influenced the final CNN heatmap.

8.5. Comparison with other rock glacier mapping methods

In order to get a better overview of the advantages of the method presented, this section will give a comparison with other methods that have been applied for rock glacier mapping.

8.5.1. Comparison with manual methods

Rock glacier inventories are generally made manually. It is however difficult to compare automated methods to the manual techniques as in the absence of reference data, studies using manual delineation do not provide accuracy assessments (Robson et al., 2020). However, the investigation of allegedly false positives showed that CNN and OBIA-based automatic classification can be a useful addition for rock glacier mapping not only because it is able to reduce the time span but also for its possible ability to detect rock glaciers that human eyes might miss. Many manually created rock glacier inventories (Liu et al., 2013, Villarroel et al.,

2018a) are based on surface velocity derived from InSAR data. This CNN classification did not use velocity layer as input, although the results were compared to velocity rates to find correlation. The comparison showed that the method is suitable to map both active and inactive rock glaciers. Therefore, it has an advantage over InSAR-based methods that are unable to detect inactive and relict rock glaciers that can still be important due to their freshwater storage. Further, velocity measurement from InSAR or feature tracking is dependent on perpendicular and temporal baselines and is therefore more difficult to calculate over smaller areas, while methods using CNN and OBIA do not have this limitation (Robson et al., 2020).

The use of Google Earth imagery or other freely available satellite products (e.g. Sentinel-2, Landsat) is common for rock glacier mapping (Jones et al., 2018c, Pandey, 2019, Rangecroft et al., 2014). In this thesis however, data for commercial satellites was used. These images have much higher spatial resolution than free satellite images which is likely to improve automatic classification. Furthermore, these products allow data extraction such as DEM generation and automated classifications, unlike imagery from Google Earth. Finally, it is now possible to order SPOT 7 and Pleiades imagery through ESA for scientific research for free, although the size of AOI is limited.

8.5.2. Comparison with other automatic methods

The methods applied in this thesis were based on the work Robson et al. (2020) whose method was formed on Brenning et al.'s (2012) paper on using textural filters to identify rock glaciers. Comparison of the results with previous studies showed that the newly developed methods are able to outperform earlier automatic classifications (Table 7). The *CNN_OBIA* method of Robson et al. (2020) was performed on Sentinel-2 images of 10 m resolution and Pleiades images resampled to 2 m resolution. In contrast, the method presented in this thesis used Pleiades tri-stereos (0.5 m) and SPOT tri-stereo data (1.5 m spatial resolution). The classification on Pleiades data proved to be more accurate with a total accuracy of 76.8%, a user accuracy of 72.0% and a producer accuracy of 88.4%. Further, the presented method could map a larger number of landforms in the La Laguna catchment (51 against 27) with the smallest identified rock glacier being only 0.011 km^2. During the comparison, both *CNN_noCurv* and *CNN_wCurv* could outperform *CNN_OBIA* in total accuracy and user accuracy.

Table 7: Comparison of the new results to Robson et al.'s (2020) results.

Classification	Accuracy	User Accuracy	Producer Accuracy
Robson et al.'s CNN_OBIA (Sentinel-2)	72.0%	65.9%	71.4%
Robson et al.'s CNN_OBIA (Pleiades)	76.8%	72.0%	88.4%
CNN_noCurv (SPOT)	73.25%	58.3%	**98.4%**
CNN_noCurv (Pleiades)	65,85%	80.1%	68.4%
CNN_wCurv (Pleiades)	**94.58%**	**83.75%**	68.85%

Visual inspection also showed that similarly to *CNN_noCurv* and *CNN_wCurv*, the *CNN_OBIA* of Robson et al. (2020) also tended to exclude frontal slopes. On the other hand the two new classifications managed to map active rock glaciers that were missed by *CNN_OBIA* (Figure 42).

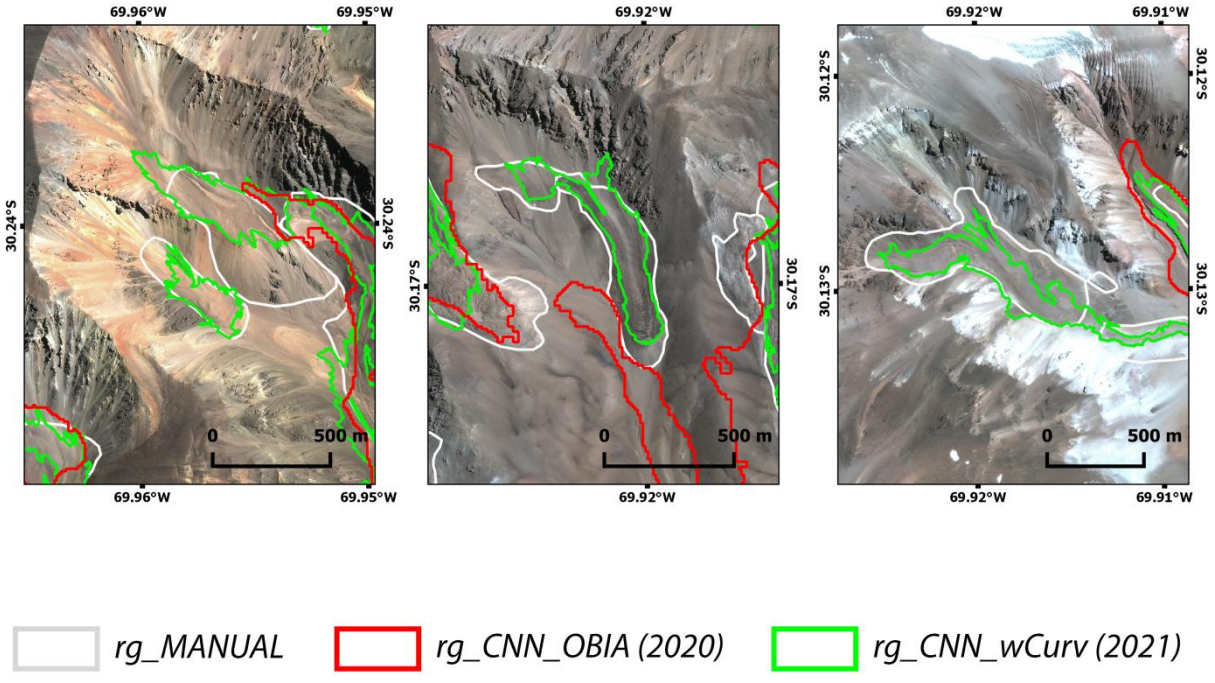

Figure 42: Examples of rock glaciers missed by Robson et al. (2020) but detected by the new classification. Background image is Pleiades orthomosaic from 2020.

When it comes to other automated rock glacier mapping methods, the new classification presented is comparable with both the method of Brenning et al. (2012), which obtained

accuracies between 0.7 and 0.8 with textural filters and Marcer's CNN, that identified 60-70% of total rock glaciers.

8.6. Overall limitations

The inaccuracies and their causes already mentioned above in the chapter indicate that the method presented is not without limitations. Small rock glaciers are likely to be excluded during the OBIA refinement and underestimations or overestimations can still occur with the larger landforms. In addition, the CNN relies on the training patches which can be insufficient to effectively classify rock glaciers. Therefore, an extensive, reliable and accurate inventory is needed as training data. Since the patterns and textures of rock glaciers can be near-identical to the surrounding bedrock or similar landforms like debris flows, talus slopes, or other deposits, the classification can produce false positives, especially when transferred to different imagery or study area, as the case of *CNN_wCurv* showed. Lastly, neural networks have a limitation to be very complicated and difficult to properly parameterise. The model used in this thesis collected patches of 30x30 pixels. The training was performed with a learning rate of 0.015 that were convolved three times and max-pooled twice. These settings were used after using trial and error methods and it is especially difficult to tell which parameters need to be refined to achieve better results.

The method might have other limitations in case further attempts of transfer. Although the model which was trained on Pleiades data could work on SPOT 7 imagery, there is a possibility that the results would differ when the method is transferred to other satellite data, such as Landsat or Sentinel-2 due to their lower resolution. With its 4-level segmentation and different rule-based classifications, the OBIA refinement is very complex which may increase the risk of inaccurate classification when transferred on other imagery. Despite these challenges, the method presented can be helpful in rock glacier inventory creation as a helpful additional tool and many possibilities of further improvement.

8.7. Potential future developments

So far, the use of deep-learning together with OBIA for rock glacier mapping has been covered only by Robson et al. (2020). However, the results presented in this thesis shows that this method could be a powerful tool and further research is needed for future development.

8.7.1. Changes of the workflow

The results presented contained false positives and negatives with under and overestimations. The classifications were based on the heatmap generated by the CNN and further studies are required to develop a CNN architecture that produces a more accurate heatmap. This will also allow the application of a less complex OBIA ruleset for refinement. Further calibrations might also lead to a better transferability between different images.

The current method requires Trimble eCognition that has an embedded CNN tool. However, it is possible to perform deep-learning classification using custom scripts. The most popular deep-learning libraries are Keras and Tensorflow. By migrating the method to one of these open-source tools, it will be possible to use deep-learning image classification without obtaining eCognition licenses. Another potential transformation of the method is the application of cloud-computing. Cloud Computing is an internet-based architecture which creates a computing environment to provide availability, scalability and flexibility of computer infrastructures at different level of abstraction (Haris and Khan, 2018). If a cloud-based service for CNN classification was established in the future, researchers from around the world would be allowed to upload data, perform their analyses and share their results without meeting strict software requirements or owning a powerful machine.

8.7.2. Input data

New datasets can be included to reach a higher accuracy: the curvature tool of QGIS allows creating more layers such as normal-contour, flowline or cross-sectional curvatures which may help in rock glacier detection. For example, the normal curvature, which measures the curvature along a horizontal plane, would help the identification of lobate-shaped landforms. Flowline information could be able to identify the flow-like morphology of active rock glaciers. The usefulness of different curvature layers has been proven by Ehsani and Malekian (2021) who used six different types of curvature derived from SRTM DEM to automatically map ridges and valleys. Using the same data with a higher resolution might be suitable for rock glaciers as well. Although they have been used for accuracy comparison, roughness layers may be a useful addition to the input datasets. Riley et al. (1999) presented a Terrain Ruggedness Index (TRI) to quantify heterogeneity. The Vector Ruggedness Measure (VRM) which was first introduced by Hobson (1972) allows the measurement of terrain ruggedness as the variation in three-dimensional orientation of grid cells within a neighbourhood. TRI

and VRM give useful information about the surface roughness and can be calculated within an implemented tool in ArcGIS or a custom Python script.

For this thesis, very-high resolution satellite imagery and DEMs were used as input layers. However, these datasets can be often unavailable or too costly. Previous studies have shown that effective CNN models can be trained with more low resolution but freely available satellite data to map different features (de Bem et al., 2020, Krysiak et al., 2020, Robson et al., 2020). Therefore, a comparative study could be conducted in the future by performing a classification in the same area using only high-resolution commercial satellite data and later only freely available imagery. This way, it is possible to find out how essential spatial resolution is to automatically detect rock glaciers. Lastly, an experimental investigation can also be lead with training data of mixed origins and resolution to find out if it is possible to make transferability between different satellite data better.

8.7.3. Testing on other areas

The two study areas in this thesis are located in the semiarid Andes which has unique geographical characteristics. Due to the climate, the area consists of mostly dry and vegetation-free bedrock. This gives remote sensing data acquired of this area special attributes. However, rock glaciers can be found in different mountainous areas around the world with different features. A popular area for rock glacier studies is the Himalayas (Jones et al., 2018a, Jones et al., 2018c). Having most of the highest peaks in the world, this region has a more extreme topography (Jones et al., 2018c) and significantly mores glaciers and debris-covered glaciers than the semiarid Andes. Several thousands of rock glaciers are located in the European mountain ranges and in North America (Jones et al., 2018a). These regions are characterised with more precipitation and denser vegetation than the study areas of this thesis. The presented method is assumed to be effective in these areas as the difference between rock glacier surface and its vegetation-covered surroundings is clearer. Another example is the rock glaciers of Greenland and Svalbard with unique arctic environment. The freely available Arctic DEM can be of great use to extract geomorphometric characteristics of these features. On the other hand, these areas are more difficult to monitor with optical satellite sensors due to their high latitude and prolonged polar nights (Myers-Smith et al., 2020). In conclusion, different factors need to be taken into consideration for the creation rock glacier inventories in different environments. As a result, it is recommended to test the presented method on rock glaciers from other different periglacial regions and to further

develop it in order to create an automatic rock glacier mapping technique that is equally effective in any parts of the world.

8.7.4. Classification of other landforms

A CNN suitable for rock glacier detection may be eligible to classify other landforms. Spectral and geomorphometric information have been successfully used to map landforms such as debris-flows (Chen et al., 2020), slope failures (Ghorbanzadeh et al., 2019), thermokarst (Huang et al., 2018) or fluvial landforms (Carbonneau et al., 2020). The ultimate goal would be to train the CNN to detect as many landform types as possible is order to create fully classified geomorphological maps of periglacial scenes.

Apart from landform inventory creation, deep-learning has proven to be suitable for mapping areas with landslides. Recent studies have shown that neural networks are suitable for the detection of high-risk areas (Wang et al., 2019, Prakash et al., 2021). A potential future development could be applied to train the CNN with similar geomorphometric characteristics and surface velocities to detect signs of unstable ground. In this way, the method will be useful not only for geological studies but also for risk assessment related to geo-hazards.

8.3.1. Differentiation between active and inactive landforms

Although both active and inactive rock glaciers can contain enough ice to act as a freshwater storage, faster deforming landforms are known to contain more amount of ice and therefore have a higher hydrological significance. As a future development, velocity information can be added to the input of the CNN and different classes can be used for active and inactive rock glaciers. Velocity rates extracted with InSAR or feature tracking can be combined together with other geomorphometric information related to landform kinematics and used as training data. A method that is able to classify active and inactive rock glaciers separately will be useful to set up an inventory based on ice content for freshwater management and strategic planning.

8.3.2. Assumptions for ice-content

As mentioned in chapter 4, the estimation of ice or water content of rock glaciers is extremely challenging because of inaccessibility. Assumptions have been made by some studies by using field surveys (Boaga et al., 2020, Guillemot et al., 2020, Halla et al., 2021). However, if

a connection between ice-content and other characteristics such as velocity, topography or morphometry is assumed, it may be possible to estimate ice-content by using solely remote sensing data. Surface velocity, elevation, slope, roughness, curvature and several other information can be derived from satellite imagery and by using these as training data, a CNN would be suitable to automatically classify landforms into groups based on assumed ice-content (e. g. inactivity = low ice-content, low velocity + gentler topography = medium ice-content, high velocity + flow-like morphometry = high ice-content). Nevertheless, further research is needed to investigate the possibility of ice-content estimation with satellite data and deep-learning.

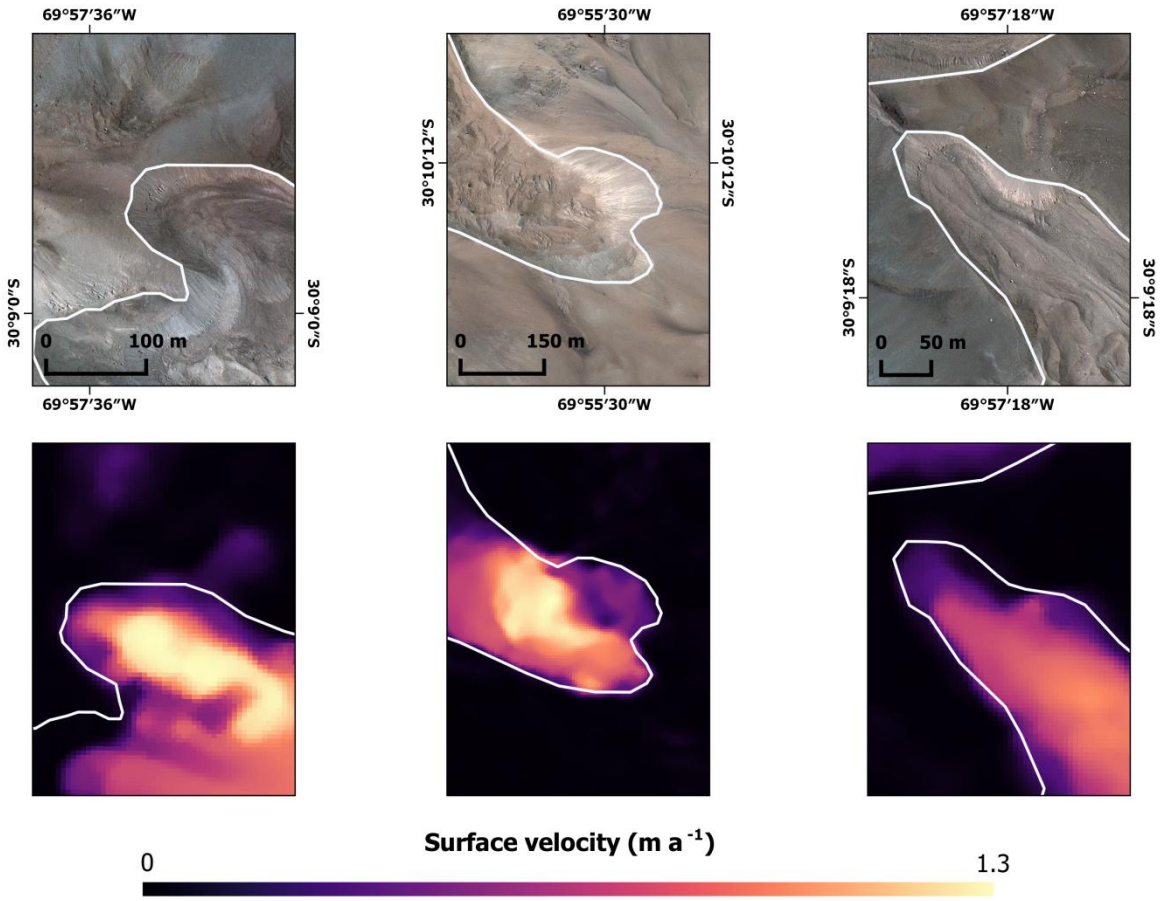

Figure 33: Active rock glaciers on the 2020 Pleiades orthomosaic (top) and satellite-derived velocity rates (bottom). Connection between geomorphometry (flow-like morphology, light coloured frontal slope, etc.) and velocity could be used to estimate ice-content.

9. Conclusion

The investigation showed that CNN together with OBIA is able to automatically detect rock glaciers and can be a useful tool when creating inventories. Two classification methods, *CNN_noCurv* and *CNN_wCurv* were developed and trained on Pleiades data of the first study area, the La Laguna catchment. The workflow further developed the method set out by Robson et al. (2020). The most suitable convolutional neural network (CNN) architecture was chosen on a trial and error basis which resulted in a probability heatmap of rock glaciers. Since the heatmap produced still contained false positives and negatives, object-based image analysis was performed to refine and reshape rock glacier outlines. The method was then applied to another set of Pleiades data showing the southern part of the Estero Derecho catchment and afterwards to SPOT 7 imagery that covered the northern side of the region. The goal was to investigate the method's transferability between different areas and sensor types. The results were then compared to a manually corrected rock glacier inventory.

Using only multispectral bands, DEM and slope layers, *CNN_noCurv* managed to achieve good classification accuracies, mapping 6.82 km^2 of validation rock glaciers out of a total 5.39 km^2, reaching a total accuracy of 73.54%. It was successfully loaded and applied on both the other Pleiades imagery and the SPOT 7 imagery. On those, it reached similar total accuracies, respectively 74.89 % and 73.15 %. Its mean user and producer accuracy was 72.83% and 78.4%. The method was then repeated with the inclusion of planform and curvature layers which were extracted from the DEM. The results showed that *CNN_wCurv* outperformed the first classification when it was applied on Pleiades data with all total accuracy rates higher than 94% and similar user and producer accuracies for both areas. On the other hand, the classification produced extremely bad results when transferred to SPOT 7 data. The reason might be differences in spatial resolution between Pleiades and SPOT 7 imagery and the excessive complexity of the CNN model the uses an eight layer-input.

User accuracies were in general higher than producer accuracies indicating that while the areas classified as rock glaciers were indeed rock glaciers, other rock glacier areas were missed by the classifications. A post-classification inspection showed that the majority of false negatives were landforms smaller than 0.05 km^2 or steep frontal slopes of rock glaciers that the classifications tended to exclude. False positives were mostly talus slopes, debris flows, fluvial deposits, rock avalanches with similar texture and morphology to rock glaciers.

It was also found that the CNN classifications managed to detect small rock glaciers that were not included in the manually created reference inventory.

In conclusion, the method presented in the thesis was found to be suitable to automatically detect large numbers of rock glaciers. It is time effective and can be run as a one workflow. Besides the high accuracy values comparable with other methods, the results also showed that the classification is able to find rock glaciers that have been missed by a human operator and therefore could even outperform the manual method. It was also found that the relationship between accuracy and mean surface velocity was weak and the methods were able to detect not only active but inactive rock glaciers as well. The comparison of *CNN_noCurv* and *CNN_wCurv* showed that adding curvature layers to the method can significantly improve the classification when applied on data that the CNN model was trained on. However, it is ineffective with data from another sensor. When using only the multispectral bands, the DEM and slope layers, the method produced less accurate results but became well transferable between different imageries. Therefore, when working on a smaller scale with imagery from one specific sensor, *CNN_wCurv* will likely be more effective, while when working with data of different origins and spatial resolution, it is more advised to use the *CNN_noCurv* method.

It is recommended to use CNN as an auxiliary tool in rock glacier mapping and to conduct research on how to further develop the workflow to reach a more accurate and transferable method. The method should be tested in a wider range of periglacial regions. The thesis focused on rock glaciers in two study areas in the semiarid Andes. These environments are characterized by dry climate, and lack of vegetation. It is crucial therefore to test the method on rock glaciers of different other environments such as the Himalayas, the Rockies or Svalbard and Greenland in order to develop a universally useful rock glacier mapping tool. In addition, the method can be used to support classification of active and inactive landforms or to estimate ice-content of rock glaciers.

10.References

ALLABY, M. 2013. Rock glacier. *A Dictionary of Geology and Earth Sciences.* Oxford: Oxford University Press.

ALSHEHHI, R., MARPU, P. R., WOON, W. L. & MURA, M. D. 2017. Simultaneous extraction of roads and buildings in remote sensing imagery with convolutional neural networks. *ISPRS Journal of Photogrammetry and Remote Sensing,* 130**,** 139-149.

ANDREASSEN, L. M., MOHOLDT, G., KÄÄB, A., MESSERLI, A., NAGY, T. & HAVSTAD WINSVOLD, S. 2021. Monitoring glaciers in mainland Norway and Svalbard using Sentinel. *In:* ANDREASSEN, L. M. (ed.). Oslo: NVE.

ARENSON, L., HOELZLE, M. & SPRINGMAN, S. 2002. Borehole deformation measurements and internal structure of some rock glaciers in Switzerland. *Permafrost and periglacial processes,* 13**,** 117-135.

ATHMANIA, D. & ACHOUR, H. 2014. External Validation of the ASTER GDEM2, GMTED2010 and CGIAR-CSI- SRTM v4.1 Free Access Digital Elevation Models (DEMs) in Tunisia and Algeria. *Remote sensing (Basel, Switzerland),* 6**,** 4600-4620.

AYALA, A., PELLICCIOTTI, F., MACDONELL, S., MCPHEE, J., VIVERO, S., CAMPOS, C. & EGLI, P. 2016. Modelling the hydrological response of debris-free and debris-covered glaciers to present climatic conditions in the semiarid Andes of central Chile. *Hydrological processes,* 30**,** 4036-4058.

AZÓCAR, G. F. & BRENNING, A. 2010a. Hydrological and geomorphological significance of rock glaciers in the dry Andes, Chile (27°–33°S. *Permafrost and Periglacial Processes,* 21**,** 42-53.

AZÓCAR, G. F. & BRENNING, A. 2010b. Hydrological and geomorphological significance of rock glaciers in the dry Andes, Chile (27°–33°S). *Permafrost and Periglacial Processes,* 21**,** 42-53.

BARCAZA, G., NUSSBAUMER, S. U., TAPIA, G., VALDÉS, J., GARCÍA, J.-L., VIDELA, Y., ALBORNOZ, A. & ARIAS, V. 2017. Glacier inventory and recent glacier variations in the Andes of Chile, South America. *Ann. Glaciol,* 58**,** 166-180.

BARR, I., DOKUKIN, M., KOUGKOULOS, I., LIVINGSTONE, S., LOVELL, H., MAŁECKI, J. & MURAVIEV, A. 2018. Using ArcticDEM to Analyse the Dimensions and Dynamics of Debris-Covered Glaciers in Kamchatka, Russia. *Geosciences (Basel),* 8**,** 216.

BARSCH, D. 1996. *Rockglaciers : indicators for the present and former geoecology in high mountain environments,* Berlin, Springer.

BENISTON, M. 1999. Global Environmental Change in Mountain Regions: An Overview. *Geographica Helvetica,* 54**,** 120-124.

BENISTON, M. 2003. Climatic change in mountain regions: A review of possible impacts. *Climatic Change,* 59**,** 5-31.

BENZ, U. C., HOFMANN, P., WILLHAUCK, G., LINGENFELDER, I. & HEYNEN, M. 2004. Multi-resolution, object-oriented fuzzy analysis of remote sensing data for GIS-ready information. *ISPRS Journal of Photogrammetry and Remote Sensing,* 58**,** 239-258.

BERTA, S. M. 1982. Analysis and Interpretation of Spectral Reflectance Signatures from Rock Glaciers. Oklahoma State University.

BERTHIER, E., VADON, H., BARATOUX, D., ARNAUD, Y., VINCENT, C., FEIGL, K. L., RÉMY, F. & LEGRÉSY, B. 2005. Surface motion of mountain glaciers derived from satellite optical imagery. *Remote Sensing of Environment,* 95**,** 14-28.

BERTHLING, I. 2011. Beyond confusion: Rock glaciers as cryo-conditioned landforms. *Geomorphology (Amsterdam, Netherlands),* 131**,** 98-106.

BILAL, M., NAZEER, M., NICHOL, J. E., BLEIWEISS, M. P., QIU, Z., JÄKEL, E., CAMPBELL, J. R., ATIQUE, L., HUANG, X. & LOLLI, S. 2019. A Simplified and Robust Surface Reflectance Estimation Method (SREM) for Use over Diverse Land Surfaces Using Multi-Sensor Data. *Remote sensing (Basel, Switzerland),* 11**,** 1344.

BLASCHKE, T. 2010. Object based image analysis for remote sensing. *ISPRS Journal of Photogrammetry and Remote Sensing,* 65**,** 2-16.

BLASCHKE, T., HAY, G. J., KELLY, M., LANG, S., HOFMANN, P., ADDINK, E., QUEIROZ FEITOSA, R., VAN DER MEER, F., VAN DER WERFF, H., VAN COILLIE, F. & TIEDE, D. 2014. Geographic Object-Based Image Analysis – Towards a new paradigm. *ISPRS Journal of Photogrammetry and Remote Sensing,* 87**,** 180-191.

BLÖTHE, J. H., HALLA, C., SCHWALBE, E., BOTTEGAL, E., TROMBOTTO LIAUDAT, D. & SCHROTT, L. 2021. Surface velocity fields of active rock glaciers and ice-debris complexes in the Central Andes of Argentina. *Earth Surface Processes and Landforms,* 46**,** 504-522.

BOAGA, J., PHILLIPS, M., NOETZLI, J., HABERKORN, A., KENNER, R. & BAST, A. 2020. A Comparison of Frequency Domain Electro-Magnetometry, Electrical Resistivity Tomography and Borehole Temperatures to Assess the Presence of Ice in a Rock Glacier. *Frontiers in Earth Science,* 8.

BOLCH, T., ROHRBACH, N., KUTUZOV, S., ROBSON, B. A. & OSMONOV, A. 2019. Occurrence, evolution and ice content of ice-debris complexes in the Ak-Shiirak, Central Tien Shan revealed by geophysical and remotely-sensed investigations. *Earth surface processes and landforms,* 44**,** 129-143.

BRENNING, A. 2005. *Climatic and geomorphological controls of rock glaciers in the Andes of Central Chile.*

BRENNING, A. 2009. Benchmarking classifiers to optimally integrate terrain analysis and multispectral remote sensing in automatic rock glacier detection. *Remote Sensing of Environment,* 113**,** 239-247.

BRENNING, A., LONG, S. & FIEGUTH, P. 2012. Detecting rock glacier flow structures using Gabor filters and IKONOS imagery. *Remote sensing of environment,* 125**,** 227-237.

BURNETT, C. & BLASCHKE, T. 2003. A multi-scale segmentation/object relationship modelling methodology for landscape analysis. *Ecological modelling,* 168**,** 233-249.

BUYTAERT, W., MOULDS, S., ACOSTA, L., DE BIÈVRE, B., OLMOS, C., VILLACIS, M., TOVAR, C. & VERBIST, K. M. J. 2016. Glacial melt content of water use in the tropical Andes. *Environ. Res. Lett,* 12**,** 114014.

CARBONNEAU, P. E., BELLETTI, B., MICOTTI, M., LASTORIA, B., CASAIOLI, M., MARIANI, S., MARCHETTI, G. & BIZZI, S. 2020. UAV-based training for fully fuzzy classification of Sentinel-2 fluvial scenes. *Earth surface processes and landforms,* 45**,** 3120-3140.

CHATTERJEE, C. C. 2019. *Basics of Classic CNN* [Online]. Towards Data Science. Available: https://towardsdatascience.com/basics-of-the-classic-cnn-a3dce1225add [Accessed 05.03 2021].

CHEN, Y., QIN, S., QIAO, S., DOU, Q., CHE, W., SU, G., YAO, J. & NNANWUBA, U. E. 2020. Spatial Predictions of Debris Flow Susceptibility Mapping Using Convolutional Neural Networks in Jilin Province, China. *Water (Basel),* 12**,** 2079.

CLAPPERTON, C. 1993. *Quaternary geology and geomorphology of South America,* Amsterdam, Elsevier.

COLUCCI, R. R., FORTE, E., ŽEBRE, M., MASET, E., ZANETTINI, C. & GUGLIELMIN, M. 2019. Is that a relict rock glacier? *Geomorphology (Amsterdam, Netherlands),* 330**,** 177-189.

CORRIPIO, J. 2003. Vectorial algebra algorithms for calculating terrain parameters from DEMs and solar radiation modeling in mountainous terrain. *International Journal of Geographical Information Science,* 17**,** 1-23.

CSILLIK, O., CHERBINI, J., JOHNSON, R., LYONS, A. & KELLY, M. 2018. Identification of Citrus Trees from Unmanned Aerial Vehicle Imagery Using Convolutional Neural Networks. *Drones (Basel),* 2**,** 39.

DE BEM, P., DE CARVALHO JUNIOR, O., FONTES GUIMARÃES, R. & TRANCOSO GOMES, R. 2020. Change Detection of Deforestation in the Brazilian Amazon Using Landsat Data and Convolutional Neural Networks. *Remote sensing (Basel, Switzerland),* 12**,** 901.

DE PASQUALE, G., VALOIS, R., SCHAFFER, N. & MACDONELL, S. 2020. Active and inactive Andean rock glacier geophysical signatures by comparing 2D joint inversion routines of electrical resistivity and refraction seismic tomography. *The Cryosphere Discuss.,* 2020**,** 1-33.

DEBELLA-GILO, M. & KÄÄB, A. 2011. Sub-pixel precision image matching for measuring surface displacements on mass movements using normalized cross-correlation. *Remote sensing of environment,* 115**,** 130-142.

DRĂGUŢ, L., CSILLIK, O., EISANK, C. & TIEDE, D. 2014. Automated parameterisation for multi-scale image segmentation on multiple layers. *ISPRS Journal of Photogrammetry and Remote Sensing,* 88**,** 119-127.

EHSANI, A. & MALEKIAN, A. 2021. Landforms identification using neural network-self organizing map and SRTM data.

ERIKSEN, H. Ø., ROUYET, L., LAUKNES, T. R., BERTHLING, I., ISAKSEN, K., HINDBERG, H., LARSEN, Y. & CORNER, G. D. 2018. Recent Acceleration of a Rock Glacier Complex, Ádjet, Norway, Documented by 62 Years of Remote Sensing Observations. *Geophysical Research Letters,* 45**,** 8314-8323.

ERZHU, L., JUNSHI, X., PEIJUN, D., CONG, L. & ALIM, S. 2017. Integrating Multilayer Features of Convolutional Neural Networks for Remote Sensing Scene Classification. *IEEE Transactions on Geoscience and Remote Sensing,* 55**,** 5653-5665.

FALASCHI, D., CASTRO, M., MASIOKAS, M., TADONO, T. & AHUMADA, A. L. 2014. Rock Glacier Inventory of the Valles Calchaquíes Region (~ 25°S), Salta, Argentina, Derived from ALOS Data. *Permafrost and Periglacial Processes,* 25**,** 69-75.

FANG, L., HOEGNER, L. & STILLA, U. 2015. AUTOMATIC MAPPING OF GLACIER BASED ON SAR IMAGERY BY BENEFITS OF FREELY OPTICAL AND THERMAL DATA. *International archives of the photogrammetry, remote sensing and spatial information sciences.,* XL**,** 47-51.

FAVIER, V., FALVEY, M., RABATEL, A., PRADERIO, E. & LÓPEZ, D. 2009. Interpreting discrepancies between discharge and precipitation in high-altitude area of Chile's Norte Chico region (26–32°S. *Water Resources Research,* 45**,** n/a-n/a.

FERESHTEHPOUR, M. & KARAMOUZ, M. 2018. DEM Resolution Effects on Coastal Flood Vulnerability Assessment: Deterministic and Probabilistic Approach. *Water Resources Research,* 54**,** 4965-4982.

FIEBIG-WITTMAACK, M., ASTUDILLO, O., WHEATON, E., WITTROCK, V., PEREZ, C. & IBACACHE, A. 2012. Climatic trends and impact of climate change on agriculture in an arid Andean valley. *Climatic Change,* 111**,** 819-833.

GARDNER, J. & BAJEWSKY, I. 1987. Hilda rock glacier stream discharge and sediment load characteristics, Sunwapta Pass area, Canadian Rocky Mountains. *Rock glaciers***,** 161-174.

GASCOIN, S., KINNARD, C., PONCE, R., LHERMITTE, S., MACDONELL, S. & RABATEL, A. 2011. Glacier contribution to streamflow in two headwaters of the Huasco River, Dry Andes of Chile. *The cryosphere,* 5**,** 1099-1113.

GEOMATICA. 2013. *Atmospheric Correction (with ATCOR)* [Online]. Available: https://www.pcigeomatics.com/pdf/AtmosphericCorrection.pdf [Accessed 05.03 2021].

GHORBANZADEH, O., MEENA, S. R., BLASCHKE, T. & ARYAL, J. 2019. UAV-Based Slope Failure Detection Using Deep-Learning Convolutional Neural Networks. *Remote sensing (Basel, Switzerland),* 11**,** 2046.

GIARDINO, J. R. & VITEK, J. D. 1988. The significance of rock glaciers in the glacial-periglacial landscape continuum. *Journal of Quaternary Science,* 3**,** 97-103.

GJERMUNDSEN, E. F., MATHIEU, R., KÄÄB, A., CHINN, T., FITZHARRIS, B. & HAGEN, J. O. 2011. Assessment of multispectral glacier mapping methods and derivation of glacier area changes, 1978–2002, in the central Southern Alps, New Zealand, from ASTER satellite data, field survey and existing inventory data. *J. Glaciol,* 57**,** 667-683.

GONG, K. & FRITSCH, D. 2016. A DETAILED STUDY ABOUT DIGITAL SURFACE MODEL GENERATION USING HIGH RESOLUTION SATELLITE STEREO IMAGERY. *ISPRS annals of the photogrammetry, remote sensing and spatial information sciences,* III-1**,** 69-76.

GUILLEMOT, A., HELMSTETTER, A., LAROSE, É., BAILLET, L., GARAMBOIS, S., MAYORAZ, R. & DELALOYE, R. 2020. Seismic monitoring in the Gugla rock glacier (Switzerland): ambient noise correlation, microseismicity and modelling. *Geophysical Journal International,* 221**,** 1719-1735.

HAEBERLI, W. & BENISTON, M. 1998. Climate Change and its Impacts on Glaciers and Permafrost in the Alps. *Ambio,* 27**,** 258-265.

HAEBERLI, W., HALLET, B., ARENSON, L., ELCONIN, R., HUMLUM, O., KÄÄB, A., KAUFMANN, V., LADANYI, B., MATSUOKA, N., SPRINGMAN, S. & MÜHLL, D. V. 2006. Permafrost creep and rock glacier dynamics. *Permafrost and periglacial processes,* 17**,** 189-214.

HALDAR, S. K. 2018. Chapter 3 - Photogeology, Remote Sensing, and Geographic Information System in Mineral Exploration. *In:* HALDAR, S. K. (ed.) *Mineral Exploration (Second Edition).* Elsevier.

HALL, D. K. & MARTINEC, J. 1985. *Remote sensing of ice and snow,* London, Chapman and Hall.

HALLA, C., BLÖTHE, J. H., TAPIA BALDIS, C., TROMBOTTO LIAUDAT, D., HILBICH, C., HAUCK, C. & SCHROTT, L. 2021. Ice content and interannual water storage changes of an active rock glacier in the dry Andes of Argentina. *The Cryosphere,* 15**,** 1187-1213.

HARIS, M. & KHAN, R. Z. 2018. *A Systematic Review on Cloud Computing*.

HASSANI, N. J. M. 2018. *Stereoscopic Parallax* [Online]. Available: https://forestrypedia.com/stereoscopic-parallax/ [Accessed 04.03 2021].

HEDLEY, J. D., ROELFSEMA, C. M., PHINN, S. R. & MUMBY, P. J. 2012. Environmental and Sensor Limitations in Optical Remote Sensing of Coral Reefs: Implications for Monitoring and Sensor Design. *Remote sensing (Basel, Switzerland),* 4**,** 271-302.

HIRSCHMULLER, H. 2008. Stereo Processing by Semiglobal Matching and Mutual Information. *IEEE Trans Pattern Anal Mach Intell,* 30**,** 328-341.

HOBSON, R. D. 1972. Surface roughness in topography: quantitative approach. *In:* CHORLEY, R. J. (ed.) *Spatial analysis in geomorphology.* London: Methuer.

HOFER, T. 2005. Introduction: The International Year of Mountains Challenge and Opportunity for Mountain Research. *In:* HUBER, U. M., BUGMANN, H. K. M. & REASONER, M. A. (eds.) *Global Change and Mountain Regions: An Overview of Current Knowledge.* Dordrecht: Springer Netherlands.

HUANG, L., LIU, L., JIANG, L. & ZHANG, T. 2018. Automatic Mapping of Thermokarst Landforms from Remote Sensing Images Using Deep Learning: A Case Study in the Northeastern Tibetan Plateau. *Remote sensing (Basel, Switzerland),* 10**,** 2067.

JANKE, J. R. 2001. Rock Glacier Mapping: A Method Utilizing Enhanced TM Data and GIS Modeling Techniques. *Geocarto international,* 16**,** 5-15.

JANKE, J. R., NG, S. & BELLISARIO, A. 2017. An inventory and estimate of water stored in firn fields, glaciers, debris-covered glaciers, and rock glaciers in the Aconcagua River Basin, Chile. *Geomorphology (Amsterdam, Netherlands),* 296**,** 142-152.

JANKE, J. R., REGMI, N. R., GIARDINO, J. R. & VITEK, J. D. 2013. 8.17 Rock Glaciers. *In:* SHRODER, J. F. (ed.) *Treatise on Geomorphology.* San Diego: Academic Press.

JASON, R. J. 2007. Colorado Front Range Rock Glaciers: Distribution and Topographic Characteristics. *Arctic, antarctic, and alpine research,* 39**,** 74-83.

JI, L. & GONG, P. 2018. 4.11 - Surface Water. *In:* LIANG, S. (ed.) *Comprehensive Remote Sensing.* Oxford: Elsevier.

JONES, D., HARRISON, S., ANDERSON, K. & BETTS, R. 2018a. Mountain rock glaciers contain globally significant water stores. *Sci Rep,* 8**,** 2834-2834.

JONES, D. B., HARRISON, S., ANDERSON, K., SELLEY, H. L., WOOD, J. L. & BETTS, R. A. 2018b. The distribution and hydrological significance of rock glaciers in the Nepalese Himalaya. *Global and planetary change,* 160**,** 123-142.

JONES, D. B., HARRISON, S., ANDERSON, K., SELLEY, H. L., WOOD, J. L. & BETTS, R. A. 2018c. The distribution and hydrological significance of rock glaciers in the Nepalese Himalaya. *Global and Planetary Change,* 160**,** 123-142.

JONES, D. B., HARRISON, S., ANDERSON, K. & WHALLEY, W. B. 2019. Rock glaciers and mountain hydrology: A review. *Earth-Science Reviews,* 193**,** 66-90.

KÄÄB, A. 2013. Rock Glaciers and Protalus Forms.

KÄÄB, A., HAEBERLI, W. & GUDMUNDSSON, G. H. 1997. Analysing the creep of mountain permafrost using high precision aerial photogrammetry: 25 years of monitoring Gruben rock glacier, Swiss Alps. *Permafrost and periglacial processes,* 8**,** 409-426.

KÄÄB, A., KAUFMANN, V., LADSTÄDTER, R. & EIKEN, T. 2003. Rock glacier dynamics: Implications from high-resolution measurements of surface velocity fields. *Permafrost***,** 501-506.

KÄÄB, A., STROZZI, T., BOLCH, T., CADUFF, R., TREFALL, H., STOFFEL, M. & KOKAREV, A. 2021. Inventory and changes of rock glacier creep speeds in Ile Alatau and Kungöy Ala-Too, northern Tien Shan, since the 1950s. *The Cryosphere,* 15**,** 927-949.

KÄÄB, A. & WEBER, M. 2004. Development of transverse ridges on rock glaciers: field measurements and laboratory experiments. *Permafrost and periglacial processes,* 15**,** 379-391.

KAUFMANN, V. 2012. Detection and Quantification of Rock Glacier Creep Using High-resolution Orthoimages of Virtual Globes. *Int. Arch. Photogramm. Remote Sens. Spatial Inf. Sci.,* XXXIX-B5**,** 517-522.

KAUFMANN, V., SEIER, G., SULZER, W., WECHT, M., LIU, Q., LAUK, G. & MAURER, M. 2018. ROCK GLACIER MONITORING USING AERIAL PHOTOGRAPHS: CONVENTIONAL VS. UAV-BASED MAPPING – A COMPARATIVE STUDY. *International archives of the photogrammetry, remote sensing and spatial information sciences.,* XLII-1**,** 239-246.

KELLERER-PIRKLBAUER, A., LIEB, G. & KLEINFERCHNER, H. 2010. A new rock glacier inventory of the Eastern European Alps. *Austrian journal of Earth Sciences,* 105.

KETTIG, R. L. & LANDGREBE, D. A. 1976. Classification of Multispectral Image Data by Extraction and Classification of Homogeneous Objects. *IEEE transactions on geoscience electronics,* 14**,** 19-26.

KHORRAM, S., KOCH, F. H., VAN DER WIELE, C. F. & NELSON, S. A. C. 2012. Remote Sensing. 1st ed. 2012. ed. New York, NY: Springer New York : Imprint: Springer.

KOFLER, C., STEGER, S., MAIR, V., ZEBISCH, M., COMITI, F. & SCHNEIDERBAUER, S. 2020. An inventory-driven rock glacier status model (intact vs. relict) for South Tyrol, Eastern Italian Alps. *Geomorphology (Amsterdam, Netherlands),* 350**,** 106887.

KRAAIJENBRINK, P. D. A., SHEA, J. M., PELLICCIOTTI, F., JONG, S. M. D. & IMMERZEEL, W. W. 2016. Object-based analysis of unmanned aerial vehicle imagery to map and characterise surface features on a debris-covered glacier. *Remote sensing of environment,* 186**,** 581-595.

KRAINER, K. & MOSTLER, W. 2002. Hydrology of Active Rock Glaciers: Examples from the Austrian Alps. *Arctic, antarctic, and alpine research,* 34**,** 142.

KRAINER, K., MOSTLER, W. & SPÖTL, C. 2007. Discharge from active rock glaciers, Austrian Alps: A stable isotope approach. *Austrian Journal of Earth Sciences,* 100**,** 102-112.

KRYSIAK, S., PAPIŃSKA, E., MAJCHROWSKA, A., ADAMIAK, M. & KOZIARKIEWICZ, M. 2020. Detecting Land Abandonment in Łódź Voivodeship Using Convolutional Neural Networks. *Land (Basel),* 9**,** 82.

LANG, S. & LANGANKE, T. 2006. Object-based mapping and object-relationship modeling for land use classes and habitats. *Photogrammetrie, Fernerkundung, Geoinformation,* 10**,** 5-18.

LI, Z., WU, Q., CHENG, B., CAO, L. & YANG, H. 2020. Remote Sensing Image Scene Classification Based on Object Relationship Reasoning CNN. *IEEE geoscience and remote sensing letters***,** 1-5.

LIANGPEI, Z., LEFEI, Z. & BO, D. 2016. Deep Learning for Remote Sensing Data: A Technical Tutorial on the State of the Art. *IEEE Geoscience and Remote Sensing Magazine,* 4**,** 22-40.

LIPPL, S., VIJAY, S. & BRAUN, M. 2018. Automatic delineation of debris-covered glaciers using InSAR coherence derived from X-, C- and L-band radar data: a case study of Yazgyl Glacier. *J. Glaciol,* 64**,** 811-821.

LITJENS, G., KOOI, T., BEJNORDI, B. E., SETIO, A. A. A., CIOMPI, F., GHAFOORIAN, M., VAN DER LAAK, J. A. W. M., VAN GINNEKEN, B. & SÁNCHEZ, C. I. 2017. A survey on deep learning in medical image analysis. *Med Image Anal,* 42**,** 60-88.

LIU, K., SONG, C., KE, L., JIANG, L., PAN, Y. & MA, R. 2019. Global open-access DEM performances in Earth's most rugged region High Mountain Asia: A multi-level assessment. *Geomorphology (Amsterdam, Netherlands),* 338**,** 16-26.

LIU, L., MILLAR, C., WESTFALL, R. & ZEBKER, H. 2013. Surface motion of active rock glaciers in the Sierra Nevada, California, USA: inventory and a case study using InSAR. *The Cryosphere,* 7**,** 1109.

MA, L., CRAWFORD, M. M. & TIAN, J. 2010. Local Manifold Learning-Based k -Nearest-Neighbor for Hyperspectral Image Classification. *IEEE Transactions on Geoscience and Remote Sensing,* 48**,** 4099-4109.

MA, L., LIU, Y., ZHANG, X., YE, Y., YIN, G. & JOHNSON, B. A. 2019. Deep learning in remote sensing applications: A meta-analysis and review. *ISPRS Journal of Photogrammetry and Remote Sensing,* 152**,** 166-177.

MAHYARI, A. & YAZDI, M. 2011. Panchromatic and Multispectral Image Fusion Based on Maximization of Both Spectral and Spatial Similarities. *Geoscience and Remote Sensing, IEEE Transactions on,* 49**,** 1976-1985.

MARCER, M. 2020. Rock glaciers automatic mapping using optical imagery and convolutional neural networks. *Permafrost and periglacial processes,* 31**,** 561-566.

MCGRATH, M. & NI SCANAILL, C. 2013. Sensing and Sensor Fundamentals.

MCNABB, R. W., WOMBLE, J. N., PRAKASH, A., GENS, R. & HASELWIMMER, C. E. 2016. Quantification and Analysis of Icebergs in a Tidewater Glacier Fjord Using an Object-Based Approach. *PLoS One,* 11**,** e0164444.

MILANA, J. & GÜELL, A. 2008. Diferencias mecánicas e hídricas del permafrost en glaciares de rocas glacigénicos y criogénicos, obtenidas de datos sísmicos en El Tapado, Chile. *Revista de la Asociación Geológica Argentina,* 63**,** 310-325.

MOHAJERANI, Y., WOOD, M., VELICOGNA, I. & RIGNOT, E. 2019. Detection of Glacier Calving Margins with Convolutional Neural Networks: A Case Study. *Remote sensing (Basel, Switzerland),* 11**,** 74.

MONNIER, S., CAMERLYNCK, C. & REJIBA, F. 2008. Ground penetrating radar survey and stratigraphic interpretation of the Plan du Lac rock glaciers, Vanoise Massif, northern French Alps. *Permafrost and periglacial processes,* 19**,** 19-30.

MONNIER, S. & KINNARD, C. 2015a. Internal Structure and Composition of a Rock Glacier in the Dry Andes, Inferred from Ground-penetrating Radar Data and its Artefacts: GPR for Inferring the Composition of Rock Glacier. *Permafrost and periglacial processes,* 26**,** 335-346.

MONNIER, S. & KINNARD, C. 2015b. Reconsidering the glacier to rock glacier transformation problem: New insights from the central Andes of Chile. *Geomorphology,* 238**,** 47-55.

MONNIER, S. & KINNARD, C. 2017. Pluri-decadal (1955-2014) evolution of glacier-rock glacier transitional landforms in the central Andes of Chile (30-33° S). *Earth Surface Dynamics,* 5**,** 493-509.

MONNIER, S., KINNARD, C., SURAZAKOV, A. & BOSSY, W. 2014a. Geomorphology, internal structure, and successive development of a glacier foreland in the semiarid Chilean Andes (Cerro Tapado, upper Elqui Valley, 30°08’ S., 69°55’ W.). *Geomorphology,* 207**,** 126-140.

MONNIER, S., KINNARD, C., SURAZAKOV, A. & BOSSY, W. 2014b. Geomorphology, internal structure, and successive development of a glacier foreland in the semiarid Chilean Andes (Cerro Tapado, upper Elqui Valley, 30°08’ S., 69°55’ W.). *Geomorphology,* 207**,** 126-140.

MYERS-SMITH, I. H., KERBY, J. T., PHOENIX, G. K., BJERKE, J. W., EPSTEIN, H. E., ASSMANN, J. J., JOHN, C., ANEU-HAYLES, L., ANGERS-BLONDIN, S., BECK, P. S. A., BERNER, L. T., BHATT, U. S., BJORKMAN, A. D., BLOK, D., BRYN, A., CHRISTIANSEN, C. T., CORNELISSEN, J. H. C., CUNLIFFE, A. M., ELMENDORF, S. C., FORBES, B. C., GOETZ, S. J., HOLLISTER, R. D., DE JONG, R., LORANTY, M. M., MACIAS-FAURIA, M., MASEYK, K., NORMAND, S., OLOFSSON, J., PARKER, T. C., PARMENTIER, F. J. W., POST, E., SCHAEPMAN-STRUB, G., STORDAL, F., SULLIVAN, P. F., THOMAS, H. J. D., TØMMERVIK, H., TREHARNE, R., TWEEDIE, C. E., WALKER, D. A.,

WILMKING, M. & WIPF, S. 2020. Complexity revealed in the greening of the Arctic. *Nature climate change,* 10**,** 106-117.
NECSOIU, M., ONACA, A., WIGGINTON, S. & URDEA, P. 2016. Rock glacier dynamics in Southern Carpathian Mountains from high-resolution optical and multi-temporal SAR satellite imagery. *Remote Sensing of Environment,* 177**,** 21-36.
OUTCALT, S. I. & BENEDICT, J. B. 1965. Photo-Interpretation of two Types of Rock Glacier in the Colorado Front Range, U.S.A. *Journal of glaciology,* 5**,** 849-856.
PANDEY, P. 2019. Inventory of rock glaciers in Himachal Himalaya, India using high-resolution Google Earth imagery. *Geomorphology (Amsterdam, Netherlands),* 340**,** 103-115.
PEÑA, H. & NAZARALA, B. 1987. Snowmelt-runoff simulation model of a central Chile Andean basin with relevant orographic effects. *IAHS-AISH publication***,** 161-172.
PERUCCA, L. & ESPER ANGILLIERI, M. Y. 2011. Glaciers and rock glaciers' distribution at 28° SL, Dry Andes of Argentina, and some considerations about their hydrological significance. *Environmental earth sciences,* 64**,** 2079-2089.
PHUNG & RHEE 2019. A High-Accuracy Model Average Ensemble of Convolutional Neural Networks for Classification of Cloud Image Patches on Small Datasets. *Applied Sciences,* 9**,** 4500.
PLACZEK, C., QUADE, J., BETANCOURT, J. L., PATCHETT, P. J., RECH, J. A., LATORRE, C., MATMON, A., HOLMGREN, C. & ENGLISH, N. B. 2009. CLIMATE IN THE DRY CENTRAL ANDES OVER GEOLOGIC, MILLENNIAL, AND INTERANNUAL TIMESCALES 1. *Annals of the Missouri Botanical Garden,* 96**,** 386-397.
POLSBY, D. D. & POPPER, R. D. 1991. The Third Criterion: Compactness as a Procedural Safeguard against Partisan Gerrymandering. *Yale law & policy review,* 9**,** 301-353.
POURRIER, J., JOURDE, H., KINNARD, C., GASCOIN, S. & MONNIER, S. 2014. Glacier meltwater flow paths and storage in a geomorphologically complex glacial foreland: The case of the Tapado glacier, dry Andes of Chile (30°S). *Journal of Hydrology,* 519**,** 1068-1083.
PRAKASH, N., MANCONI, A. & LOEW, S. 2021. A new strategy to map landslides with a generalized convolutional neural network. *Sci Rep,* 11**,** 9722-9722.
RABATEL, A., CASTEBRUNET, H., FAVIER, V., NICHOLSON, L. & KINNARD, C. 2010. Glacier changes in the Pascua-Lama region, Chilean Andes (29° S): recent mass-balance and 50-year surface-area variations. *The Cryosphere Discussions,* 4**,** 2307-2336.
RAJU, A. & SHANTHI, T. 2020. Convolutional Neural Network Demystified for a Comprehensive Learning with Industrial Application.
RANGECROFT, S., HARRISON, S. & ANDERSON, K. 2015. Rock Glaciers as Water Stores in the Bolivian Andes: An Assessment of Their Hydrological Importance. *Arctic, Antarctic, and Alpine Research,* 47**,** 89-98.
RANGECROFT, S., HARRISON, S., ANDERSON, K., MAGRATH, J., CASTEL, A. P. & PACHECO, P. 2014. A First Rock Glacier Inventory for the Bolivian Andes. *Permafrost and Periglacial Processes,* 25**,** 333-343.
RASTNER, P., BOLCH, T., NOTARNICOLA, C. & PAUL, F. 2014. A Comparison of Pixel- and Object-Based Glacier Classification With Optical Satellite Images. *IEEE Journal of Selected Topics in Applied Earth Observations and Remote Sensing,* 7**,** 853-862.
RILEY, S., DEGLORIA, S. & ELLIOT, S. D. 1999. A Terrain Ruggedness Index that Quantifies Topographic Heterogeneity. *Internation Journal of Science,* 5**,** 23-27.
ROBSON, B. A. 2016. *Quantification and change assessment of debris-covered glaciers using remote sensing.* Doctoral dissertation, University of Bergen.
ROBSON, B. A., BOLCH, T., MACDONELL, S., HÖLBLING, D., RASTNER, P. & SCHAFFER, N. 2020. Automated detection of rock glaciers using deep learning and object-based image analysis. *Remote sensing of environment,* 250**,** 112033.
ROBSON, B. A., NUTH, C., DAHL, S. O., HÖLBLING, D., STROZZI, T. & NIELSEN, P. R. 2015. Automated classification of debris-covered glaciers combining optical, SAR and topographic data in an object-based environment. *Remote Sensing of Environment,* 170**,** 372-387.

RODRIGUEZ, M., OHLANDERS, N., PELLICCIOTTI, F., WILLIAMS, M. W. & MCPHEE, J. 2016. Estimating runoff from a glacierized catchment using natural tracers in the semi-arid Andes cordillera. *Hydrological processes,* 30**,** 3609-3626.

SAHU, R. & GUPTA, R. D. 2018. CONCEPTUAL FRAMEWORK OF COMBINED PIXEL AND OBJECT-BASED METHOD FOR DELINEATION OF DEBRIS-COVERED GLACIERS. *ISPRS annals of the photogrammetry, remote sensing and spatial information sciences,* IV-5**,** 173-180.

SCHAFFER, N., MACDONELL, S., RÉVEILLET, M., YÁÑEZ, E. & VALOIS, R. 2019. Rock glaciers as a water resource in a changing climate in the semiarid Chilean Andes. *Regional Environmental Change,* 19**,** 1263-1279.

SCHMID, M. O., BARAL, P., GRUBER, S., SHAHI, S., SHRESTHA, T., STUMM, D. & WESTER, P. 2015. Assessment of permafrost distribution maps in the Hindu Kush Himalayan region using rock glaciers mapped in Google Earth. *The cryosphere,* 9**,** 2089-2099.

SCHROTT, L. 1996. Some geomorphological-hydrological aspects of rock glaciers in the Andes (San Juan, Argentina). *Zeitschrift fur Geomorphologie, Supplementband,* 104**,** 161-173.

SCHUCKMAN, K. & DUTTON, J. A. 2018. *Band Math* [Online]. The Pennsylvania State University. Available: https://www.e-education.psu.edu/geog480/node/524 [Accessed 05/05/2020].

SCOTTI, R., BRARDINONI, F., ALBERTI, S., FRATTINI, P. & CROSTA, G. B. 2013. A regional inventory of rock glaciers and protalus ramparts in the central Italian Alps. *Geomorphology (Amsterdam, Netherlands),* 186**,** 136-149.

SHARMA, A., LIU, X., YANG, X. & SHI, D. 2017. A patch-based convolutional neural network for remote sensing image classification. *Neural Networks,* 95**,** 19-28.

SHEAN, D. E., ALEXANDROV, O., MORATTO, Z. M., SMITH, B. E., JOUGHIN, I. R., PORTER, C. & MORIN, P. 2016. An automated, open-source pipeline for mass production of digital elevation models (DEMs) from very-high-resolution commercial stereo satellite imagery. *ISPRS journal of photogrammetry and remote sensing,* 116**,** 101-117.

SINCLAIR, K. E. & MACDONELL, S. 2016. Seasonal evolution of penitente glaciochemistry at Tapado Glacier, Northern Chile. *Hydrological Processes,* 30**,** 176-186.

SONG, J., GAO, S., ZHU, Y. & MA, C. 2019. A survey of remote sensing image classification based on CNNs. *Big earth data,* 3**,** 232-254.

SONOBE, R., TANI, H., WANG, X., KOBAYASHI, N. & SHIMAMURA, H. 2014. Random forest classification of crop type using multi-temporal TerraSAR-X dual-polarimetric data. *Remote Sensing Letters,* 5**,** 157-164.

STROZZI, T., CADUFF, R., JONES, N., BARBOUX, C., DELALOYE, R., BODIN, X., KÄÄB, A., MÄTZLER, E. & SCHROTT, L. 2020. Monitoring Rock Glacier Kinematics with Satellite Synthetic Aperture Radar. *Remote Sensing,* 12**,** 559.

TIMILSINA, S., SHARMA, S. K. & ARYAL, J. 2019. MAPPING URBAN TREES WITHIN CADASTRAL PARCELS USING AN OBJECT-BASED CONVOLUTIONAL NEURAL NETWORK. *ISPRS annals of the photogrammetry, remote sensing and spatial information sciences,* IV-5/W2**,** 111-117.

TRIGLAV-ČEKADA, M., BARBORIČ, B., FERK, M. & ZORN, M. 2016. Nationwide aerial laser scanning reveals relict rock glaciers and protalus ramparts in Slovenia. *The Cryosphere Discussions***,** 1-17.

TROMBOTTO, D., BUK, E. & HERNÁNDEZ, J. 1997. Monitoring of Mountain Permafrost in the Central Andes, Cordon del Plata, Mendoza, Argentina. *Permafrost and periglacial processes,* 8**,** 123-129.

TYAGI, P. & BHOSLE, U. 2011. Atmospheric Correction of Remotely Sensed Images in Spatial and Transform Domain. *International Journal of Image Processing,* 5**,** 564-579.

VALOIS, R., SCHAFFER, N., FIGUEROA, R., MALDONADO, A., YÁÑEZ, E., HEVIA, A., YÁNEZ CARRIZO, G. & MACDONELL, S. 2020. Characterizing the Water Storage Capacity and Hydrological Role of Mountain Peatlands in the Arid Andes of North-Central Chile. *Water (Basel),* 12**,** 1071.

VILLARROEL, C. D., BELIVEAU, G. T., FORTE, A. P., MONSERRAT, O. & MORVILLO, M. 2018a. DInSAR for a Regional Inventory of Active Rock Glaciers in the Dry Andes Mountains of Argentina and Chile with Sentinel-1 Data. *Remote Sensing,* 10**,** 1588.

VILLARROEL, C. D., TAMBURINI BELIVEAU, G., FORTE, A. P., MONSERRAT, O. & MORVILLO, M. 2018b. DInSAR for a Regional Inventory of Active Rock Glaciers in the Dry Andes Mountains of Argentina and Chile with Sentinel-1 Data. *Remote Sensing,* 10**,** 1588.

WAHRHAFTIG, C. & COX, A. 1959. Rock glaciers in the Alaska Range. *Geological Society of America Bulletin,* 70**,** 383-436.

WANG, S., WANG, M., ZHAO, X. & LIU, D. Two-Stage Object Detection Based on Deep Pruning for Remote Sensing Image. 2018 Cham. Springer International Publishing, 137-147.

WANG, Y., FANG, Z. & HONG, H. 2019. Comparison of convolutional neural networks for landslide susceptibility mapping in Yanshan County, China. *Science of The Total Environment,* 666**,** 975-993.

WEI, H. & BARTELS, M. 2012. 3D Digital Elevation Model Generation. *In:* PEARS, N., LIU, Y. & BUNTING, P. (eds.) *3D Imaging, Analysis and Applications.* London: Springer London.

WGMS. 2021. *Global Galcier State* [Online]. World Glacier Monitoring Service. Available: https://wgms.ch/global-glacier-state/ [Accessed 13.03 2021].

WHALLEY, W. B. & AZIZI, F. 2003. Rock glaciers and protalus landforms: Analogous forms and ice sources on Earth and Mars. *Journal of Geophysical Research - Planets,* 108**,** 8032-n/a.

WHALLEY, W. B. & MARTIN, H. E. 1992. Rock glaciers : II models and mechanisms. *Progress in physical geography,* 16**,** 127-186.

WHITE, P. G. 1979. Rock Glacier Morphometry, San Juan Mountains, Colorado. *GSA Bulletin,* 90**,** 924-952.

WIEDERKEHR, M. & MÖRI, A. 2013. Swissalti3D : a new tool for geological mapping. *Swiss Bulletin für angewandte Geologie,* 18**,** 61.

YANI, M., IRAWAN, S. & S.T, M. T. 2019. Application of Transfer Learning Using Convolutional Neural Network Method for Early Detection of Terry's Nail. *Journal of Physics: Conference Series,* 1201**,** 012052.

ZEZE, R. & LIU, G. 2018. Rock glaciers in Daxue Shan, south-eastern Tibetan Plateau: an inventory, their distribution, and their environmental controls. *The Cryosphere,* 12**,** 2327-2340.

ZHANG, E., LIU, L. & HUANG, L. 2019. Automatically delineating the calving front of Jakobshavn Isbræ from multitemporal TerraSAR-X images: a deep learning approach. *The Cryosphere,* 13**,** 1729-1741.

11.Appendices

11.3. Scatter plots showing aspect and mapping accuracy

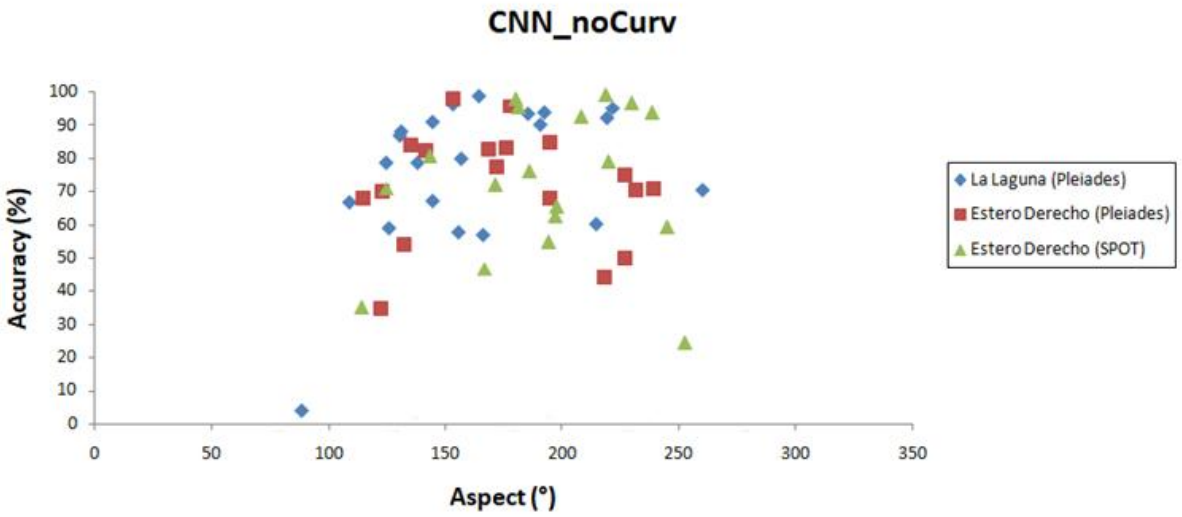

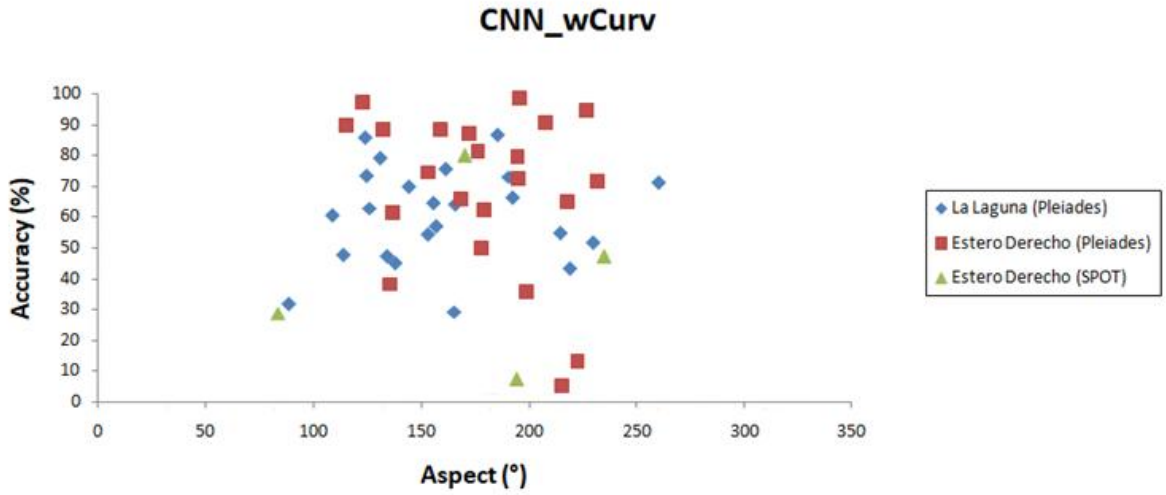

11.4. Scatter plots showing compactness and mapping accuracy